

AUTOMATED PLATFORMS AND SOFTWARE-DEFINED
INSTRUMENTATION FOR RADAR SOUNDING OF ICE

A DISSERTATION
SUBMITTED TO THE DEPARTMENT OF ELECTRICAL ENGINEERING
AND THE COMMITTEE ON GRADUATE STUDIES
OF STANFORD UNIVERSITY
IN PARTIAL FULFILLMENT OF THE REQUIREMENTS
FOR THE DEGREE OF
DOCTOR OF PHILOSOPHY

Thomas Olmsted Teisberg
June 2025

© 2025 by Thomas Olmsted Teisberg. All Rights Reserved.
Re-distributed by Stanford University under license with the author.



This work is licensed under a Creative Commons Attribution-
Noncommercial 3.0 United States License.
<http://creativecommons.org/licenses/by-nc/3.0/us/>

This dissertation is online at: <https://purl.stanford.edu/hx433gb9980>

I certify that I have read this dissertation and that, in my opinion, it is fully adequate in scope and quality as a dissertation for the degree of Doctor of Philosophy.

Dustin Schroeder, Primary Adviser

I certify that I have read this dissertation and that, in my opinion, it is fully adequate in scope and quality as a dissertation for the degree of Doctor of Philosophy.

Ching-Yao Lai

I certify that I have read this dissertation and that, in my opinion, it is fully adequate in scope and quality as a dissertation for the degree of Doctor of Philosophy.

Howard Zebker

Approved for the Stanford University Committee on Graduate Studies.

Stacey F. Bent, Vice Provost for Graduate Education

This signature page was generated electronically upon submission of this dissertation in electronic format.

Abstract

Ice-penetrating radar (IPR) refers to a class of radar instruments used to image into and through ice, especially glacial ice found in Earth's glaciers, ice caps, and ice sheets. Since the 1960s, IPR has been used from airborne platforms to image englacial layers and the bedrock hidden beneath the surface of the Antarctic Ice Sheet (AIS) and the Greenland Ice Sheet (GIS). Although other methods are also used to image beneath ice, IPR is the only remote sensing approach capable of giving direct measurements of ice thickness. As a result, IPR data plays a crucial role in our understanding of the dynamics of ice sheets and glaciers and in models of the future evolution, and sea level rise contributions, of these ice masses.

Due to the complexity of the dynamics of Earth's ice sheets and the long timescales of their response to interactions with the ocean, atmosphere, and solid earth, much remains unknown about the dynamics of the AIS and GIS, especially in light of recent warming of the atmosphere. Understanding and predicting the future behavior of the AIS and GIS will require both expanding collection of sub-surface data and developing new ways to process and interpret it.

The first two chapters focus on the development of a miniaturized, low-cost IPR system integrated with a small, fixed-wing uncrewed aerial vehicle (UAV). Chapter 2 covers the development of core radar system, the Open Radar Code Architecture (ORCA), which was a collaborative effort with my fellow PhD student Anna Broome that we spun out as an open-source framework for building scientifically-driven customized ice-penetrating radar systems. The core of the approach is to use software-defined radios (SDRs) to be able to reduce development time by shifting much of the complexity of the instrument design from hardware into software. This approach allows us to rapidly develop different instruments with varying capabilities by utilizing a range of inter-compatible SDRs and/or simply changing the software configuration. The bulk of this work is focused on validation of the core software to ensure its suitability for building scientific instruments.

Chapter 3 introduces one of the radar instruments that inspired the development of ORCA. Peregrine is a 2-meter wingspan UAV carrying a miniaturized IPR instrument. Peregrine is in part a field instrument and in part a testing ground for future UAV-borne IPR designs. Aside from miniaturizing the core radar instrument to under 400 grams, the primary challenge with incorporating an IPR into a small UAV is the design of antennas that are compatible with the aircraft. Because IPR

instruments operate at low frequencies, the antennas generally need to be fairly large. While this is not a major problem for crewed aircraft, it becomes particularly challenging on very small aircraft, such as UAVs. Peregrine used a set of miniaturized IPR antennas designed specifically to integrate under the wings with minimal impact to the aircraft design. Peregrine has been tested in real-world polar field conditions in Iceland, Svalbard, and Greenland. Results from those field campaigns are presented.

Peregrine is also a testing ground for larger UAV-borne IPR systems. Ground testing has been completed on a variant of the Peregrine IPR instrument designed for a 4-meter wingspan UAV, utilizing lessons learned from the smaller-scale development effort. Chapter 4 discusses potential improvements to the Peregrine system as well as system design choices for adapting the Peregrine radar to larger UAS. This chapter provides selected quantitative performance targets that should be achievable by UAV-borne systems of various sizes and guideposts towards achieving them.

Chapter 5 diverges slightly and discusses an emerging application of UAV-borne IPR surveying: interferometric processing of repeat-pass radar data to obtain estimates of englacial velocity. The availability of surface velocity measurements at high spatial and temporal scales has been transformative to our understanding of ice sheet dynamics. Unfortunately, measurements of sub-surface velocities have so far been limited to techniques requiring extensive on-the-ground fieldwork. With the improved capabilities to perform precise repeat measurements, UAV-borne IPR systems may offer a remote sensing option to measure the deformation of internal layers within the ice. This chapter contains an analysis of how these measurements of internal deformation may be used to reconstruct the three-dimensional velocity structure of the ice with minimal assumptions on the physical properties of the ice.

Finally, chapter 6 summarizes the contributions of this work and lists possible next steps in the development of the ideas presented in each of the preceding chapters.

Acknowledgments

I have been incredibly lucky to be surrounded by amazing, patient, and brilliant mentors, family, and friends, without any of whom I would never have made it to this point. As any Ph.D. student will tell you, the most important school-related decision you ever make is picking a Ph.D. advisor. I choose very well (or perhaps just got very lucky) in having Dusty Schroeder as my advisor. Dusty, thank you for always believing in me, for patiently guiding me through the many twists and turns of deciding what I actually wanted to work on, and for supporting me as a whole human, all the way through to serving cocktails at my wedding. Your wholehearted embrace of each and every one of your students as a scholar and as a person has been the best part of my academic journey.

I have been lucky to have many faculty mentors beyond my formal advisor. I would, of course, like to thank my committee, Howard Zebker, Ching-Yao Lai, and Zerina Kapetanovic, both for being a part of my committee and for answering numerous questions and providing advice over the years. I have also had the privilege of working with Mathieu Morlighem and Jamin Greenbaum, both of whom have provided invaluable advice to me and been role models in the field.

My committee chair, Mykel Kochenderfer, deserves a special thank you. I first met Mykel as an undergraduate with an idea that no one else would say yes to. Over the years, Mykel was one of a few professors who transformed my view of what getting a Ph.D. in engineering was about. When I finally decided to try working in a lab for a summer, Amin Arbabian taught me what engineering research really was. Without his patient mentorship, I would never have applied to a Ph.D. programs. Sorry for dropping out that first time – at least I made it back the next year. John Pauly and Dwight Nishimura also deserve a thank you for sparking my interest in signal processing and fielding my numerous questions about grad school.

One of the unexpected opportunities of grad school was getting to do fieldwork across the Arctic to test my systems. The complex logistics of shipping equipment around the world, getting permits, accessing field sites, and staying both warm and safe was possible only with the support of far too many amazing people to name all of them here. Among them, however, I'd particularly like to thank Stephan Mantler, Tor-Arne Johansen, Sam Dorsi, Ian Geraghty, and Tina Dobleman, without each of whom one or more of our field trips would not have been possible. The Geophysics Department staff have also been amazing, adopting me in and making me feel like Geophysics was truly my

home. They have also put up with an unreasonable number of requests to do weird things, like buying Pelican cases at auction from failed startups or shipping 1000 lbs of equipment across the country overnight, to name just a couple. Thank you Liliane Pereira, Ros McCambridge, Jeremy Samos, and Clark Campagna.

My advisor and other mentors made my Ph.D. possible, but it was my incredible labmates who made it fun. Sean, Mickey, Riley, Nicole, Winnie, Anna, Eliza, Danny, Natalie, Annie, Oliver, Jordan, Sunme, and (honorarily) Paul, you have all been amazing labmates, and I'm lucky to count you all as my friends. I've learned so much from each of you and enjoyed every adventure together. I couldn't have asked for a better person to do five field seasons with than Anna, who stays relentlessly calm and sane no matter what is happening. For the record, I did beat Anna in Banagrams exactly once, but we will not discuss how many hundreds of attempts that took. Going anywhere with Eliza is guaranteed to be both very fun and an extremely good workout. I hope you will one day fulfill your dream of windsurfing across Antarctica. Danny, I admire your endless positivity, though I'm still confused by your love of dry oatmeal and freeze-dried foods. To all of the undergrads I've worked with over the last few years, thank you for your time and I hope you had as much fun as I did.

My friends outside of school have also been amazing sources of support and sanity. I'm especially thankful for my undergrad crew, Andrew, Jean-Luc, Justin, and Ashwin, who have been my companions for so many adventures.

Finally, I am immensely grateful to my family: my mom and dad, who always offered their full support for whatever I was doing, with no pressure or conditions, my brother, who is always there for me at any time of day, and, of course, my wife, Mai, who always knows how to make me smile no matter what is happening. I could never have done any of this without all of you. Mai, thank you for putting up with every twist and turn of this process and still signing up for a lifetime more of it at the end.

The work in this dissertation was only possible with financial support from many groups. In order of the awards, my work has been supported by the Heising-Simons Foundation, the Stanford Institute for Human-Centered Artificial Intelligence, the National Aeronautics and Space Administration (NASA), Stanford Data Science, the TomKat Center for Sustainable Energy, and the National Science Foundation (NSF). To the program managers, administrators, and field logistics teams at NASA, NSF, and Polar Field Services (PFS), thank you for supporting this work.

This work was supported in part by the National Science Foundation under Grant 284791. It was also supported by the National Aeronautics and Space Administration (NASA) under Grant 80NSSC22K0782 and NASA Future Investigators in NASA Earth and Space Science and Technology (FINESST) Grant 80NSSC23K0271.

Contents

Abstract	iv
Acknowledgments	vi
1 Introduction	1
1.1 Scientific Motivations	1
1.2 Ice-Penetrating Radar	2
1.3 Platforms for Ice-Penetrating Radar	4
1.4 Dissertation Outline	6
2 Open Radar Code Architecture	8
2.1 Abstract	8
2.2 Introduction	9
2.3 Prototypical Radar System	11
2.4 Radar Code Architecture	12
2.4.1 Error Handling	13
2.4.2 Data Storage, Metadata, and Configuration	13
2.5 Signal Coherence Characterization and Analysis	15
2.6 Noise Source Characterization and Analysis	17
2.6.1 Local Oscillator (LO) Leakage	18
2.6.2 Switching Noise	19
2.6.3 Radio-frequency Interference	21
2.6.4 Thermal Noise	21
2.6.5 Phase Dithering to Overcome Coherent Noise	22
2.7 SDR Calibration	23
2.8 Processing Code	24
2.9 SDR & Host Hardware Options	25
2.9.1 Performance Benchmarking	26
2.10 Conclusion	28

3 Peregrine UAV-borne Ice-Penetrating Radar	30
3.1 Abstract	30
3.2 Introduction	30
3.3 System architecture	31
3.3.1 Aircraft	32
3.3.2 Antennas	33
3.3.3 Radar sounder	35
3.4 Experimental results	36
3.4.1 Case study: Slakbreen Glacier, Svalbard	36
3.4.2 Analysis of SNR	37
3.5 Estimating radar performance	39
3.6 Future work	40
3.7 Discussion	41
3.8 Conclusion	42
4 Future developments in UAV-borne IPR	44
4.1 A perspective on the pathways for UAV-borne IPR	44
4.2 Performance targets for UAV-borne RES	45
4.3 System improvements for Peregrine	48
4.4 Radar development roadmap for larger UAVs	50
4.4.1 RF front-end	50
4.4.2 Expected performance improvements	53
5 Measurement of Englacial Velocity Fields with InRES	54
5.1 Abstract	54
5.2 Introduction	55
5.2.1 Englacial layering in radio echo sounding	56
5.2.2 Prior work in radio echo sounder layer interferometry	56
5.3 Interferometric measurement of englacial layer deformation	57
5.3.1 Notation	57
5.3.2 Estimating the three-dimensional englacial velocity field	59
5.3.3 Boundary conditions	61
5.4 Zero layer slope approximation	61
5.4.1 Interpolation between zero layer slope areas	62
5.5 Radar measurement model	63
5.5.1 Measurement error sources	64
5.5.2 Off-nadir reflections from non-zero layer slopes	64
5.5.3 Radar instrument offset between measurements	65

5.5.4	Difficulty of absolutely referencing layer motion	66
5.5.5	Phase wrapping and layer alignment	67
5.6	Applications and Examples	67
5.6.1	Rheology estimation	68
5.6.2	Spatially variable rheology	69
5.6.3	Observing basal sliding	70
5.6.4	Identifying englacial velocity in transition	71
5.6.5	Measurement noise and cross-track error simulations	72
5.7	Discussion	73
5.8	Conclusions	76
5.9	Stability of horizontal velocity ODE	76
5.10	SIA model to evaluate zero layer slope approximation	78
6	Conclusions	81
6.1	Summary of Research	81
6.2	Future Directions	81
6.2.1	Software-defined radar	82
6.2.2	UAV-borne ice-penetrating radar	82
6.2.3	Interferometric estimation of englacial velocity	82
References		84

List of Tables

2.1	Noise sources impacting ice-penetrating radars and mitigations	18
2.2	Ettus SDR options	25
3.1	Peregrine System Mass Budget	36

List of Figures

1.1	IPCC estimates of uncertainty in sea level rise	2
1.2	Density of IPR survey data over the AIS	3
1.3	Repeat IPR surveys over the AIS	5
1.4	Key considerations for IPR performance across possible platforms	6
2.1	Loopback testing setup diagram	9
2.2	ORCA code flowchart	14
2.3	Chirp coherence test results	16
2.4	Phase variance measurements	17
2.5	Spectrograms of chirps showing noise sources	19
2.6	Switching power supply noise	20
2.7	Noise floor versus coherent summations	22
2.8	Input power calibration	24
2.9	Error rate versus pulse repetition frequency for different host computer interfaces	27
3.1	Photo of Peregrine	32
3.2	Peregrine antenna design	34
3.3	Radar payload diagram	35
3.4	Slakbreen example radargram	37
3.5	Altitude versus surface SNR	38
3.6	Transmit parameters versus surface SNR	38
3.7	SNR versus coherent summation	40
3.8	Existing IPR survey density over the Antarctic Ice Sheet	41
4.1	Geometric spreading correction magnitudes for required surface SNR calculations	46
4.2	Cumulative distribution functions of required surface SNR	47
4.3	Map of UAV range rings around existing Antarctic research stations	48
4.4	Updated RF front-end block diagram	51
4.5	Cumulative distribution function of required surface SNR	52

5.1	Cartoon of horizontal advection of sloped layers	58
5.2	Zero layer slope approximation errors	62
5.3	Diagram of geometric error sources	65
5.4	Solution results from a synthetic flowline model with identical surface expression . .	68
5.5	Example of estimating spatially-variable ice rheology	70
5.6	Frozen-to-sliding transition example	71
5.7	Estimating basal velocity from layer velocity	72
5.8	Identifying recent changes in flow history	73
5.9	Effects of phase noise on velocity reconstruction	74
5.10	Greenland surface velocity divergence	77
5.11	Maximum layer slope for the zero slope approximation under a bounded error	79

Chapter 1

Introduction

1.1 Scientific Motivations

The Greenland Ice Sheet (GIS) and Antarctic Ice Sheet (AIS) represent massive repositories of frozen freshwater, changing under a combination of their own internal dynamics and interactions with the atmosphere, oceans, and solid earth. The GIS holds an estimated 7.4 meters of equivalent global mean sea level rise [94], while the AIS contains an estimated 57.9 meters [97]. Since first becoming glaciated tens of millions of years ago, the AIS has grown and shrunk periodically [112, 9]. The GIS is the relatively younger ice sheet, likely having seen complete deglaciation sometime during the Pleistocene [123]. While this history makes it clear that dramatically different configurations of the AIS and GIS are possible, the timescales of historical changes are extremely long in comparison to the modern observational record, and deep uncertainties remain about how either ice sheet may respond to atmospheric or ocean changes on human-relevant timescales.

This uncertainty, especially in the future of the AIS, is represented by a wide interval of plausible future sea level rise under future climate scenarios as reported by the Intergovernmental Panel on Climate Change (IPCC). IPCC “likely” range consensus estimates of future global mean sea level rise by 2100 vary from less than 0.3 meters to more than 1 meter, as shown in Fig. 1.1. Under each “Shared Socioeconomic Pathway” (SSP), the overall “likely” range covers a span of 0.25 to 0.35 m, with the majority of each range accounted for by uncertainty in contributions from the AIS. This deep uncertainty arises because we do not fully understand the dynamics of the AIS, especially how it interacts at its boundaries: with the atmosphere, the ocean, and the Earth beneath it [105]. Because the IPCC estimates are based on current ice sheet models that do not account for all hypothesized mechanisms of retreat, some argue that the IPCC numbers may underestimate the true uncertainty, especially on the warmer end of climate scenarios [133]. With the GIS already accounting for the highest rate of change in sea level [65] and the AIS representing by far the largest uncertainty by 2100 [43], the importance of understanding the dynamics of Earth’s ice sheets is clear.

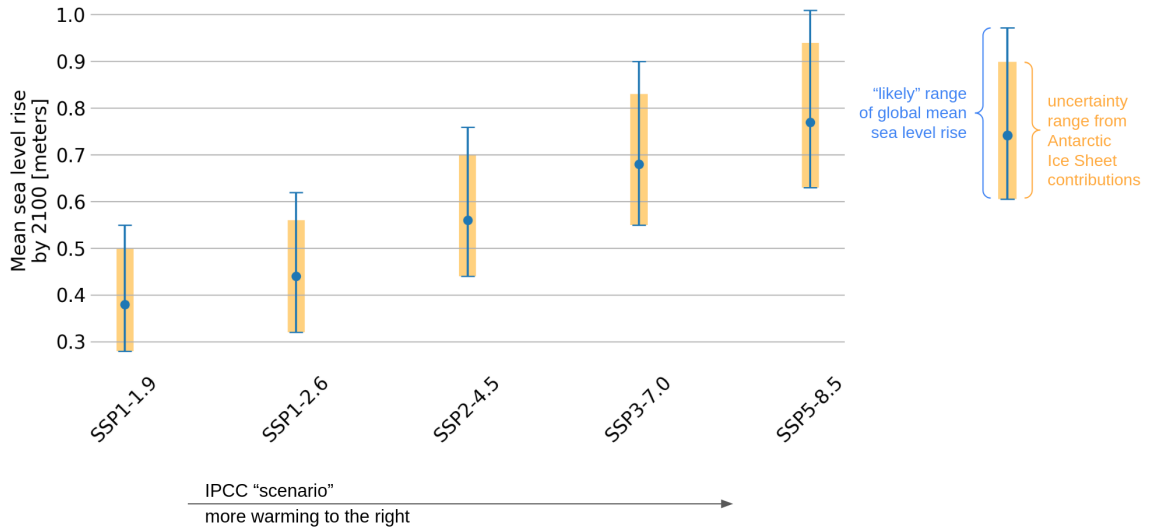


Figure 1.1: Mean global sea level rise estimate (blue dots) and "likely" range (between blue ticks) for the five IPCC scenarios, roughly corresponding to higher rates of warming to the right. The yellow bars represent the uncertainty range of just the Antarctic Ice Sheet's modeled contributions to sea level rise. Uncertainty in changes in the AIS is a major contributor to overall uncertainty in future sea level rise. Data from IPCC AR6 Table 9.9 [43].

1.2 Ice-Penetrating Radar

The relative transparency of ice to radio waves was first reported in the late 1920s [136], but little attention was paid to it until pilots began to notice erroneous readings from radar altimeters when flying over the ice sheets [144]. These anomalous readings spurred new interest in understanding the electromagnetic properties of ice. Supporting by national interests in Antarctic science, the first large-scale airborne ice-penetrating radar (IPR) surveys were carried out over the AIS in the late 1960s and 1970s [100], shortly followed by similar surveys of the GIS [53].

IPR relies on the same principles as other radar systems, however it is distinguished by using low enough frequencies to penetrate deep into snow and ice (generally under 1 GHz) and being generally nadir-looking. IPR instruments record reflections off of englacial and subglacial interfaces. Early surveying efforts were primarily aimed at mapping the bedrock beneath the AIS and GIS, however it quickly became apparent IPR instruments were also detecting englacial interfaces, known as "layers," that were also of scientific interest [54]. Englacial interfaces may occur for a variety of reasons, but, over polar ice sheets, they are generally assumed to represent past buried surfaces with slightly different dielectric properties [134]. The attenuation observed within the ice provides constraints on englacial temperature [127, 33]. Although IPR typically does not penetrate past the basal interface, IPR data can also be used to estimate the properties of the basal interface, including

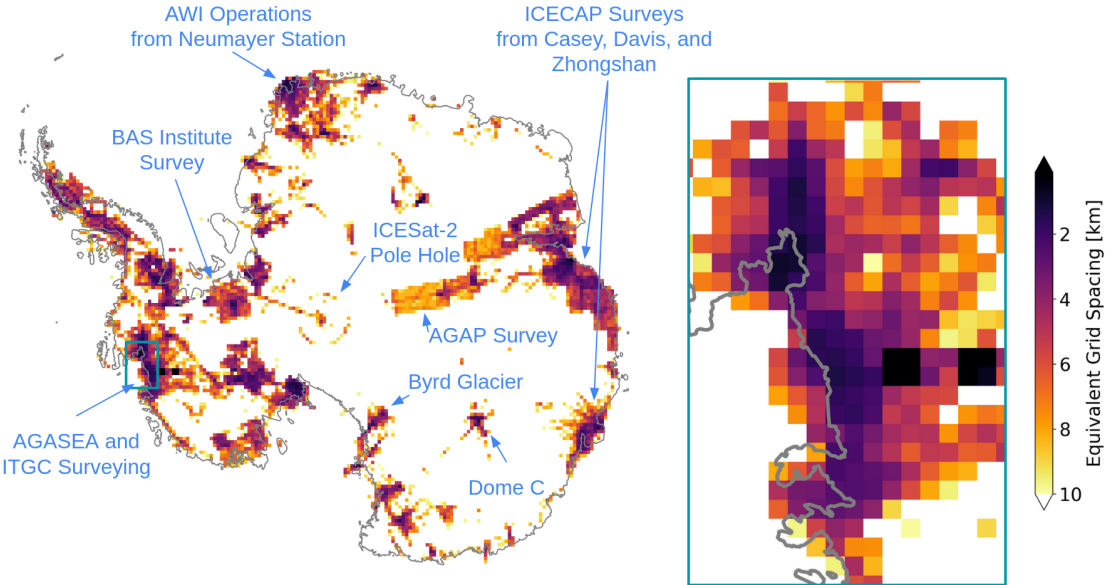


Figure 1.2: Equivalent gridded survey density of all IPR data collected, as represented in the BedMap 3 data release, over the AIS (left) and in the Amundsen Sea Embayment (zoom box on the right). Selected notable survey locations are shown in blue. All line-km of IPR survey data in each 30 km x 30 km grid cell are summed and converted to an equivalent grid spacing if all of that data had been a single gridded survey of the cell. Note that, while BedMap 3 represents the best available collection of IPR survey lines, some data may still be missing. Inclusion in BedMap 3 does not mean that the actual survey data is publicly available. IPR survey location data from Frémand et al. [44].

identifying subglacial water [124]. More recently, radar polarimetry has been used to estimate ice fabric properties [70] and radar interferometry to constrain englacial velocity [73] (more about this in Chapter 5).

Although IPR data was among the first types of data to be collected at large scale across the AIS and GIS, the volume of data available to date is now small in comparison to many satellite-derived measurements. Although IPR instruments are carried on satellites around other planets, significant obstacles exist to developing an orbital IPR instrument for Earth’s ice sheets [128, 29, see also Section 1.3]. As a result, large-scale IPR data collection remains the domain of sub-orbital airborne platforms. Since the 1960s, IPR data collection has largely been viewed as a mapping project seeking to fill in the gaps of the unknown subglacial topography. These data collection efforts have certainly led to significant advances in our knowledge of subglacial topography and our ability to model our ice sheets [115, 44, 97]. The vast scale of the ice sheets, especially the AIS, however, makes it easy to hide how little we know. Recent work estimated that radar survey horizontal resolution in the vicinity of Thwaites Glacier should be 2 km or better to achieve the ± 2 cm uncertainty in sea level rise over 200 years goal in the 2017 Decadal Survey [24]. Incorporating all reported IPR flight lines

released as part of the BedMap 3 effort [44], Fig. 1.2 shows the equivalent survey spacing if every line-km of data collected in each 30 km by 30 km grid cell had been flown as part of a coordinated gridded survey. On the right side of the figure is a zoom-in on the Amundsen Sea Embayment, where Thwaites is located. In parts of this area, the overall survey density is reaching, or even exceeding, that 2 km target. Across most of the AIS, though, equivalent survey densities are far lower, generally worse than 10 km. Although not all locations will require the same survey density and Thwaites likely requires a higher survey density than most areas, this view is a helpful reminder that even the bed mapping project is nowhere near complete.

As we seek the understand the dynamics of the ice sheets, new applications of IPR are moving beyond one-time measurements. Of particular interest is IPR interferometry, a technique in which the phase differences between two spatially coincident measurements are analyzed to estimate the motion occurring between the two measurements. This technique promises to provide the first remote sensing method of estimating the subsurface velocity structure of ice sheets. (For details on this method, see Chapter 5). This technique requires multiple measurements of the same location, spaced appropriately in time (relative to the rate of internal motion of the englacial layers). Few repeat IPR measurements exist over Antarctica. Even by the generous standard of counting any measurements passing through the same 1 square km grid cell from distinct surveys, the metric shown in Fig. 1.3, repeat IPR measurements are sparse even in the most heavily surveyed areas. This is largely by design. For decades, the focus has been on filling in new pieces of the map, so re-surveying the same areas was something to be avoided. As new processing techniques unlock new science opportunities, however, the way we think about planning IPR surveys will need to adapt.

1.3 Platforms for Ice-Penetrating Radar

At roughly 150% the size of the continental United States and featuring far fewer airports, the AIS is a challenging environment for airborne surveying. Compounding the pure remoteness are cold temperatures, adverse weather, and long periods of polar night. The combination of these factors limits scientific aircraft operations to a few months of Austral summer. Despite these limitations, the international science community has averaged roughly 85,000 line-km of airborne IPR survey data per year from 2000 to 2019 and 58,000 line-km per year in Greenland from 2009 through 2019. (The AIS estimate is based on data from Frémand et al. [44] and the GIS estimate, including only US-based Operation IceBridge flights, is based on Morlighem et al. [94].) Despite these heroic efforts, the demand for new data remains high [115]. There is growing interest in alternative platforms to crewed aircraft to satisfy these data needs. Proposed alternatives include conventional UAVs [7, 141, 121], stratospheric solar-powered UAVs [35], and Earth-orbiting satellites [58, 17, 19, 50, 59, 61]. Despite the obvious enthusiasm for orbital platforms, there are unique challenges for orbital IPR instruments [128, 29], though these may be overcome with clever engineering and technological

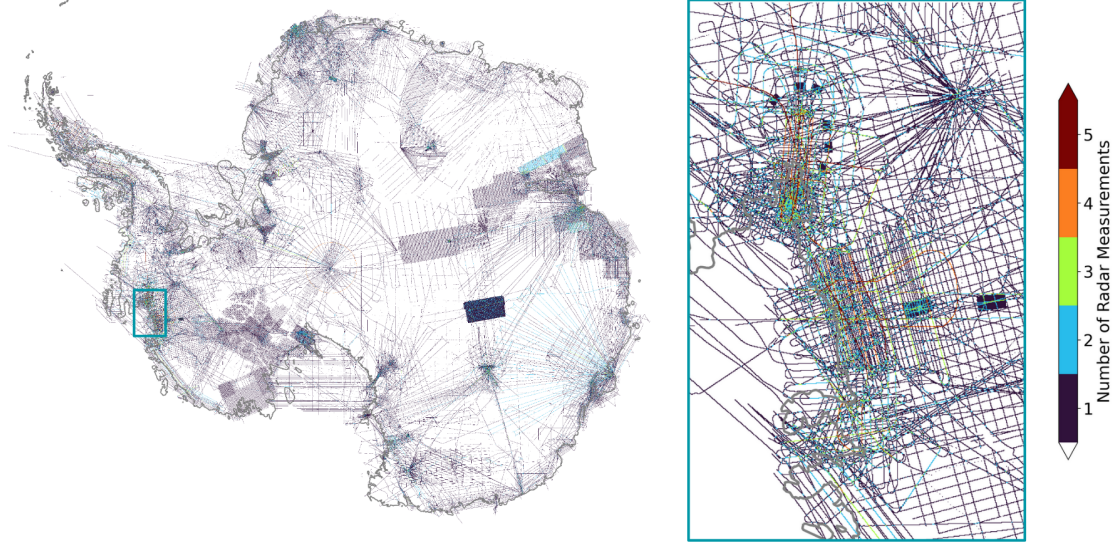


Figure 1.3: Number of repeated IPR measurements over the AIS (left) and in the Amundsen Sea Embayment (zoom box on the right). The number of measurements is determined by summing the number of surveys that included a measurement crossing any part of each 1 km x 1 km grid cell. Measurements do not need to be exactly overlapping or from the same radar system to count as repeats. IPR survey location data from Frémand et al. [44].

advances.

When considering new IPR instruments and platforms, there are three especially important metrics to consider: signal-to-noise ratio, signal-to-clutter ratio, and range resolution. Each of these concepts is illustrated in Fig. 1.4 and briefly described in the context of platform selection below:

- **Signal to noise ratio (SNR)** is the most familiar and the most commonly analyzed. In the IPR context, it refers to the ratio of the power reflected from the desired imaging interface to the ratio of background noise. Typically, this is either thermal noise or a cosmic noise source, depending on the antenna's properties and the receiver design [7]. Noise power is generally constant with altitude, but signal power decreases as a result of geometric spreading. To recover suitable SNRs, high-altitude platforms generally need more transmit power, longer dwell times, or a higher effective antenna (array) gain (real or synthetic).
- **Signal to clutter ratio (SCR)** is the ratio of the power from desired reflecting interfaces to the power from undesired but still real reflecting interfaces that may obscure the desired target(s). In the context of IPR, clutter comes primarily from near-surface off-nadir reflections [29]. As platform altitudes increase, the antenna's beam pattern makes it sensitive to a wider area of potential off-nadir reflections and surface reflections at the same range delay as deeper

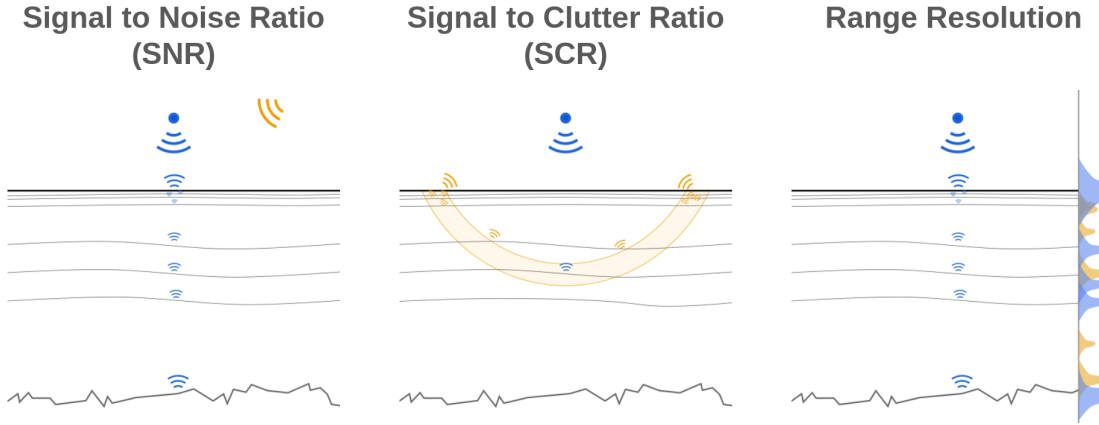


Figure 1.4: This figure illustrates three key performance metrics to consider when evaluating the combination of an IPR instrument and a potential platform. From left to right: Signal to noise ratio (SNR) is the ratio of the power returned from a desired reflection (the signal) to the dominating background noise source, which is typically thermal or cosmic noise. Signal to clutter ratio (SCR) is the ratio of power returned from a desired reflection to power returned by reflections off of real interfaces that are not the designed target. In IPR, this typically means off-nadir reflections, especially cross-track off-nadir reflections that may be difficult to discriminate from reflections at nadir. Range resolution refers to the ability of a radar system to distinguish two reflections closely spaced in range. This is important both for distinguishing targets at nadir from each other and for separating off-nadir reflections from the desired signal.

englacial and basal interfaces appear at higher incidence angles. This is a major additional challenge for high-altitude systems.

- **Range resolution** refers to the ability of a radar system to differentiate between two targets spaced closely together in the range dimension. It is primarily a function of the radar waveform bandwidth and any window function or other modulation features applied to the waveform. In the context of IPR systems, range resolution is important both for distinguishing different englacial layers and for effectively separating off-nadir clutter from desired reflections. Although range resolution does not change with altitude, the presence of more clutter may make range resolution more important. And frequency allocation rules may make bandwidth less available on orbital platforms.

1.4 Dissertation Outline

Chapters 2 and 3 collectively represent the IPR development work. My co-author and fellow PhD student Anna Broome and I were each working on an IPR instrument early in our PhD process. We realized that the foundations we were building could be shared and started working together

to build a common core for our radar systems. This eventually became ORCA, the Open Radar Code Architecture, an open-source effort to build easily customizable IPR systems tuned to specific scientific objectives. Chapter 2 describes that effort and lays the foundation of using software-defined radios (SDRs) as the backbone of IPR instruments. This chapter focuses on understanding the performance of the SDRs and how that performance relates to the IPR link budget, especially in the context of long acquisition times.

Chapter 3 represents the main project that I built on top of the scaffolding of the ORCA project. Peregrine is a small, fixed-wing uncrewed aerial vehicle (UAV) that carries a miniaturized IPR. It builds upon the ORCA project, using an extremely lightweight SDR to provide an IPR instrument at under 400 grams (1 kg with cabling and antennas). The antennas are designed specifically to integrate with the aircraft and are fabricated such that they can be conformally attached to the underside of the wings.

The objective of building UAV-borne IPR systems is to increase access and bring down the costs of collecting new IPR data. Traditionally, IPR data has been viewed primarily as a map-making tool, with the goal of new surveys being to "fill in the gaps." While there are still gaps to fill, there is also a growing body of work on identifying changes through repeat IPR measurements. These time series measurements force us to think about IPR data collection as an ongoing monitoring effort, not just a race to fill in the last gaps.

Chapter 4 provides one possible roadmap for future UAV-borne IPR work. It provides some quantitative targets for what may be achievable with UAV-borne systems and some specific suggestions where there remains room for improvement in Peregrine and in ORCA-derived radar systems for future larger UAS.

Chapter 5 explores using repeat-pass IPR measurements to reconstruct englacial velocity. Most ice sheet models are heavily reliant on high spatial and temporal resolution measurements of surface velocity, but subsurface velocity measurements are only extremely sparsely available, generally requiring intensive fieldwork. The ability to collect sub-surface velocity measurements with IPR would be transformative for ice sheet models. At the same time, it would add to the need to collect IPR data in the same places on a routine basis, something best enabled by automated platforms capable of precisely repeating survey lines over and over again. This importance of automated IPR platforms to collecting interferometric IPR data is the connection between this chapter and the others.

Chapter 6 summarizes the main contributions of this dissertation and briefly reviews potential next steps in each of the areas covered above.

Chapter 2

Open Radar Code Architecture (ORCA): A Platform for Software-defined Coherent Chirped Radar Systems

This chapter was published as:

Thomas O. Teisberg, Anna L. Broome, and Dustin M. Schroeder. “Open Radar Code Architecture (ORCA): A Platform for Software-Defined Coherent Chirped Radar Systems”. In: *IEEE Transactions on Geoscience and Remote Sensing* 62 (2024), pp. 1–11. ISSN: 0196-2892, 1558-0644. DOI: 10.1109/TGRS.2024.3446368. URL: <https://ieeexplore.ieee.org/document/10639440/>

Thomas Teisberg and Anna Broome are equal contribution co-first authors.

Copyright Thomas O. Teisberg, Anna L. Broome, and Dustin M. Schroeder, 2024. Licensed under Creative Commons BY-NC-ND 4.0.

2.1 Abstract

Ice-penetrating radar systems are critical instruments for observing the subsurface conditions on Earth’s ice sheets. Traditionally, ice-penetrating radars have not been widely accessible to the glaciological community (as in the case of resource-intensive airborne systems) and/or have been limited in their ability to be reconfigured and optimized for studying different glaciological targets

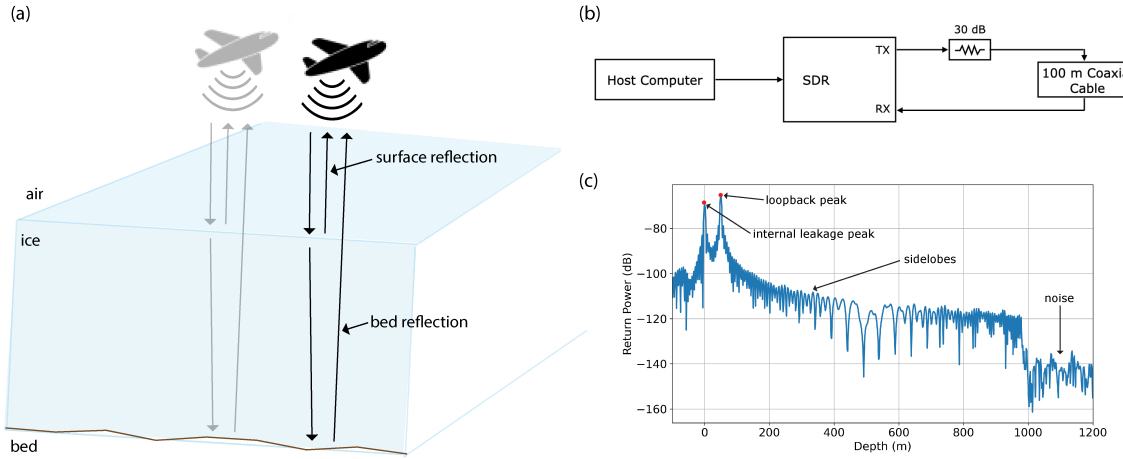


Figure 2.1: (a) Cartoon of a typical ice-penetrating radar survey geometry. An electromagnetic signal is transmitted from the radar, which is depicted here on an airborne platform. These signals reflect off dielectric contrasts, such as the air-ice interface and the ice-bed interface. (b) Setup for a “loopback” test in which the SDR transmit port is directly connected to the receive port through an attenuator and coaxial cable that introduces a fixed time delay, which is dependent on the cable length. (c) Example of data produced by such a loopback test (after pulse compression), showing both the direct coupling internal to the SDR and the signal transmitted through the coaxial cable (red dots). Data collected on an Ettus B205mini SDR.

(as in the case of hardware-defined radar systems). To alleviate the challenges associated with this situation, we have developed the Open Radar Code Architecture (ORCA), which is an open-source radar software codebase that allows commercially available software-defined radios (SDRs) to be used as coherent ice-penetrating radars. Here, we describe the architecture of our code, characterize coherence on SDR-based radars, and demonstrate techniques we use to improve SNR and overall performance. We also highlight the variety of SDR options available to potential users and discuss tradeoffs between different system configurations.

2.2 Introduction

The cryosphere is one of the most sensitive components of the Earth system to a changing climate [42]. In particular, Earth’s polar ice sheets represent the largest contribution to uncertainty in mean sea level rise by 2100 according to the Intergovernmental Panel on Climate Change (IPCC) models [42]. Reducing uncertainty in predictions of future global sea level change requires a better understanding of the physical processes and conditions underlying ice-sheet motion, as well as improved models that better capture the relevant physics and processes. Ice-penetrating radars, also known as radio echo sounders, are a widely-employed class of instrument whose measurements are used to

estimate numerous glaciological conditions relevant to ice sheet models [76, 130]. These glaciological conditions include ice thickness, basal material, basal roughness, englacial and basal thermal state, englacial water, englacial layering, crystal orientation fabric, and other properties. Information about these conditions may be directly derived from ice-penetrating radar observations or they may be determined using inversion-based estimation techniques [126].

Traditionally, ice-penetrating radars used in glaciology have been limited to a few airborne systems (e.g. [119, 106, 155, 62]), semi-custom ground-based systems (e.g. [12, 98, 91, 93]), adaptations of commercial ground-penetrating radars (e.g [18, 25]) and other one-off systems developed by individual research groups (e.g. [151, 26]). All of these systems have distinct benefits and drawbacks, as well as their own unique resource constraints. A drawback shared amongst many existing systems is that they are rigid in their system design. In other words, once the radar system has been designed, tested, and built, it is very difficult to modify its configuration, which may be necessary to study different glaciological targets. Furthermore, the existing systems that are capable of surveying moderate to extensive spatial areas are so resource intensive that their field campaigns often require significant national or multinational support (e.g. [84]). This makes targeted data collection with these systems an unrealistic option for many research groups.

Software-defined radios (SDRs) are radio communications systems that implement core functionality, such as filtering, mixing, amplification, modulation, and demodulation, primarily in the digital domain, as opposed to using dedicated analog electronic circuits. Moving this core functionality from the analog to the digital domain increases the flexibility of the system, typically widening its operating frequency range, at the expense of fine-tuned performance. Utilizing SDRs as radar transceivers increases flexibility in the implementation of radar systems, particularly in terms of waveform design, choice of center frequencies and bandwidths, rapid reconfigurability, and system architecture choices.

Recently SDRs have been used as the backbone for several cryosphere-focused remote sensing systems. In [114], an Ettus E312 SDR was mounted on a hexacopter uncrewed autonomous system (UAS) to map snow depths. A bistatic ice-penetrating radar with wireless synchronization was developed in [10] using an Ettus E312 for its receiver, and successfully observed basal reflections from 1000 m thick ice. A passive radar sounder, using the sun as a signal source, has also observed basal reflections from 1000 m thick ice and is likewise based on an Ettus E312 SDR [110, 109]. The development of a mobile, ground-based ice-penetrating radar system that uses several SDRs from National Instruments and Ettus is detailed in [80] and observed basal reflections from ice as thick as 800 meters.

To improve community access to large-scale ice-penetrating radar measurements, the Stanford Radio Glaciology Lab has developed the Open Radar Code Architecture (ORCA). ORCA is an open-source radar software codebase (available at https://github.com/radioglaciology/uhd_radar), which can be deployed on commercially available SDRs in the Ettus family [41]. This new codebase

provides researchers with the ability to build reconfigurable coherent ice-penetrating radar systems from commercially available components and included open-source hardware designs at a relatively low cost. Using this codebase, SDR-based radars can mimic characteristics of the most common airborne and ground-based systems in use today, democratizing access to ice-penetrating radar technology. We have deployed ORCA on two distinct SDR-based ice-penetrating radar systems: a mobile, ground-based system using an Ettus X310 [15] and an uncrewed autonomous vehicle (UAV)-borne system using an Ettus B205mini-i [142].

2.3 Prototypical Radar System

Fig. 2.1(a) shows a conceptual example of an ice-penetrating radar system deployed on an airborne platform. The nadir-looking radar emits an electromagnetic signal, often pulsed (e.g. [119, 155]), or in some cases continuous (e.g. [12, 98]). Some of the transmitted signal is reflected off the air-ice interface back to the receiver, while a portion of the signal is transmitted through the surface and reflects off subsurface dielectric contrasts, including internal layers and the ice-bed interface, before propagating back upwards through the ice column to the receiver. The radar system demonstrated in this paper is designed to emit a modulated waveform (for example, but not limited to, a linear frequency-modulated chirp) and to receive samples that are phase-coherent relative to each transmitted pulse. We use the terms pulses, chirps, transmissions, and waveforms interchangeably in this work. We refer to samples as the individual data points that make up a pulse, chirp, transmission, or waveform.

Because testing ice-penetrating radar equipment *in situ* is a logistically challenging endeavor, we primarily test our systems in a laboratory setting using a “loopback” configuration as shown in Fig. 2.1(b). In this setup the SDR transmit port is directly cabled to the receive port, with at least 30 dB of in-line attenuation added to prevent receiver damage. Varying lengths of coaxial or fiber optic cable can be used as delay lines to simulate round-trip propagation of the radar signals through ice ($v_{coax} \sim 1.98\text{e}8 \text{ m/s}$, $v_{ice} \sim 1.68\text{e}8 \text{ m/s}$).

Fig. 2.1(c) shows the results from a loopback test, where 100 m of coaxial cable is connected between the transmitter and receiver. The loopback peak is visible at an effective distance of 50 m. A direct path peak resulting from internal leakage of the chirp between transmitter and receiver is also visible at an effective distance of 0 m. We plot distances in terms of an effective distance, corresponding to the one-way distance to a reflector, as opposed to the round trip distance directly computed from the two-way travel time. The data in Fig. 2.1(c) was collected using a linear frequency-modulated chirp and processed using pulse compression, also called match filtering. The match filtering process produces sidelobes, which are visible in Fig. 2.1(c). The nature of the sidelobes is dependent on the amplitude of the transmitting waveform and can be modified by applying window functions to the pulse [60]. Beyond a distance corresponding to the pulse length,

the sidelobes end and the noise floor is visible.

2.4 Radar Code Architecture

The radar code is designed to repeatedly transmit a pre-generated waveform (such as a chirp) and receive synchronized returns (reflections) of these waveforms. In order to achieve the highest possible duty cycle, our code splits this task between two threads: a scheduler thread responsible for enqueueing commands for the SDR and a data-writing thread responsible for pulling received data from the SDR and storing it in persistent memory. The SDR-interfacing code is written in C++ and does not utilize any custom field-programmable gate array (FPGA) code, maximizing its flexibility and portability between different SDRs. Pre- and post-processing code is written in Python and described further in Sec. 2.8.

The Ettus SDRs use a system of first-in-first-out (FIFO) command queues for managing requested operations. These queues are implemented on FPGAs in each Ettus device, and execution of the commands has deterministic timing relative to the system clock. Commands can be assigned to run at specific times and will wait at the top of the queue to be executed until the assigned time is reached. Time-synchronized operations can be performed by enqueueing back-to-back transmit and receive commands with the same start times, or with a fixed offset. The command queues are relatively short in length and a failed command can quickly cascade into additional errors, so the state of the queue should be actively managed by the host computer, especially for high duty cycle operation.

In addition to managing the command queues, the host computer needs to pull data from the SDR and write it to some form of persistent storage. This process is limited by the host computer's processing power, the bandwidth of the interface between the SDR and the host computer, buffer space on the host computer, and a range of other factors that are dependent on the specific system architecture (e.g. the particular Ethernet or USB host controller and write speed of storage devices). Due to other processes running on the host, the exact rate at which data can be transferred and stored is effectively non-deterministic. Because of this non-determinism, our radar code uses a separate thread solely responsible for receiving and storing data from the SDR. The scheduler thread and data-writing threads are synchronized by simple counters that track the number of transmissions enqueued, the number successfully received, and any errors that occur. The overall architecture of the code is depicted in Fig. 2.2.

This separation of data storage (a highly buffered process with non-deterministic timing) and command scheduling (a minimally buffered process with tight timing constraints) is necessary to achieve high duty cycle operation. The command queue maximum lengths are quite short (eight commands on most Ettus SDRs), so the host software must continuously manage the queue to ensure that the next transit and receive commands are enqueued before their scheduled times. Because the

commands are small, they do not use much bandwidth over the link between the computer and SDR.

In contrast, retrieving the data from the SDR is a high bandwidth operation and the rate at which the computer can read and record this data can vary significantly as the operating system switches between the numerous processes being run on any standard computer. Data buffers, both on the SDR and on the computer, allow for this non-deterministic timing of reading data. By keeping this process separate from the command scheduling, this architecture greatly reduces the impact of delays in transferring data on keeping the command queues full.

2.4.1 Error Handling

When data is not transferred fast enough (resulting in empty or full buffers) or commands are not enqueued prior to their scheduled times, errors can occur (more details on errors can be found in Section 2.9.1). When an error occurs, it usually means that the host computer has fallen behind, leading to cascading errors. To mitigate this, the host code detects errors and temporarily increases the time before the next transmission to allow the host computer to catch up. Data about errors is stored in a log file so that post-processing code can reconstruct the exact timing of each transmission.

2.4.2 Data Storage, Metadata, and Configuration

After the desired number of pulses have been collected, the host computer directs the SDR to stop transmitting and recording, and begins the data storage process. Radar data is saved as interleaved in-phase and quadrature samples (IQ format), with bit depth dependent on the specific SDR used. Metadata is also saved at this time including the configuration file (described below), a log file, and optionally a GNSS file. The log file records errors encountered by the SDR during data reception, as well as the version of code used, which is required for post-processing. The GNSS file may be recorded when SDRs that accept GNSS input feeds, in particular those with GPS-disciplined oscillators, are used. In this case, radar data is timestamped with the GNSS time and GNSS positioning data can be recorded at a user-specified interval. All data and metadata files are timestamped with the date and time at the end of the recording.

At runtime, the user provides a configuration file in YAML format, specifying the desired radar and data storage parameters. The configuration file contains options for setting waveform related parameters (e.g. chirp type, window function, bandwidth, pulse duration, sample rate), SDR communications parameters (e.g. device IP address, clock frequency, data format), RF parameters (e.g. center frequency, receive and transmit gain, local oscillator offset, sample rate), and data collection/storage parameters (e.g. recording length, pulse repetition frequency, radar data storage location, GNSS data storage location, maximum file size). An option is also included to specify whether the system should transmit (i.e. be an active radar system) or only record data without transmitting (i.e. be a purely passive receiver). Default configuration files for example systems are included in the repository. A single configuration file fully defines the entire radar system, allowing the code

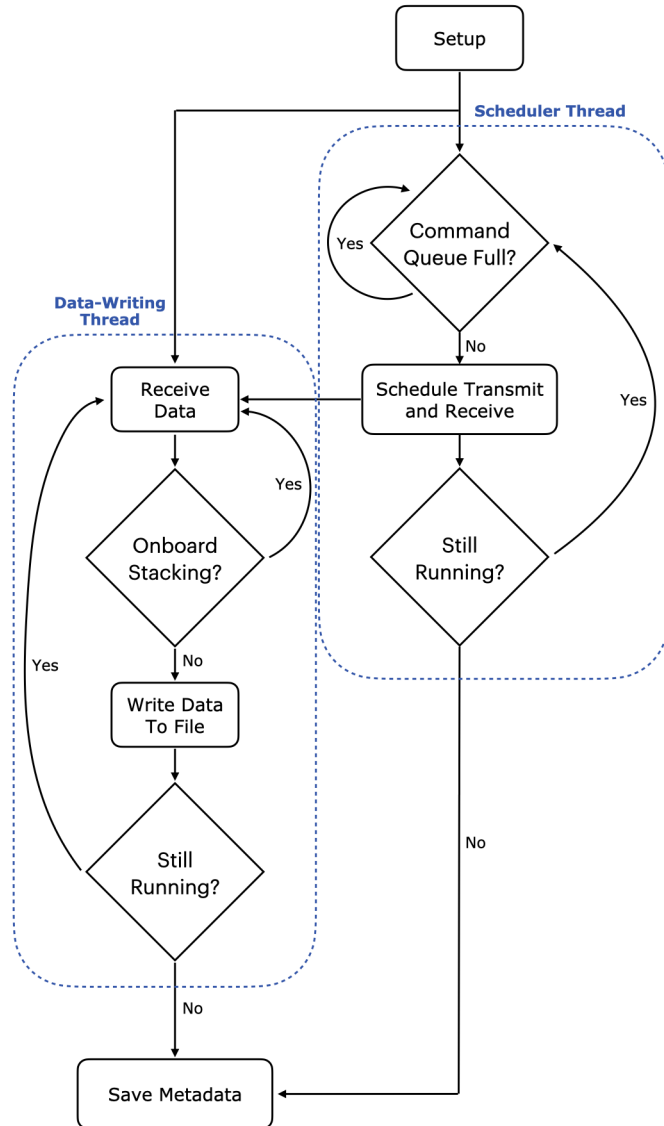


Figure 2.2: The radar code runs on a host computer and manages the SDR through two threads highlighted by dashed blue boxes: a scheduling thread responsible for managing the SDR's command queue and a data-writing thread that receives and stores data.

to be easily deployed on many types of SDRs. Furthermore, the configuration file is automatically saved along with the radar data, ensuring all necessary parameters for post-processing are readily available and facilitating the use of common post-processing code across multiple instruments. An example configuration file is included as a supplement to this article, and more configuration files can be found in the GitHub repository.

2.5 Signal Coherence Characterization and Analysis

Numerous processing methods have been developed and applied widely to ice-penetrating radar data to improve the signal-to-noise ratio (SNR) and/or resolution of targets within the ice [126]. A select number of processing methods have been developed for impulse radar systems [79], but because chirped airborne ice-penetrating radars have collected much of the existing radar data over the Greenland and Antarctic Ice Sheets, many more processing methods have been developed for and applied to coherent chirped radar data. These methods include, but are not limited to, both unfocused [107] and focused [78, 106, 62] synthetic aperture radar (SAR) processing, specularity analysis [125], layer-optimized synthetic aperture processing [21], swath imaging [101], interferometry [69], and polarimetry [70]. Crucially, all of these methods rely on phase coherence of the transmitted signal with the receiver, such that, for a given radar location and unchanging scene, the phase of the reflection, after cross-correlation, is unchanging with time.

Some confusion can result from the binary categorization of radar systems as “coherent” or “incoherent”. To help clarify, we distinguish between three common uses of the term coherence:

1. A **coherent radar system** is one in which the hardware is designed such that a transmitted signal reflecting off of a fixed set of targets is recorded with identical range and phase for each measurement.
2. **Coherent processing** is any post-processing done across measurements that relies upon the use of digitized in-phase and quadrature voltage signals (as opposed to using only the square or magnitude of the voltage signal) so that the coherence property of the radar, described in (1) can be used to improve SNR or resolution.
3. Particular imaged scenes or objects are sometimes called coherent, referring to either the predictability of phase changes as a function of time and/or space, or to constructive interference among multiple targets in a scene. These definitions are highly dependent on the imaging geometry and purpose of the data acquisition, however they are not properties of the radar system itself, so we do not consider them here.

While no hardware system is perfectly coherent, in practice, many systems, including ours, are close enough to being perfectly coherent that this subtlety can be ignored. For most applications,

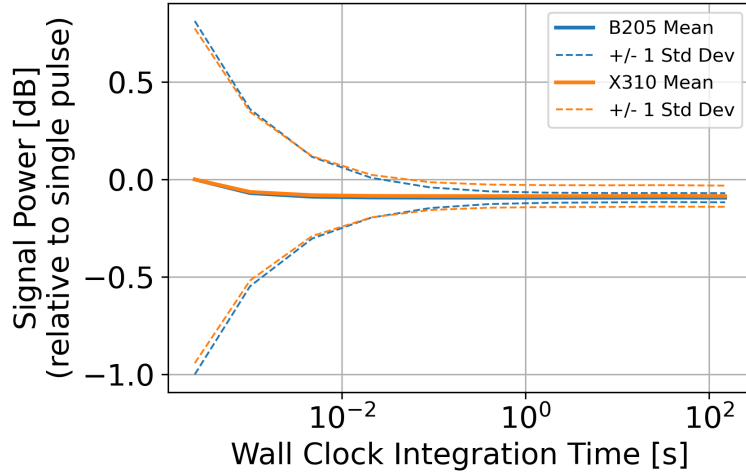


Figure 2.3: Signal coherence testing was performed for both SDRs in a loopback configuration. Mean signal power dips only slightly relative to the single recording (unstacked) mean. This indicates good coherence of the system.

if the drop in mean signal power with a large amount of stacking is small compared to the targeted SNR, the system may be considered coherent. As shown in Fig. 2.3, the drop in signal power is about 0.1 dB. The exact degree of system coherence varies with both the choice of SDR and configuration settings (e.g. sample rate and bandwidth).

In common SDR architectures, reduced signal coherence comes from phase noise, which is a manifestation of the timing jitter caused by drift within and between onboard clocks and local oscillator(s) [140]. We quantify the coherence of our systems by transmitting repeated pulses in the loopback setup shown in Fig. 2.1(b) and comparing the signal peak magnitude and phase when averaging over varying numbers of transmitted pulses. Fig. 2.3 shows these results as a function of coherent integration time, which is the elapsed wall clock time corresponding to the duration of measurements over which we average (wall clock integration time).

Theoretically, as long as signal power remains constant, every 10x increase in the number of coherently integrated pulses will result in a 10 dB increase in SNR (10 dB decrease in noise power) [2]. In our system, the power drops only slightly (0.1 dB) with increased stacking, as seen in Fig. 2.3(a), indicating good coherence. The slight drop in signal power of about 0.1 dB observed in Fig. 2.3 is a result of phase noise internal to the SDRs [140].

Another metric for evaluating coherence is to look at the long-term phase stability in a loopback setup. The variance of the phase of a reflection is commonly approximated as [146]:

$$\text{Var}(\phi) \approx \frac{1}{\text{SNR}} \quad (2.1)$$

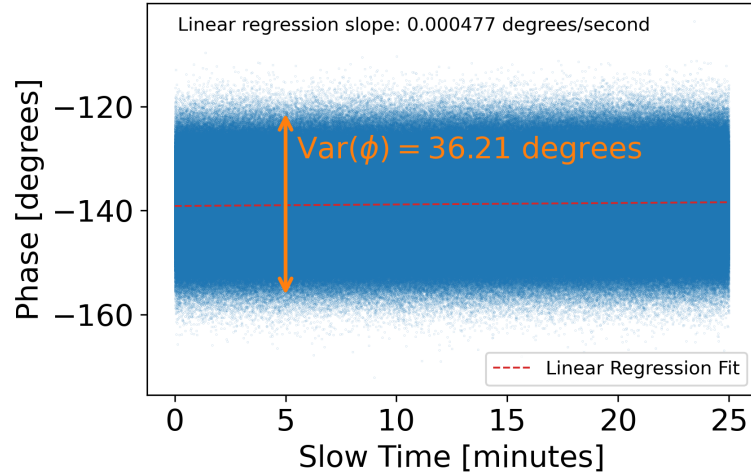


Figure 2.4: Single pulse variance of the reflection phase matches well to the expected $\frac{1}{\text{SNR}}$ value of about 33 degrees. Over a long recording, the system drift may be estimated by a linear regression over the phases. The observed drift of less than 0.5 millidegrees per second is inconsequential for most applications. Data collected on a B205mini SDR in a loopback configuration with approximately 20 dB single pulse SNR.

Fig. 2.4 shows measured phases of a loopback peak over a 25 minute recording. By fitting a linear regression to the phases, the phase drift can be estimated. If desired, this drift can subsequently be removed from the recorded data by multiplying the data with a complex exponential containing a linear phase progression that is the inverse of the estimated phase drift. For many ice-penetrating radar applications, particularly those utilizing moving platforms, this level of improvement in coherence may not be necessary. We note that care should be taken to ensure that phase drift estimated in field data is intrinsic to the radar and not a property of the scene being imaged.

2.6 Noise Source Characterization and Analysis

Ice-penetrating radars are affected by several types of noise including thermal noise, external environmental noise, quantization noise, and leakage from internal components such as switching power converters or local oscillators (LOs) [2, 111]. Noise sources may be described and modeled as incoherent (i.e. thermal) or coherent (i.e. speckle, LO leakage). Both types affect the radar's ability to detect small signals, but each type requires different mitigation approaches. While incoherent noise can be reduced through averaging, coherent noise cannot be, since it adds in-phase with the signal. Understanding the types of noise affecting the radar system and mitigating them appropriately is thus essential to improve the radar's performance in terms of signal detection and SNR. Table 2.1

Table 2.1: Potential noise sources affecting ice-penetrating radars and corresponding mitigation options.

Noise Type	Example Sources	Mitigation Options
Incoherent	thermal noise, power supply switching noise, background radiation, RFI	coherent summation (coherent averaging/stacking)*, RF front-end design, hardware filters, software filters*, shielding, antenna directivity
Coherent	local oscillators leakage, clock leakage, synchronization signals	phase dithering*, Hardware filters, software filters*, active cancellation

* Implemented as a pre- or post-processing option in the ORCA codebase.

shows an overview of noise sources that may affect ice-penetrating radars and options that exist to mitigate those noise sources.

Spectral analysis techniques may be used to determine relative contributions of different noise sources and to investigate a noise source's impact on a radar system's sensitivity. Alongside spectral analysis, a nuanced understanding of the radar system's architecture, and in our case, the architecture of the underlying SDR, is important to understand the system's noise characteristics.

2.6.1 Local Oscillator (LO) Leakage

Spectrograms are a powerful tool for understanding various noise sources that may be present in radar systems. Fig. 2.5 shows how various common noise sources may manifest themselves in spectral analysis. In Fig. 2.5(a) the impacts of LO leakage are clearly visible alongside a linear FM chirp. LO leakage is a form of coherent noise and limits the SNR gains achievable using pulse compression because the portion of the reference (transmitted) chirp centered around 0 Hz baseband is present in the received data at all delays, partially or wholly obfuscating reflections of the full linear FM chirp. To address the issue of LO leakage, the LO frequency can be tuned to a center frequency outside the chirp bandwidth, the digitally generated chirp signal can be moved away from baseband such that the LO contamination does not affect the chirp bandwidth of interest, or the frequencies corresponding to the LO leakage may be filtered out (using a notch filter) either during digital chirp generation or via analog filters in the front end. Our code provides support for any of these methods except the use of analog filters in the RF front end, as this would require a user-specific hardware implementation. While tuning the LO frequency outside of the chirp bandwidth either digitally or via RF/DSP tuning is an attractive option on the surface, it limits the available bandwidth that the chirped signal can occupy. This is because the sample rate of the system will be centered around the tuned LO frequency and the chirp will inherently be one-sided around this new

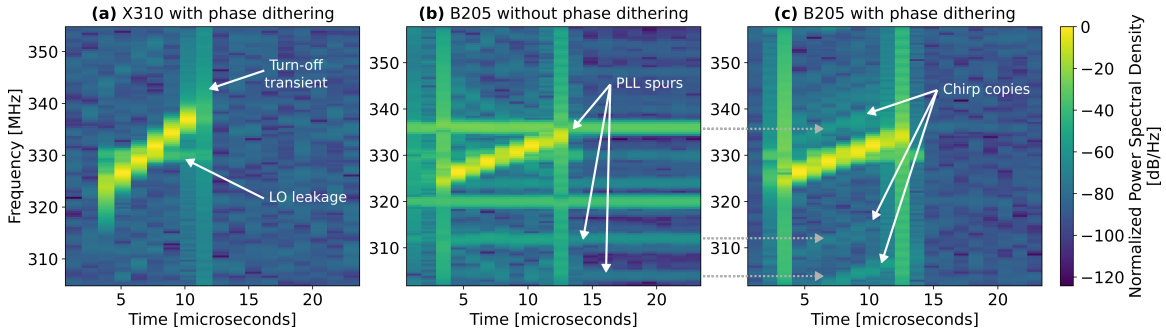


Figure 2.5: Spectrograms showing various artifacts that may occur depending on the selected configuration. (a) As with all quadrature transceivers, some leakage of the local oscillator (LO) into the output signal occurs. (b) The LO fed to the mixer is generated by a phase-locked loop (PLL), which contains frequency spurs depending on the exact configuration. (c) For the same settings except with phase dithering enabled, the LO and its frequency spurs are significantly reduced, however copies of the transmitted chirp centered at the frequency spurs remain in the signal.

LO frequency, as opposed to occupying frequencies both above and below the LO as before. While this may be an acceptable tradeoff in some applications, it is often desirable to maximize the chirp bandwidth to enhance range resolution [146]. In applications necessitating maximal bandwidth, we suggest users consider processing options that include a notch filter around baseband to alleviate LO impacts.

The Ettus SDRs all use phase-locked loops (PLLs) to generate the LO signals. Although an ideal LO contains only a single frequency, the PLL output used as an LO contains other frequency components, known as spurs [8]. The location and strength of these spurs depends on the reference oscillator frequency, the tuning frequency, and the design of the PLL. In general, we have found these spurs to be more problematic on the B205mini SDR, which always uses fractional-N PLLs. Fig. 2.5(b) shows examples of these spurs, with significant stacking applied to make these spurs visible. These spurs can be mitigated in stacked data by use of phase dithering (see Section 2.6.5), however, as shown in Fig. 2.5(c), if the spur was present in the transmit LO signal, copies of the chirp will be maintained after phase-dithering, centered on each spur.

2.6.2 Switching Noise

Noise from switching DC-DC power converters can also couple into the receiver system and is often difficult to detect in a spectrogram. Fig. 2.6(a) shows an example of this noise in the time domain when a commercial switching power supply is used in close proximity to the receive antenna. The roughly 2 MHz repetition frequency of the spikes corresponds to the switching frequency of the power supply. Note that there is no electrical connection between the power supply and the SDR in this test setup. The recorded noise is the result of radiated emissions. Switching noise is typically not coherent, but it still presents a nuisance for recovering and interpreting weak and/or distant

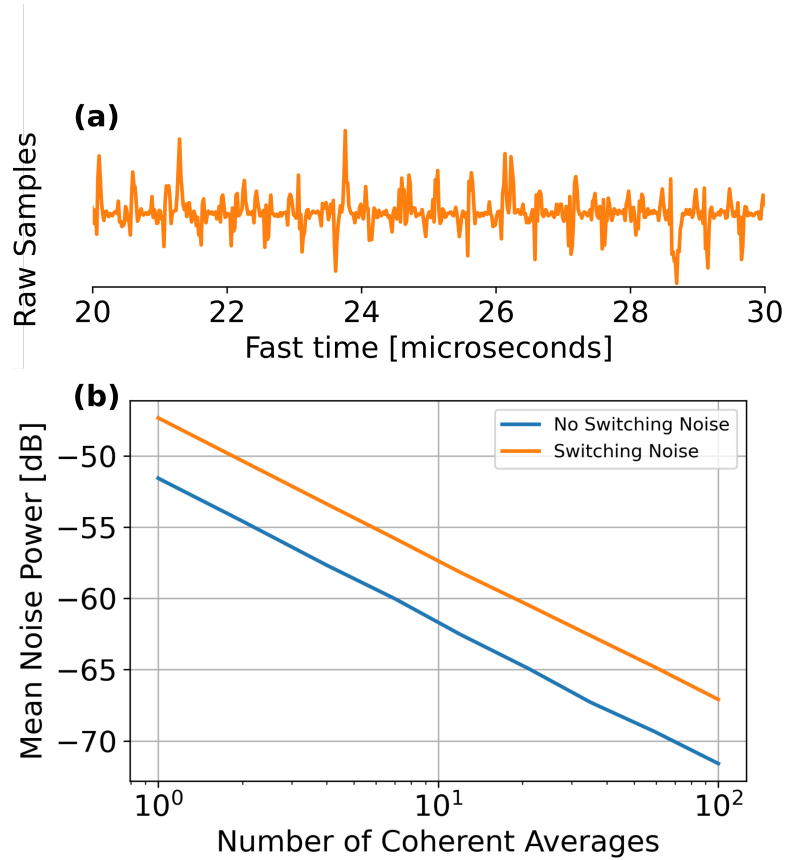


Figure 2.6: (a) Noise from a switching power supply presents in the raw time-domain samples as spikes at a rate of 2 MHz (the power supply switching frequency). (b) The effect of this is to increase the initial single-pulse noise floor. While the noise floor can still be reduced by coherent integration, starting at a lower noise floor is desirable to increase SNR for a given coherent integration time. Data collected on a B205mini.

reflections. As shown in Fig. 2.6(b), the switching power supply noise can be reduced by coherent summation, however the noise level for a given coherent integration length always remains elevated compared to the noise-free case. Switching noise from power converters is often best mitigated by improving the design of the power supply, making use of non-switching power converters, or including more effective shielding [111].

2.6.3 Radio-frequency Interference

External environmental (e.g. man-made) noise or radio-frequency interference (RFI) typically presents less of a problem for active radar systems as compared to passive ones (e.g. [4, 109]), but nonetheless can be a nuisance. The inherent flexibility of SDR-based radar systems provides several options for mitigating RFI. One option involves conducting a spectral scan at the field site and using statistical methods to determine which frequency bands have RFI contamination and which do not [109]. Then, only the clean frequency bands can be selected for use in the radar survey. Another option is to perform post-processing RFI removal to filter out in-band contamination prior to additional processing [109, 4].

2.6.4 Thermal Noise

Thermal noise (also called Nyquist noise or Johnson noise) is the noise generated by thermally-induced movement of bound charges, such as electrons [113]. The random fluctuations of thermal noise can be modeled as an additive white Gaussian noise source [32]. Because thermal noise is additive and incoherent relative to the radar signal, its impact can be reduced through averaging [2]. For complex-valued data, coherent averaging of N samples preserves the signal magnitude and phase, while reducing the mean noise power by a factor of N [2, 10]. Operating in a thermal noise-dominated regime is thus advantageous, because coherent averaging of data collected from a perfectly coherent radar system can in theory produce infinite decreases in mean noise power, and thus infinite increases in SNR. In reality, these performance improvements are finite, even for a perfectly coherent radar system, because eventually multiplicative noise such as clutter or sidelobes will become dominant over the remaining thermal noise.

Understanding the dominating noise regime at any given stage of the radar system and data processing pipeline is critical for systems without significant performance margins, as is the case in most SDR-based radar systems. Different noise regimes cause different limits on system performance and overcoming these limits requires distinct techniques depending on the primary noise source. Below we explore the impacts of coherent noise and how it is addressed in our radar platform.

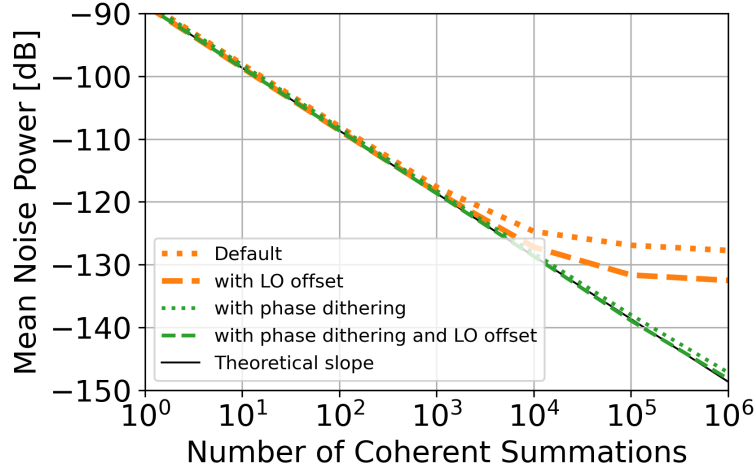


Figure 2.7: Mean noise power as a function of number of coherent stacks (averages). The thin dotted orange line shows a coherent noise dominated system, where mean noise power levels off as the stacking amount increases. Shifting the LO away from the signal (thick dashed orange line) allows for a lower mean noise power but the system still reaches a coherent noise limited state. The green lines (dashed with LO offset and dotted without LO offset) show the results of applying phase dithering to make the coherent noise sources incoherent. This keeps the system in an additive noise dominated regime and allows for additional coherent processing gain to be achieved. This data is collected on an Ettus X310. Exact results will change depending on the system and initial single-pulse SNR.

2.6.5 Phase Dithering to Overcome Coherent Noise

Most radar systems we envision being built upon this architecture will have the noise for each recorded pulse dominated by an additive noise source, such as thermal noise at the antenna. As long as the target(s) of interest remain phase coherent (i.e. are not moving in the scene), coherent averaging across multiple pulses can then be used to reduce the noise power level while keeping the signal power constant (coherent summation, as opposed to averaging, would result in increased signal power and constant noise power) [2]. As the noise floor decreases, however, the system eventually will become dominated by a noise source that is coherent with the transmitted and received signals. Clocks and oscillators internal to the SDR that leak directly into the transmitted or received signal may be such a noise source. Eventually, clutter or sidelobes may also appear to be a limiting coherent noise source. Because these noise sources are coherent with the radar system, the mean noise power will level off as additional stacking is performed. This is the case shown by the orange lines in Fig. 2.7. In this case, LO leakage within the radar system quickly moves the system out of an incoherent noise dominated regime into a coherent noise dominated one.

One approach for mitigating coherent noise used by some radar systems is phase dithering [2].

Phase dithering consists of applying a variable phase offset to each transmitted waveform and inverting that phase offset upon reception. This process effectively decorrelates coherent noise sources while maintaining coherency of the transmitted waveform. After inverting for the applied phase shift, received data can be coherently averaged to realize a factor of N increase in SNR (assuming thermal noise is now the dominant noise source).

Phase dithering can be implemented in a number of ways depending on how the radar is designed. For an SDR-based radar, no additional hardware is needed. Each transmitted chirp is simply multiplied by a complex exponential and the received data is multiplied by the inverse. Our code implements phase dithering by applying a pseudo-random phase shift in this manner. Phase shifts are generated using a seeded pseudo-random number generator and are undone prior to writing received data to storage. Apart from minor computational overhead, there is no downside to phase dithering on an SDR-based system. Phase dithering only helps however, once a coherent noise source becomes dominant. The point at which this happens can vary significantly between systems and is dependent on the initial single-pulse SNR.

Fig. 2.7 highlights the impacts of different noise regimes and how they can be mitigated. Without mitigation, the noise power eventually levels out as the LO's coherent noise dominates (orange lines in Fig. 2.7). Shifting the chirp away from the LO allows for reaching a lower noise floor (dashed orange line), however other clocks and spurs of the LO can still result in a coherent noise dominated regime. By employing phase dithering (green lines in Fig. 2.7), these coherent noise sources are effectively made incoherent, allowing the mean noise power to continue declining at the theoretically expected 10 dB per 10x increase in stacking, resulting in the ideal coherent processing gain of 60 dB for 1 million coherent averages.

2.7 SDR Calibration

Radiometric calibration of the SDR may be useful for some studies, including those that seek to quantify reflectivity of the ice-bed interface [26] or surface properties [52]. Microwave radiometers, which are deployed in polar regions to observe englacial temperature [154], are effectively non-transmitting radars and also require radiometric calibration of the SDR. In its most basic form, this radiometric calibration is a knowledge of the actual power (in physical units) transmitted out of the SDR, plus a mapping of the received power in SDR units to physical units. Both of these calibrations are primarily a function of the user-specified SDR transmit and receive gain, and to a lesser degree, are a function of frequency.

The relation between SDR transmit gain and physically transmitted power is provided by Ettus for most of the SDR systems they produce (e.g. [145]). We have found this data to be largely accurate and do not reproduce it here. This relation can be confirmed by transmitting from the SDR into a calibrated receiver. The mapping of measured to physical power on the receive side is

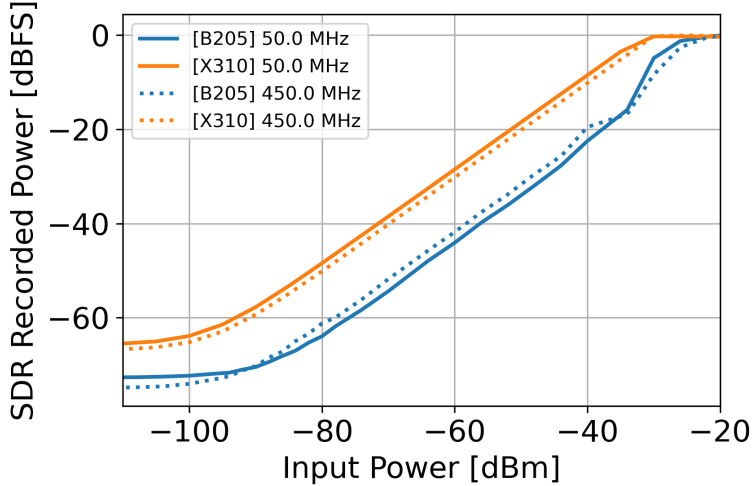


Figure 2.8: Mapping between received power in physical units (dBm) and SDR units (dBFS) for the X310 (receive gain 30 dB) and the B205mini (receive gain 36 dB). The X310 has better linearity and a wider dynamic range, making it more suitable to applications requiring radiometric precision.

done by transmitting from a calibrated source into the SDR. Fig. 2.8 depicts the resulting calibration curve for an X310 system at an SDR receive gain of 30 dB (orange) and a B205mini system with receive gain of 36 dB (blue). Different values of SDR receive gain shift this curve left or right and different SDR platforms have different dynamic ranges and linearity.

2.8 Processing Code

While the main focus of this paper is on the code that controls the SDRs and their behavior as radars, we briefly discuss the processing methods included within the ORCA repository for completeness.

The primary processing methods are written in Python, and example processing scripts are written in Jupyter Notebooks. Radar data is saved from the SDR into a binary file with samples in IQ format. We provide a method to read in the radar data, as well as associated metadata (i.e. the YAML file that catalogs the user-specified operating parameters), and convert the saved binary file into Zarr format, which is an open-source compressed file format meant for storing chunked, multi-dimensional arrays [158]. Converting the data to Zarr format slightly reduces storage requirements and is useful both for faster local and cloud-based processing. The radar data is loaded from the Zarr file into an Xarray Dataset, arranged by fast time sample index and slow time pulse index. The metadata from the associated YAML configuration file and reported errors that occurred during recording are loaded as attributes into the dataset.

Basic processing methods we include are stacking, which coherently averages together N pulses,

Table 2.2: Select Ettus SDR options as of Spring 2024 [41]

SDR	Frequency Range (GHz)	Bandwidth (MHz)	Channels	Mass (kg)	Cost
X310 with UBX 160	0.01-6	200	2 TX 2 RX	1.7	\$14,000
X410	0.001-7.2	400	4 TX 4 RX	2.7	\$28,000
B205mini	0.07-6	56	1 TX 1 RX	0.024	\$1,500
B210	0.07-6	56	2 TX 2 RX	0.35	\$2,200
N310	0.01-6	100	4 TX 4 RX	3.13	\$18,000

and pulse compression, which uses a copy of the analytic transmitted signal to implement a match filter on the received data. Example scripts we provide include a basic field processing notebook (Field Processing.ipynb) that loads data, views a single pulse of raw data (useful to check for clipping), performs stacking and pulse compression, and displays 1D and 2D radargrams. This script also displays the power spectrum and fast time spectrogram of the data, which are both useful for debugging RFI and other issues. We also provide an example script, similar to the one used to produce Fig. 2.7, to compute SNR-related statistics such as mean noise power and noise power variance, as a function of the amount of stacking. This script can be useful for evaluating the coherence of the system. Notebooks to reproduce each of the figures in this paper are also included in the repository.

2.9 SDR & Host Hardware Options

Our code can be deployed on any SDR in the Ettus family that utilizes a host computer. The E3xx series SDRs, which contain their own embedded computers, are currently not supported though, to the best of our knowledge, there is nothing preventing adaptation of our code to these platforms. Table 2.2 lists examples of several Ettus SDRs and some of their capabilities most relevant for ice-penetrating radar systems. For some ice-penetrating radar applications, the bandwidth may be particularly important. Higher bandwidth SDRs are well suited to resolving fine details in the near surface (“snow” radars) while the lower cost, lighter weight systems with less bandwidth may be more appealing if the primary goal is detecting the ice-bed interface. Our code may be adapted to use intrinsically lower bandwidth SDRs in a stepped-frequency architecture to synthesize larger overall effective bandwidths. For an end user with a specific target, platform, or radar requirement in mind, multiple SDRs may be sufficient to complete the task or only one may meet the user’s needs. We show this data, current as of early 2024, to demonstrate the range of choices one has in

SDR selection.

Beyond SDR selection, the choice of host computer can have a significant impact on the performance of the radar system. Each SDR has a specific set of communications protocols it supports for getting commands from and transferring data to the host. For example, the Ettus X310 can utilize either 1 Gb or 10 Gb Ethernet connected via an optical transceiver for host communication, while the B205mini is restricted to USB 3. Selection of the communications interface hardware is also an important consideration.

2.9.1 Performance Benchmarking

For many ice-penetrating radar applications, particularly those using relatively low-power transmitters, maximizing coherent processing gain is crucial for improving SNR. This means it is desirable to maximize the number of pulses transmitted (and received) in a given processing aperture. From a radar system design point of view, it is therefore important to design a radar capable of performing at a high pulse repetition frequency (PRF).

If the combination of SDR, communication interface, and host computer, is unable to perform at a given PRF, the most common behavior is that the command queue described in Sec. 2.4 becomes full of out-of-date commands and scheduling of data recording corresponding to each transmitted pulse results in a timing error (late command error). When this error occurs, data is not recorded for the error pulse. We note that we do not observe a loss of phase coherence between pulses before and after these errors.

Another error behavior sometimes observed (more commonly in scenarios with long pulse lengths) is the occurrence of overflow and underflow errors. These errors happen when the host either does not consume or does not produce data samples fast enough to keep up with the specified rate. These errors are addressed through careful choice of sample rates and performance tuning on the host side (e.g. by elevating thread priorities or writing to a RAM drive). For some applications and unavoidable host computer limitations, it may be necessary to utilize RF Network on Chip (RFNoC) blocks, such as the Replay block which utilizes DRAM on the SDR to buffer incoming and outgoing data, reducing the demands on the host computer [148].

Characterizing a realistically achievable maximum PRF is important for understanding the operating limitations of the radar system. In Fig. 2.9 we show the error rate achieved as a function of duty cycle and PRF for several SDR/interface/host computer combinations. Each error results in a small gap in data recording, so high error rates may pose issues for some post-processing algorithms. There is no hard threshold for what error rate is tolerable, but we treat an error rate of approximately 10% as an upper limit of what might be tolerable. In general, systems should be designed for much lower error rates if possible.

Fig. 2.9 shows that the limiting bandwidth is different for each SDR/interface/host combination. The X310 SDR connects to the host computer via a single 1 Gb, single 10 Gb, or dual 10 Gb Ethernet

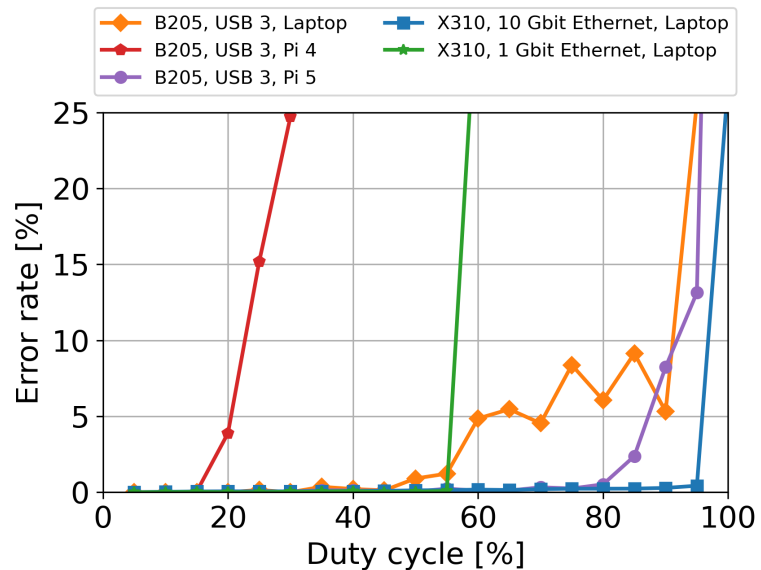


Figure 2.9: Error rate as a function of duty cycle for various combinations of SDRs and host computers: B205mini with laptop via USB3 (orange diamonds), B205mini with Raspberry Pi 4 via USB3 (red pentagons), B205mini with Raspberry Pi 5 via USB3 (purple circles), X310 with laptop via 1 Gb Ethernet (green stars), and X310 with laptop via 10 Gb Ethernet (blue squares). All data is collected in a loopback configuration, with a sample rate of 50 MHz for the X310 data and 56 MHz for the B205mini data.

connection. When the host computer has sufficient processing power (as is the case for our host computers) it is the bandwidth of the Ethernet interface that limits maximum sample rates on the X310 system. When connecting to the SDR via 1 Gb Ethernet, Ettus states the expected maximum sample rate for a single channel with 16 bit I/Q samples should be 25 Msps, while when using a single 10 Gb Ethernet connection the maximum sample rate for a single channel should be 200 Msps [1]. To achieve the full 200 Msps rate on multiple channels requires dual 10 Gb Ethernet [1]. We do not currently have a use case for and do not test full 200 Msps streaming from all channels using dual 10 Gb Ethernet.

Fig. 2.9 demonstrates that our code is capable of running at the respective data rate limits on the X310 with either 1 Gb or 10 Gb Ethernet connections. X310 loopback data in Fig. 2.9 were collected using a sample rate of 50 MHz, meaning that a 1 Gb Ethernet connection should only support duty cycles of approximately 50%, while a 10 Gb Ethernet connection should be capable of supporting 100% duty cycles. Operation at these limits is demonstrated by the green (1 GbE) and blue lines (10 GbE) in Fig. 2.9. Beneath the Ethernet data rate limit, error rates of less than 2% are reliably achieved.

For systems based on the B205mini SDR, which uses a USB 3.0 interface, achievable data rates are heavily dependent on the host computer’s specifications, especially the USB 3 controller. Use of a Raspberry Pi 4, for example, is possible but significantly limits the achievable duty cycle, as compared to use with a high performance laptop or even a Raspberry Pi 5, shown by the red, orange, and purple lines in Fig. 2.9, respectively. Users with applications that demand high PRFs should exercise caution when using SDRs with USB interfaces, as well as if using host computers with limited processing power.

2.10 Conclusion

The Open Radar Code Architecture (ORCA) is a powerful platform for developing ice-penetrating radar systems that we hope will enable more glaciologists to collect their own radar data. ORCA is an open-source codebase for running coherent, chirped ice-penetrating radars on software-defined radios (SDRs) within the Ettus family. ORCA includes options to overcome thermal noise impacts (via coherent stacking) and coherent noise impacts (via phase dithering and filtering). ORCA has been successfully deployed on two distinct systems developed by the Stanford Radio Glaciology Lab: Peregrine, a fixed-wing UAV ice-penetrating radar [142] and MAPPERR, a towed ground-based ice-penetrating radar system [15]. ORCA code, as well as open-source hardware designs and building instructions for Peregrine and MAPPERR are available at https://github.com/radioglaciology/uhd_radar.

Acknowledgment

The authors would like to thank NASA, the NSF, NDSEG, the Heising-Simons foundation, and Stanford University for financial and logistical support that made the development and testing of the described system possible.

T. O. Teisberg was supported by a NASA FINESST Grant (80NSSC23K0271). A. L. Broome was supported by the NDSEG Fellowship Program.

This material is based upon work supported by the National Science Foundation under Grant No. 284791. Field testing was supported by NASA under Grant 80NSSC22K0782.

Additional support was provided by the Heising-Simons Foundation, the TomKat Center for Sustainable Energy, Stanford Data Science, and the Stanford Institute for Human-Centered Artificial Intelligence.

Chapter 3

Integration of an open-source ice-penetrating radar with a low-cost fixed-wing UAV

3.1 Abstract

Ice-penetrating radar instruments are widely used to image englacial and subglacial features through ice sheets and glaciers. Existing instruments used in polar ice sheet research are primarily either ground based, towed by ski or snowmobile, or mounted on crewed aircraft. Ground-based systems suffer from a scalability problem, as they require the use of slow-moving ground vehicles guided by humans and are limited to areas that may be safely traversed. Airborne systems solve these problems, but their use is expensive and logistically complex, largely due to the use of crewed aircraft over extremely remote parts of the Earth. Here we present the development of a miniaturized ice-penetrating radar tightly integrated with a small, fixed-wing uncrewed aerial system (UAS). This low-cost, logistically lightweight system bridges the gap between ground-based and conventional airborne ice-penetrating radars, offering polar field teams a new tool for process-scale studies. Additionally, it serves as a testing ground for a next generation of more capable, longer range ice-penetrating radar UAS that can reduce the costs of large-scale polar radar remote sensing.

3.2 Introduction

The Earth’s ice sheets are the leading sources of uncertainty in models of future sea level rise by 2100 according to estimates from the Intergovernmental Panel on Climate Change [43]. This uncertainty arises from unknowns about the physics of ice flow and its interactions with the ocean and atmosphere

[131]. At the core of this uncertainty is a lack of subsurface data, limiting our ability to understand the dynamics of ice flow. Ice-penetrating radar (IPR) is the primary tool used to measure the subsurface properties of ice sheets and glaciers at large spatial scales. In order to operate at scale, IPR instruments are typically carried on crewed aircraft in order to image through englacial layering and bedrock topography along the aircraft’s flight path. Given the remote nature of the Antarctic and Greenland Ice Sheets (AIS and GIS, respectively), these survey flights are expensive and logistically complicated.

Advances in IPR data interpretation are opening new opportunities for understanding surface processes [20], hydrology [31], flow history [39], englacial velocity [73, 23, 143], and more, however realizing these opportunities will require collecting more IPR data, including repeat-pass measurements to detect changes. Expanding data collection and enabling persistent repeat measurements can both benefit from less expensive, automated, and uncrewed collection platforms. Uncrewed aerial vehicles (UAVs) are rapidly maturing and offer an opportunity to fill these data collection gaps, however significant challenges exist in equipping small UAVs with ice-penetrating radar.

Building off of an open-source IPR instrument architecture [139] and prior early prototype [141], we present a UAV-borne IPR data collection system. The Platform for Experimental Radio-Echo Geophysics in Remote Ice Navigation and Exploration (Peregrine) is 2-meter wingspan, fixed-wing uncrewed aerial system (UAS) designed for radar sounding of ice sheets and glaciers. Peregrine is a small-scale platform with a very light logistical footprint, suitable for deep field operations. In addition, it serves as a test-bed for solving the integration challenges associated with equipping IPR instruments on larger UAVs, including integration of antennas with small airframes, radar link budgets for power-constrained platforms, and flying in adverse environmental conditions.

In this work, we introduce the integrated architecture of the IPR instrument and aircraft, review field testing in Iceland, Svalbard (shown in Fig. 3.1), and Greenland, develop methods of estimating the performance of the radar instrument in a variety of locations and configurations, and discuss future developments for both Peregrine and larger-scale IPR-equipped UAS.

Historically, access to airborne IPR data collection has been limited to a few groups with the resources to build, maintain, and field highly custom instruments. In contrast, Peregrine is an open-source system, with design files for the IPR instrument as well as all modifications made to the UAV freely available. The entire system can be assembled for less than \$5000, putting Peregrine in reach of many polar fieldwork projects.

3.3 System architecture

Peregrine is built around an open-source autopilot and an off-the-shelf expanded polyolefin (EPO) foam airframe. The airframe hosts a radar sounder payload in the aircraft body, connected to transmit and receive antennas attached under the wings. Wherever possible, off-the-shelf parts were



Figure 3.1: A Peregrine UAS in flight over the Slakbreen Glacier in Svalbard. Peregrine is a 2-meter wingspan fixed-wing UAS with an ice-penetrating radar instrument. The red radar antennas are visible under each wing.

used to simplify production, however some modifications to the airframe are necessary for integration with the radar system and its antennas.

The radar sounder instrument is an open-source custom design based on ORCA [139] with a total mass under 400 grams for the instrument, excluding antennas. The details of the aircraft, antennas, and radar instrument are described in the subsections below.

3.3.1 Aircraft

The structure of the Peregrine UAS is built from the X-UAV Talon off-the-shelf remote-controlled (RC) aircraft kit, including the wing extension set for a total wingspan of two meters. The Talon airframe is a V-tail configuration with a pusher propeller. It is designed for hand launch and belly landings, which are both easily achieved on snowy surfaces. The aircraft avionics are based around the open-source PX4 autopilot running on a Cube Orange flight controller. All control of the aircraft can be fully automated using the PX4 software such that no human intervention is needed from launch to landing.

In addition to an electric motor and servos controlling the ailerons and rudervators, the flight controller is connected to a pitot-static tube for airspeed sensing, a laser altimeter, and a GPS receiver. Both the aircraft and the radar instrument are powered by lithium-ion batteries.

This airframe was selected because the EPO foam construction makes it relatively radio-transparent at relevant frequencies, the design of the body and wings provides for large spaces to mount instruments, and the availability of the foam parts has generally been good.

Several modifications to the airframe were necessary to accommodate electronics and antenna mounting. The carbon fiber spars are replaced by fiberglass spars and numerous 3D-printed mounts have been added. Details of these modifications, as well as source files for the designs, are available on the Peregrine website.

3.3.2 Antennas

The relatively low frequencies required to penetrate through ice pose a challenge for antenna integration with small UAS, as the size of the antenna generally scales with the wavelength. Wide bandwidths are also desirable to increase range resolution, which further complicates antenna selection. The SDR used in Peregrine supports 56 MHz of instantaneous bandwidth, so the design goal was to achieve more than 56 MHz of bandwidth centered below 500 MHz. This is accomplished using “edge-cut” bow-tie antennas, which can be thought of as a compromise between bow-tie antennas and dipole antennas in which a traditional bow-tie antenna is made narrower in width by symmetrically removing material from both sides.

The design process began with a conventional bow-tie antenna with a total length of 570 mm. The two sides of the bow-tie are connected through a 1:4 balun (TC4-1WX+, Minicircuits) to a coaxial connector. Versions of this design cropped to varying maximum widths were tested, both in simulation using Ansys HFSS and with laser-cut copper pieces adhered to a plastic backing. A 100 mm maximum width was selected as a compromise between feasibility of integration with various UAS platforms and bandwidth.

For ease of fabrication, this antenna is designed as a PCB antenna fabricated on a 0.6 mm thick FR4 substrate. This makes the antennas inexpensive to produce and less than 1 mm in finished thickness, facilitating easy integration with the UAS wing. The downside of this relatively uncontrolled fabrication process, however, is significant antenna-to-antenna performance variance that requires each antenna to be tested. Antennas are mounted to the underside of the UAV wings by means of plastic threaded inserts and plastic bolts. An antenna mounted to a wing and example S-parameter measurements are shown in Fig. 3.2.

As previously described, the wings of the aircraft are primarily made of EPO foam, making them largely radio transparent. Carbon fiber tubes in the wing are replaced by fiberglass tubes to minimize coupling between the antennas. Wires running to the servos controlling ailerons on each wing remain a source of coupling. Each servo wire set is wrapped twice through snap-together ferrite core (0461178281, Fair-Rite Products Corp.) to minimize this coupling.

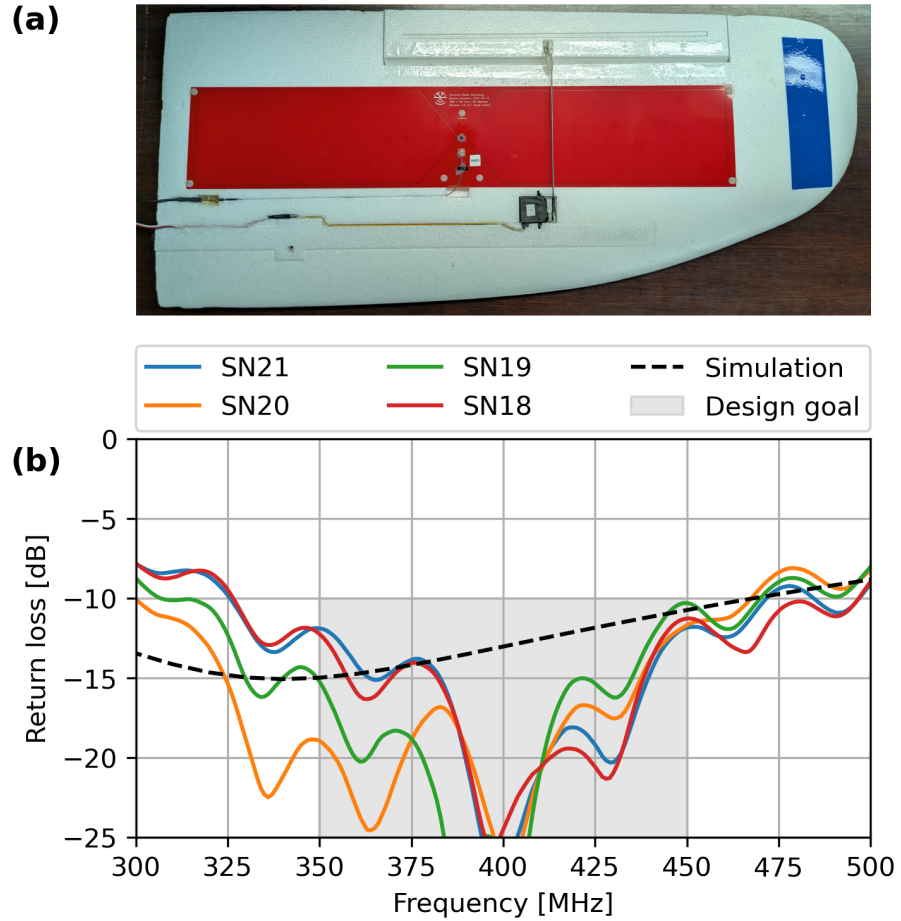


Figure 3.2: (a) Photo of an antenna installed on the under side of a Peregrine wing. (b) Comparison of return loss measurements for four copies of the same PCB antenna design, compared against the simulation results. While all satisfy the design goal, significant variation exists due to the manufacturing process.

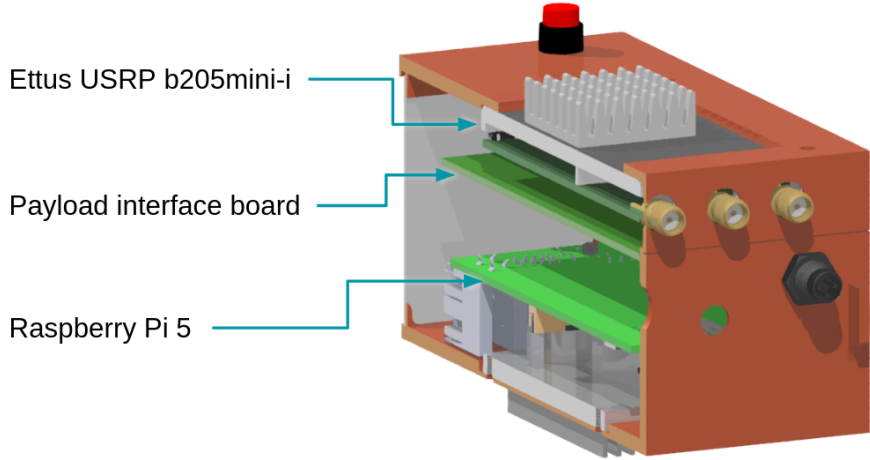


Figure 3.3: Cutaway view of the radar payload enclosure showing the SDR, Raspberry Pi computer, and interface electronics.

3.3.3 Radar sounder

Peregrine is equipped with a software-defined coherent ice-penetrating radar sounder. The radar payload is built around the Open Radar Code Architecture (ORCA) [139] and uses an Ettus b205mini-i software-defined radio controlled by a Raspberry Pi 5. On the receive side, a low-pass filter and an optional low-noise amplifier are used to improve signal-to-noise ratio (SNR). The enclosure containing the core radar instruments, a block diagram of the radar system, and key locations on aircraft are shown in Fig. 3.3.

As with all ORCA-derived IPR instruments, the system configuration is set by editing a simple YAML file. As such, multiple strategies may be employed depending on what is advantageous to the situation. Small UAS come with unique constraints which inform strategies configuring the radar sounder. In most cases, small UAS are constrained to fly below 120 meters by regulation. With only about 800 nanoseconds of round-trip travel time to the surface, constraining the transmitted pulse to be shorter than this would be a major limitation. Techniques such as multiple receive channels with varying gains or time-varying gain amplifiers require hardware that weighs too much for a small UAS. As such, it is desirable to be able to record without saturating while simultaneously transmitting. This permits reconstructing the surface reflection even if the transmitted pulse is much longer than the round-trip travel time to the surface.

In its default configuration, no external transmit amplifiers are used, giving Peregrine a maximum transmit power of just over 10 milliwatts. In practice, actual transmit powers are set such that the transmit pulse does not saturate the receiver, usually around 1 milliwatt. This low power can be compensated for in part by using extremely long pulses. If transmitting may continue while receiving

Table 3.1: Peregrine System Mass Budget

Component	Mass (kg)
Airframe, motors, and avionics	2.0
IPR sounder instrument	0.4
Antennas and cables	0.6
Batteries	0.7
Total mass	3.7

all relevant reflections, the main limitation on transmit length becomes motion of the aircraft during a transmitted chirp. Chirp lengths on the order of hundreds of microseconds can easily be employed to boost the SNR.

As an SDR-based radar sounder, Peregrine is also capable of transmitting a wide range of software-defined chirp waveforms. This includes arbitrary window functions as well hyperbolic chirps, phase-coded waveforms, or any other waveform design which may be advantageous to the measurement scenario. Although not yet implemented, different waveforms could be used adaptively, including in-flight to optimize SNR, range resolution, or other metrics.

The full radar instrument, including antennas and cabling, takes up about 1 kg of the overall aircraft weight, as detailed in Table 3.1.

3.4 Experimental results

The Peregrine system has been tested on several field campaigns to understand radar performance, platform capabilities, and user experience in real-world conditions. From 2022 through 2024, Peregrine was deployed over glaciers or ice sheets in Iceland, Svalbard, and Greenland. In addition to validating radar instrument performance, these test campaigns provided an opportunity to iterate on aspects of the UAV platform design and validate usability in a range of environmental conditions. Peregrine has successfully launched in wind conditions of up to 7 m/s and flown in estimated winds at flight altitude exceeding 10 m/s. The coldest operating temperature to date is -27.8 C. (Ground wind speed and temperature are recorded using a Kestrel 5500 portable weather station on a tripod at approximately 2 meters above the surface. In-flight winds are estimated from the PX4 autopilot's wind estimation.)

3.4.1 Case study: Slakbreen Glacier, Svalbard

The Slakbreen Glacier is a roughly 13.5 kilometer long mountain glacier, spanning an area of 41.5 square kilometers as of 2007 [74]. It was surveyed by airborne IPR in 1980 [37] and subsequently with a multi-frequency ground-based IPR in the 1990s [56], revealing ice thicknesses up to 320 meters and a reflecting horizon suggestive of a polythermal temperature structure, with a warm base due

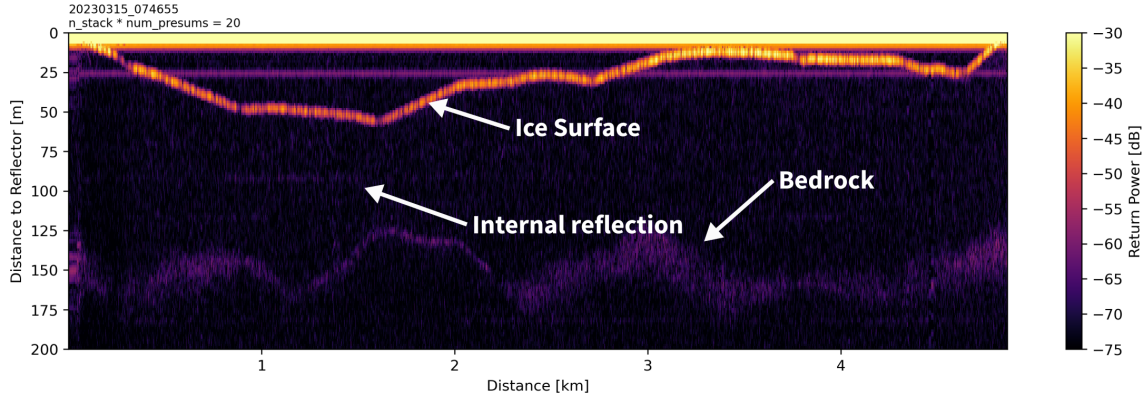


Figure 3.4: Example radar data collected over Slakbreen in Svalbard, showing reflections from the ice surface, bedrock, and an internal reflection.

to frictional heating [40]. The surface of Slakbreen is heavily crevassed, limiting safe travel across the glacier, especially along the glacial margins. Working from a flagged route along the center of the glacier, a Peregrine UAS was used to perform surveys perpendicular to the flow direction. The radar data collected, an example of which is shown in Fig. 3.4, shows the valley floor beneath the glacier as well as an englacial interface, likely caused by a transition from cold to temperate ice.

The Slakbreen field campaign is a representative example of the type of applications we envision for Peregrine. The lightweight logistical footprint made it possible to transport a Peregrine system to the glacier and deploy it on several flights with no additional infrastructure. Although the margins of the glacier were deemed too dangerous for human travel, Peregrine could be launched from a safe area and sent to autonomously collect data over the glacier margins.

3.4.2 Analysis of SNR

To compare results across field campaigns, it is most useful to focus on the ratio of the surface return power to the noise floor (the surface SNR). Englacial attenuation, scattering, and reflectivity can vary widely and are generally poorly constrained. In contrast, surface SNR is more straight-forward to compare across locations and can be used to estimate englacial SNR if englacial conditions can be estimated.

For a low-altitude airborne system, the strongest impact on surface SNR come from variation in altitude above ground (AGL). Target AGL can generally be selected by the operator, but a tradeoff must be considered between flying lower (for better SNR) and maintaining a suitable safety margin. This is especially important in glaciated regions where digital elevation models used in flight planning may be off by meters depending on what year and season the data was collected. Fig. 3.5 shows estimated surface SNR values versus AGL for a single flight over Slakbreen. To correct for this effect, a geometric spreading correction is applied to normalize each surface reflection strength to a

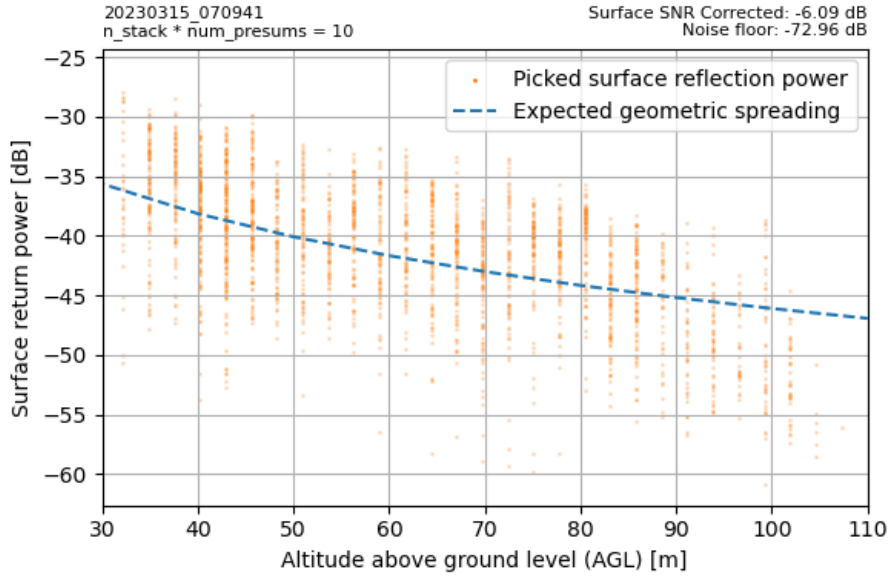


Figure 3.5: For low-altitude airborne IPR systems, altitude above the ground is a major determinant of surface power, due to geometric spreading. Surface reflection powers are plotted against altitude for one flight over the Slakbreen Glacier to demonstrate this effect.

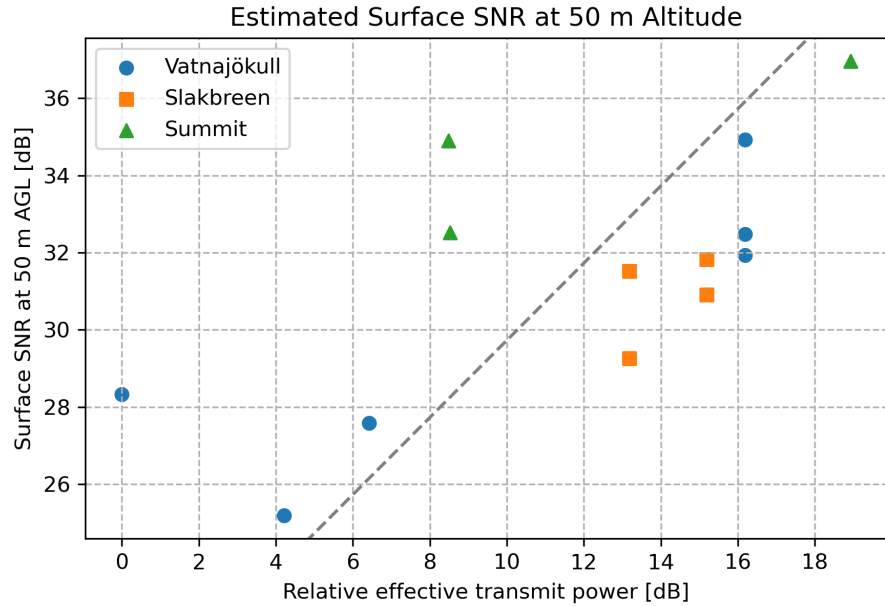


Figure 3.6: Surface SNR varies, in part, with software-defined radar settings, such as transmit power, window functions, and chirp length. Estimated relative effective transmit power based on these parameters is shown compared to estimated surface SNR at 50 meters AGL with unfocused coherent summation of 10 chirp recordings. Color and shape of each marker indicates the field site.

reference altitude, selected here as 50 meters:

$$P_{\text{dB, surf, 50 m AGL}} = P_{\text{dB, surf}} + 10 \log_{10} \left(\frac{\text{altitude}}{50 \text{ meters}} \right) \quad (3.1)$$

Software-defined radar systems can be rapidly reconfigured in ways that also impact the surface SNR. In addition to transmit power, the chirp length and transmit window function both impact the energy of the transmitted pulse. It is helpful to calculate an effective transmit power, taking into account the pulse compression gain expected for the specified chirp as well as the actual transmit power. Fig. 3.6 shows mean corrected surface SNRs for test flights versus this pulse-corrected effective transmit power. In addition to radar settings, surface SNR is also influenced by properties of the snow surface, so it is expected that effective transmit power only loosely corresponds to surface SNR.

For relatively thin mountain glaciers such as Slakbreen, only minimal coherent summation is needed to clearly see the bed. Thicker ice found on polar ice sheets, however, will require additional processing gains. Prior the Greenland deployment, a phase dithering approach was added to ORCA that makes coherent noise sources internal to the SDR incoherent with the radar chirp [139]. This feature enables the noise floor to continue dropping linearly with the number of coherent summations for much longer. Because this feature was added after the Iceland and Svalbard tests, we focus only on the Greenland data for the comparison of surface SNR versus coherent summation shown in Fig. 3.7.

3.5 Estimating radar performance

As a software-configurable instrument, the performance of the Peregrine radar may be tuned to a range of scenarios. If some other radar data is available to provide a required surface SNR, the surface SNR values presented here may be used as a rough guide to what basal SNRs are achievable, with appropriate scaling for radar settings and flight altitude.

The Peregrine test data collected near Summit Station, Greenland, shown in Fig. 3.7, is most representative of a configuration that would be used for polar ice sheet work. Using the approximate surface SNR of 50 dB for a 50 meter AGL flight, we can estimate the basal SNR over the AIS using a data-driven required surface SNR approach [128]. Peregrine is expected to achieve > 3 dB basal SNR across about 80% of the AIS's floating ice shelves. As expected, a small airborne platform is not suitable for bed mapping in most of the interior regions of the ice sheet. This does not necessarily mean that Peregrine may not be used in these areas, however, it simply means that bed reflections should not be expected.

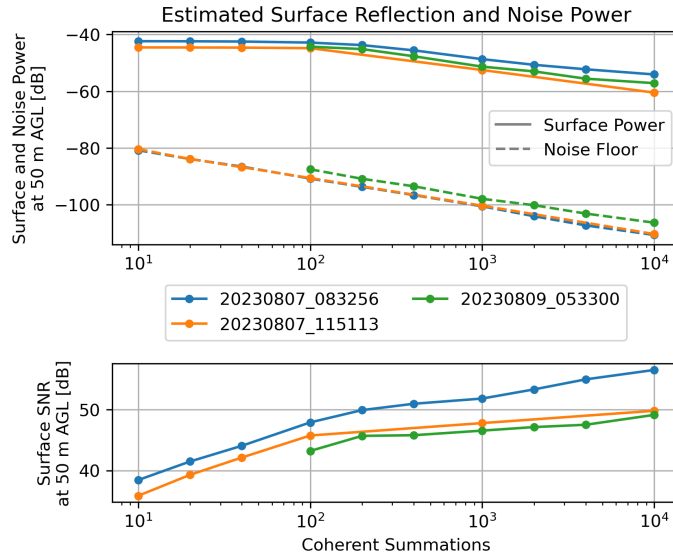


Figure 3.7: SNR increases with coherent summation applied to in-flight data collected near Summit Station in Greenland. Because no focusing is applied, the surface power eventually drops off, however the noise floor can still be seen to be dropping. Middle legend indicates unique flights used in the analysis.

3.6 Future work

Dealing with the massive dynamic range associated with imaging subglacial targets is one of the primary challenges of IPR instruments. The dynamic range between the surface reflection and the bed reflection can often exceed 100 dB without even accounting for geometric spreading [128]. For small UAS, this problem is made worse by the limited space for and between antennas. When antenna space is limited, the direct path (from the transmit antenna to the receive antenna through the air without reflection) is often stronger than the surface reflection, putting an even stronger constraint on dynamic range. IPR systems employ techniques such as blanking switches [81], time-varying gain amplifiers [28], limiters [66, 16], and interleaved chirps of different power levels or lengths [132] in order to improve their effective dynamic ranges. All of these tools are designed to allow for the use of high power transmit amplifiers to improve SNR, however they also come at the cost of reducing transmit duty cycle. In the case of an extremely small UAS, such as Peregrine, payload mass constraints limit the size of power amplifier that could be added anyway, making this an unappealing option relative to simply using longer, low power chirps.

With slightly more payload capacity, however, this calculation changes. A version of the Peregrine radar with a 100 W power amplifier has been developed and tested on the ground. This upcoming version uses a series of RF limiters and low-noise amplifiers in the receive front-end to prevent damage to the SDR from the direct path of these higher-power chirps. The tradeoff is that the system is

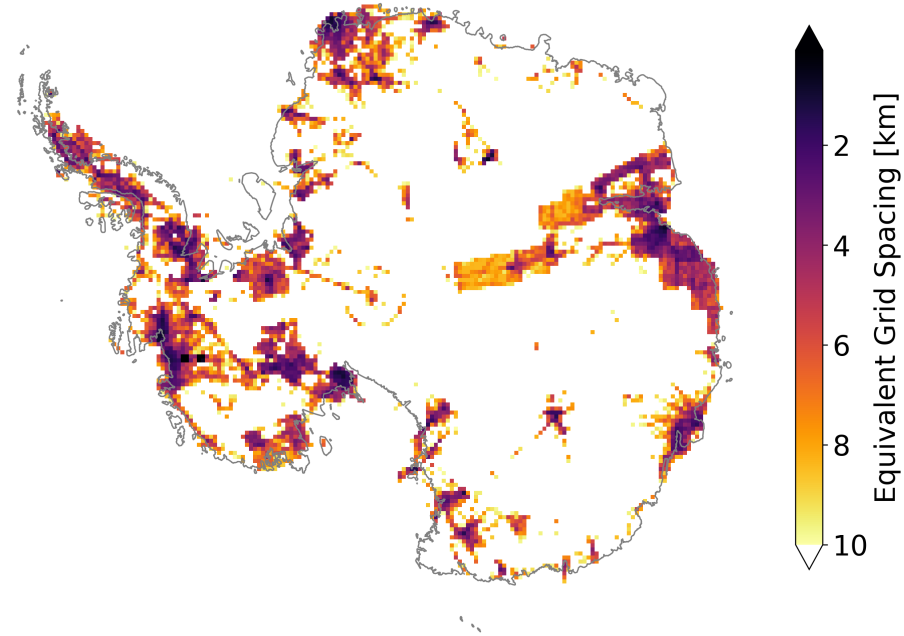


Figure 3.8: Equivalent gridded survey spacing of all available airborne IPR data collected, as represented in the BedMap 3 data release [44]. Despite decades of surveying, IPR data at high spatial resolutions is only rarely available.

effectively blind while the chirp is being transmitted, so chirps must either be kept extremely short or a sequence of interleaved high and low power pulses must be used to image both the near surface and deeper layers. An interleaved pulse sequence with two chirp powers carries an effective 3 dB penalty due to a 50% reduction in transmit duty cycle. This is, however, an easy price to pay if the mass budget is available to carry a power amplifier providing, for example, 40 dB of additional gain.

Overall, this next iteration of the radar instrument is expected to provide a roughly 44 dB higher SNR, however at a payload mass of 3 kg, it will require a significant step up in the size and complexity of the UAV platform.

3.7 Discussion

Peregrine is a starting point for changing how we think about IPR data collection. Traditionally, there has been a major division between airborne and ground-based IPR data. Airborne IPR systems used in polar regions have been flown on crewed aircraft, requiring pilots, engineers, and

ground support, in addition to the science teams operating the instrument and large quantities of fuel. These systems are expensive to build and operate, with only a few institutions controlling access to the instruments and data collection efforts being supported by the largest scale national and international grants. On the other side of the divide are ground-based radars, which are generally financially and logically in reach of smaller field teams but limited in the surveys they can carry out. Most of the ski or snowmobile towed radar systems are impulsive radars, which are processed differently from chirped radars and may not necessarily be temporally coherent [108, 92], limiting the ability to compare data collected from these systems with airborne IPR data. Bridging this gap to some extent is the ApRES, a ground-based coherent radar instrument designed specifically for glaciology [27, 69, 13, 99], however it is primarily used as a stationary instrument and significant limitations apply to using it as a mobile instrument [72].

The radar instrument on Peregrine is a coherent, chirped radar, operating in much the same ways that existing airborne systems work and capable of using the same post-processing techniques. Unlike existing airborne IPR systems, however, Peregrine costs less than \$5,000 USD and can be operated by a field team of just two people. Peregrine also enables data collection over areas that might not be safe for humans to traverse and collects data faster than typical snowmobile-towed surveying while fully automating the process of following a survey path.

A platform as small as Peregrine is in no way a replacement for crewed airborne IPR systems. Peregrine cannot compete with the range or SNR of these much larger platforms, however it provides a lightweight alternative anywhere that range and SNR are not the primary limitations. This may be especially beneficial to field teams interested in small-scale processes. Mountain glaciers, grounding zones, and areas with active near-surface hydrology are all examples are potential study sites that could benefit from the intermediate spatial scales of IPR data that Peregrine can collect. In most cases, existing airborne IPR data is not available at the kinds spatial resolutions that are needed for process-level work, as shown in Fig. 3.8, and temporal resolution of any kind is rare. As an automated system, Peregrine is extremely well suited to carrying out repeat measurements over days, months, or years. Gridded surveys may be planned with spacing less than 100 meters, due to the small turning radius of the platform. Once a survey has been designed once, repeating that data collection is a simple task.

3.8 Conclusion

In this paper, we have presented the design of a low-cost, airborne IPR data collection system that fills a gap between ground-based and expensive crewed airborne IPR systems. Peregrine carried a coherent, chirped IPR, similar in kind to existing crewed airborne radar systems commonly employed in polar fieldwork. It has been tested with a two-person field team in three polar environments, proving the platform capable of operations in real-world conditions. The small size of the platform

does introduce limitations, primarily on radar SNR and platform range. These limitations are discussed and the expected surface SNR is quantified based on analysis of field campaigns to date. We discussed how to extrapolate these results to future survey planning. Finally, we have discussed next steps for this project and the opportunities available for improving the SNR of upcoming version of this radar system on larger UAV platforms.

Code and Data Availability

The Peregrine radar system is based on ORCA, an open-source ice-penetrating radar architecture. Code is available at https://github.com/radioglaciology/uhd_radar and documentation at <https://orca.radioglaciology.com/>. Post-processing code used specifically to make the figures in this paper is located in the `postprocessing/notebooks/peregrine_paper` directory of the ORCA repository. Instructions for building a Peregrine system may be found on the ORCA website.

Acknowledgments

The authors would like to thank NASA, the NSF, NDSEG, the Heising-Simons foundation, the University Centre in Svalbard (UNIS), and Stanford University for financial and logistical support that made the development and testing of the Peregrine system possible.

Field testing in Svalbard would not have been possible without the support of Tor Arne Johansen. Field testing in Iceland was made possible by advice and logistical support from Helgi Björnsson, Finnur Pálsson, and Stephen Mantler. Danny Francis May and Eliza Joy Dawson assisted with field work in both locations. The photo in Fig. 3.1 was taken by Eliza Dawson.

T. O. Teisberg was supported by a NASA FINESST Grant (80NSSC23K0271). A. L. Broome was supported by the NDSEG Fellowship Program.

This material is based upon work supported by the National Science Foundation under Grant No. 284791. Field testing was supported by NASA under Grant 80NSSC22K0782.

Additional support was provided by the Heising-Simons Foundation, the TomKat Center for Sustainable Energy, Stanford Data Science, and the Stanford Institute for Human-Centered Artificial Intelligence

Chapter 4

Future developments in UAV-borne IPR

4.1 A perspective on the pathways for UAV-borne IPR

For years, UAVs have been offered up as the obvious next generation of platforms for ice-penetrating radar [85, 7]. Despite rapid advances in UAV technology and a number of technology demonstrations [85, 36, 141, 121], UAV-borne IPR systems are only just beginning to yield scientific results, and those results are, so far, mostly limited to mountain glaciers [121]. Much of this can be attributed to the significant challenges of operating any airborne system in polar regions. This situation continues to improve as UAV technology becomes more reliable and operational experience increases.

At the same time, new proposals are being put forward for alternative approaches to collecting IPR data. Among these, stratospheric UAVs (also known as high-altitude pseudo-satellites) and satellite constellations are being put forward as supplements to or replacements for conventional airborne data collection.

It is important to try to understand both the scientific goals of data collection as well as the capabilities and development paths of various possible platforms in order to understand where development efforts are best spent. Section 4.2 is intended to provide a framework for understanding the instrument capabilities that are achievable in the near future with different platforms and the capability levels that correspond to unlocking various types of new scientific results. Sections 4.3 and 4.4 provide specific suggestions for future work on the Peregrine UAV-borne IPR system and an in-development larger UAV that is designed to carry an ORCA-based IPR instrument, respectively.

4.2 Performance targets for UAV-borne RES

It can be useful to think about the capabilities of UAV-borne IPR platforms along three major axes:

- Signal-to-noise and signal-to-clutter ratios for relevant targets – Can the radar instrument see the targets of interest?
- Range, autonomy, and reliability – How much surveying can the platform achieve at what distance from a home base?
- Radar sounder capabilities – What relevant capabilities does the system have to support more sophisticated post-processing such as cross-track focusing ("swath"), radiometric analysis, interferometry, multi-frequency analysis, and polarimetry

For sub-orbital systems, signal-to-noise ratio is generally the primary limitation on what a radar sounder can see. (For more about this, see Section 1.3.) In this context, the required surface SNR (RSSNR) methodology, as introduced in Schroeder et al. [128], is helpful for system design.

For low-altitude platforms, it is important to note that required surface SNR is defined as the surface SNR needed to achieve a 0 dB SNR detection on the basal interface *after geometric spreading correction*. For orbital platforms, where the distance from the platform to the surface is much greater than the ice thickness, the geometric spreading correction is generally negligible. For low-altitude systems, however, it is not. Fig. 4.1 shows examples of how RSSNR relates to the uncorrected SNR needed on the ice surface interface for various altitudes and ice thicknesses.

Seeing the basal interface across 100% of each ice sheet is not necessarily the most important design goal for a UAV-borne IPR system. At least in the short term, UAVs are excellent platforms for tasks such as collecting precise repeat surveys or very dense grids but are less well suited to extremely long-range campaigns into the deep interior. This suggests that seeing through thinner ice around the grounding zones may be the more relevant design goal. Crewed aircraft can continue to be used to survey deep interior regions that change more slowly. With this context, we can break up the surface SNR targets by region. Fig. 4.2 shows the cumulative distribution functions of surface SNR needed to achieve a 0 dB basal reflection SNR. The surface SNR targets are shown for varying platform altitudes, to illustrate the effect of the geometric spreading correction.

Surveying range is also a critical platform consideration. For smaller-scale systems, the relevant questions are generally if the UAV can transit to the survey site of interest and how many line-km of surveying can be accomplished at the survey site per mission.

As UAV-based surveying evolves, it may be more helpful to think of a set of UAVs, perhaps stationed at different permanent research stations, as part of an observing system that could be coordinated to carry out targeted surveys in areas of interest.

Since grounding zones are often the fastest-changing areas and are especially important to estimating future sea-level rise, one interesting question is what UAV range would be needed to create

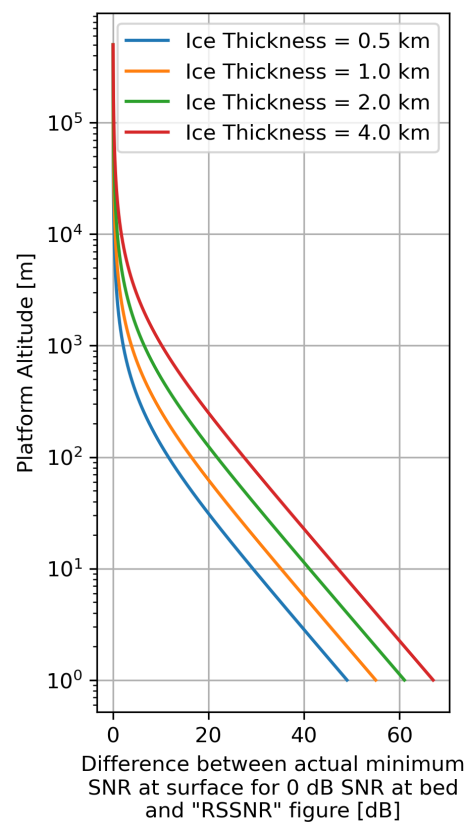


Figure 4.1: The additional geometric spreading correction needed to calculate the surface SNR needed for a bed detection is negligible at high altitudes but is critical to consider for low-altitude systems.

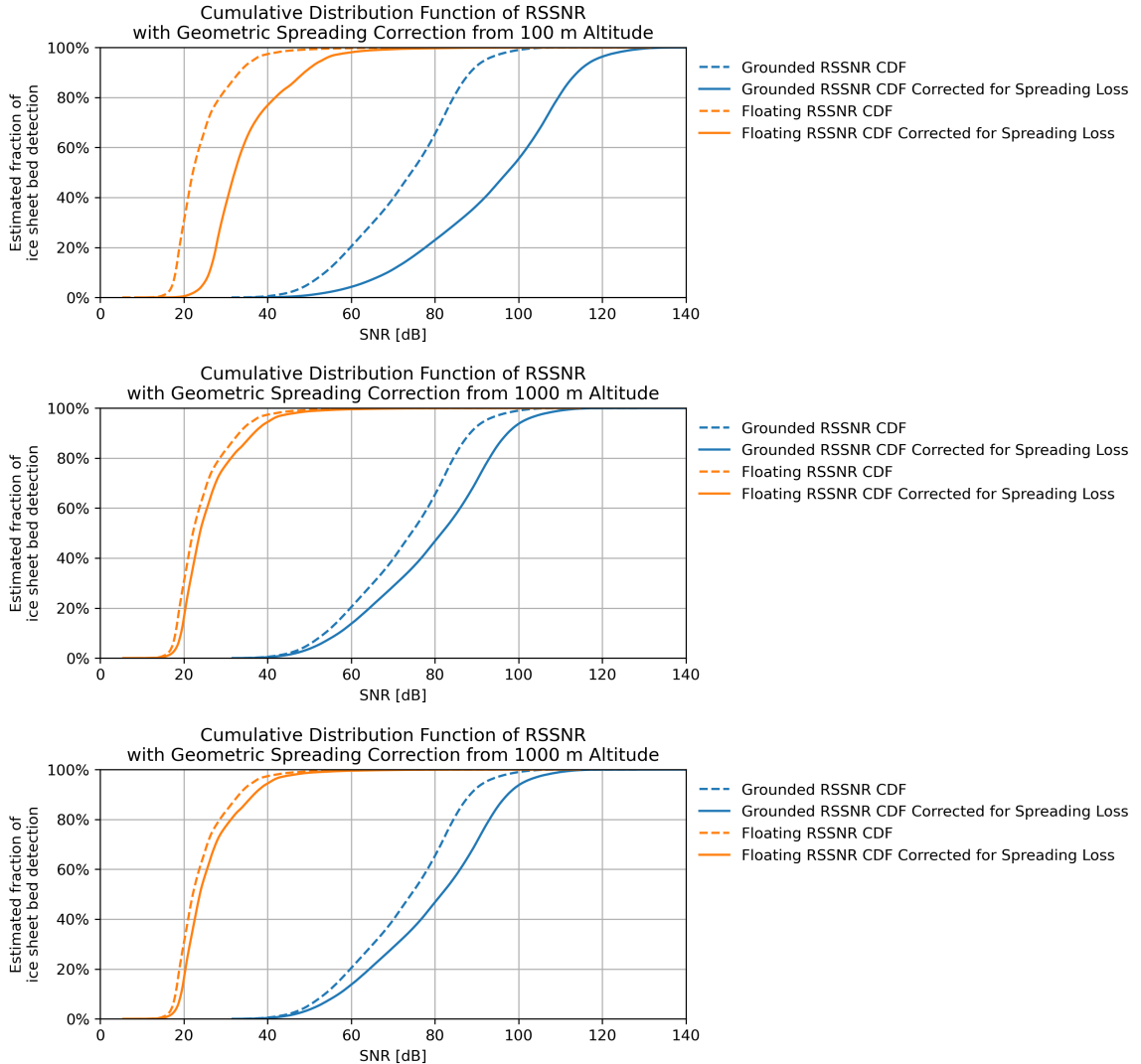


Figure 4.2: Cumulative distribution functions of required surface SNR (RSSNR) for floating (orange) and grounded (blue) parts of the Antarctic Ice Sheet along with corrections for platforms at varying altitudes. Data here is based on a similar Bayesian linear regression approach to the one described by Schroeder et al. [128] and comes from unpublished work in collaboration with Ellianna Abrahams.

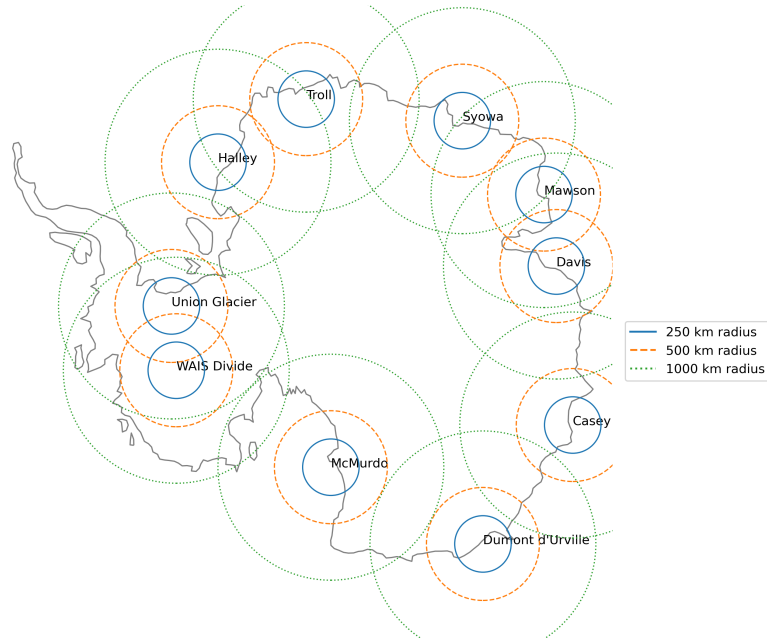


Figure 4.3: Hypothetic UAV maximum surveying range rings shown around selected Antarctic research stations to illustrate the capabilities of a UAV-based observing system if UAVs were deployed to numerous research stations in a coordinated way. The 250 km range ring roughly corresponds to the theoretical range of an EDGE Autonomy Penguin B VTOL UAV. The 500 km range range roughly corresponds to the range for the non-VTOL (fixed-wing only) variant of the same UAV. The 1000 km radius is roughly the range needed to fully fill in the entire grounding zone (except for small parts of the Antarctic Peninsula).

an observing system consisting of a fleet of UAVs permanently stationed at selected coastal research stations. Fig. 4.3 shows 250 km, 500 km, and 1000 km range rings placed over selected Antarctic research stations. West Antarctica is likely the limiting region, perhaps requiring longer range UAVs or the use of icebreaker-deployed UAVs to fill in the gaps.

The final capability to consider is support for advanced post-processing approaches. In some cases (such as multi-frequency support), UAV-borne platforms are no different from other systems. For array-based processing, however, the capability of UAVs to precisely perform extremely dense surveys should be considered as an alternative to large cross-track arrays.

4.3 System improvements for Peregrine

The Peregrine system is primarily limited by mass and volume constraints. As a very small UAS, there are limits to the achievable output power which limits the achievable SNR to some extent. As described in Chapter 3, Peregrine currently achieves about 50 dB SNR from a 50 meter nominal

altitude.

The starting point for improving the SNR on the Peregrine system should almost certainly be increasing the duty cycle and implementing some form of along-track focusing. Looking at the surface power and noise floor dynamics shown in Fig. 3.7, we can see that the noise floor is continuing to decrease at 10 dB per decade of coherent summation, however the surface power also being to decrease around 200 summations. This occurs when the surface phase is beginning to change over the coherent summation interval. There are two ways to improve this. First, the pulse repetition interval may be shortened so that less distance is traveled between pulses. The data shown in Fig. 3.7 was collected with a Raspberry Pi 4. As shown in Fig. 2.9, the Raspberry Pi 5 allows for a roughly 5 times higher duty cycle, which would support 5 times more coherent summation for the same amount of distance traveled. Integration gains can be further extended by implemented an along-track focusing algorithm, rather than simply summing up returns without phase correction.

The power output on the Peregrine system is currently limited by the constraint of not saturating the receiver. The receiver sensitivity may be changed, but adjusting the receiver amplification down in order to increase the transmit power is generally not beneficial. (In practice, the RX gain is set as low as possible before the noise figure greatly increases, which is an effect of the chained receive amplifiers internal to the AD9364. Above the RX gain where the noise figure stays relatively constant, it is better to keep the RX gain low so that the TX gain can be as high as possible such that the transmit power is high relative to any external noise sources.)

A way around this is to use an RF limiter, blanking switch, or some other mechanism. In any case, however, the data while the chirp is being transmitted and the receiver is saturated will probably need to be thrown out. Given the low altitudes, it is generally impractical to have the chirp transmission finish before the surface return starts coming back, so an interleaved approach is needed. In an interleaved approach, a lower power (or very short) pulse is used to record the surface and near-surface reflections, followed by a higher power (and/or longer) pulse that will saturate the surface but achieve sufficient SNR on deeper targets. The radargrams from these interleaved pulses may then be merged together. This approached, used by other airborne radar systems [28], works well but carries at least a 3 dB penalty, as half of your time is spent transmitting each type of chirp.

If the higher power pulse is much more than 3 dB higher power than what you could otherwise use, then this is still helpful. For Peregrine, with significant weight, size, and power limitations, this 3 dB penalty may be significant compared to a power amplifier that would be added. This tradeoff needs to be considered in any plan to add a power amplifier.

Any higher power system would likely require a new antenna design, as the current antenna design relies on a Mini-Circuits TX4-1WX+ balun with a maximum power handling capability of 0.25 W. In addition to increasing the power, there is certainly room for improvements in the antenna design. In particular, the antenna was initially designed when a number of UAV platforms were still under consideration and so had to meet the size constraints of the smallest. With the X-UAV

Talon wing, there is some space for the current antenna design to grow, which could likely be used to increase its directivity. To the extent that directivity also reduces antenna coupling, directivity is a double-win in that it also allows for higher output powers through the reduced coupling.

The full range of the Peregrine system has not been extensively tested or characterized. The use of Li-Ion battery packs has been tested and performs well. Since upgrading to using two Li-Ion 4-cell battery packs with a combined capacity of 7000 mAh, the full range of the system has not been tested. More work could be done here, and further improvements in flight time are likely possible.

Finally, the system is currently limited by the lack of any connection (other than power) between the radar payload and the autopilot. New capabilities could be unlocked by enabling in-flight radar settings updates and data preview.

4.4 Radar development roadmap for larger UAVs

A variant of the Peregrine radar is being developed for use on somewhat larger UAV platforms. This radar system increases the transmit power to 100 W and fits in an expanded mass budget of about 2.5 kg (as compared to 1 kg for the Peregrine radar, both including antennas and cabling). A prototype of this system was tested by towing it behind a snowmobile near Summit Station in Greenland in 2024 and was capable of seeing the ice-bed interface through approximately 3 km of ice. This section briefly describes the design of this new radar system so far, as it differs from the previously-described Peregrine radar, and provides some directional suggestions for where additional work would be beneficial.

4.4.1 RF front-end

The updated radar system uses the same radar payload but with an RF front-end capable of much higher power output. A block diagram of the RF front-end is shown in Fig. 4.4. This updated design achieved higher SNR primarily by adding a 100 W output power amplifier. In order to utilize this added power, the receive side has a series of low-noise amplifiers and limiters to prevent the high-power signal coming direction from the transmit antenna to the receive antenna (the “direct path”) from damaging any of the amplifiers or the SDR itself.

Assuming a noise figure of about 10 dB for the SDR on its own (which depends on the RX settings), the total receive chain shown here should achieve a roughly 1.9 dB noise figure, representing an improvement of over 8 dB in the SNR, in addition to the higher transmit power.

Assuming it is used in a pulse-interleaved mode where high-power pulses are alternated with low-power pulses used to image the near-surface, this updated RF front-end is expected to improve SNR by approximately 45 dB, after accounting for 40 dB higher transmit power, an 8 dB improvement in noise figure, and a 3 dB penalty for interleaved pulses.

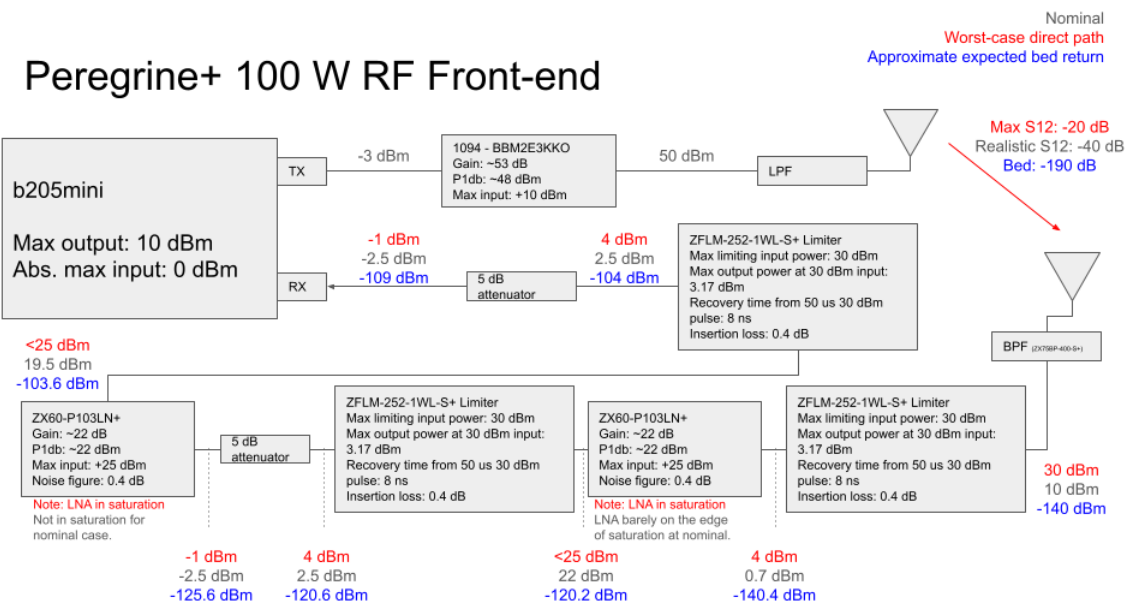


Figure 4.4: A block diagram of the as-tested RF front-end for adapting the Peregrine radar system to larger UAV platforms. Red, gray, and blue numbers show RF power levels at each component for three different cases of loss between the transmit and receive antenna. Red corresponds to the worst-case design scenario for maximum coupling between the antennas. Gray corresponds to a realistic direct-path coupling. Blue corresponds to a hypothetical attenuation of the signal returning from a reflection off of the ice-bed interface.

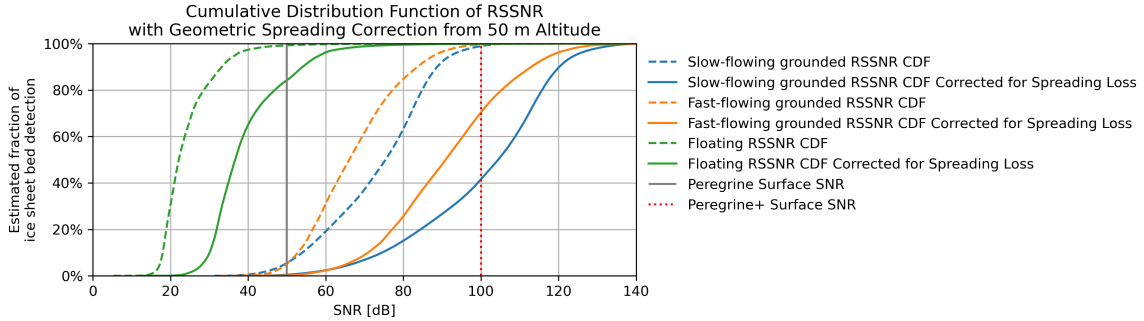


Figure 4.5: Cumulative distribution functions for RSSNR and altitude-corrected required surface SNR for floating ice, fast-flowing (≥ 100 m/year) grounded ice, and slow-flowing grounded ice (< 100 m/year), as compared with achievable surface SNRs for Peregrine and the updated version described here for larger UAVs (called "Peregrine+" in this plot).

The power amplifier used here (Model No. 1094, Empower RF, Inglewood, CA) was selected for its relatively high power to mass ratio and for the ability to quickly enter and leave a low-power shutdown state. Basic support exists in ORCA for trigger a GPIO output to put the amplifier in shutdown state between transmissions, which significantly reduces the overall power budget. This capability has not been extensively tested yet, and more analysis and testing is needed as available on-board power will likely be a limitation with this radar system.

For gas-powered UAVs, electrical power is usually provided by an on-board generator, possibly with battery backup. Because available power is dependent on engine RPM, it may be useful to built a tighter integration that allows the radar system to shut off or switch to a lower power state during phases where less power is available.

The selected amplifier is a class AB amplifier and is relatively efficient for an amplifier with good linearity properties. Lower mass and much higher efficiency could be achieved with a Class D or other fully non-linear amplifier. This comes with significant tradeoffs in distortion of the output signal, however it is worth further investigation.

Antenna design and cabling

Most larger UAVs rely on carbon fiber reinforcements for their wings, making the conformal design of the Peregrine antennas unsuitable. Instead, we have developed a number of Vivaldi antenna prototypes that are suitable for mounting under the wings or booms of larger UAVs. Designs for these antennas will generally need to be customized to each individual UAV. Panzer [102] provides some good general guidelines for the design process of these antennas. Vivaldi antennas can be made more directive than the edge-cut bowties used on the Peregrine system, which should enable 2-3 dB better directivity on each antenna.

4.4.2 Expected performance improvements

Combining the antenna improvements with the RF front-end, this version of the radar system should achieve a roughly 50 dB higher SNR as compared to Peregrine. As shown in Figure 4.5, this would enable surveying the basal interface from a 50 meter altitude across more than 60% of the fast-flowing grounded ice (≥ 100 m/year) on the AIS.

Chapter 5

Measurement of Englacial Velocity Fields with Interferometric Radio Echo Sounders

This chapter was published as:

Thomas O. Teisberg et al. “Measurement of Englacial Velocity Fields With Interferometric Radio Echo Sounders”. In: *Journal of Geophysical Research: Earth Surface* 130.6 (June 2025), e2025JF008286. ISSN: 2169-9003, 2169-9011. DOI: 10.1029/2025JF008286.
URL: <https://agupubs.onlinelibrary.wiley.com/doi/10.1029/2025JF008286>

Copyright Thomas O. Teisberg, Dustin M. Schroeder, Paul T. Summers, and Mathieu Morlighem, 2025. Licensed under Creative Commons BY-NC 4.0.

5.1 Abstract

The surface velocity of ice sheets is now measured at high spatial and temporal resolutions by satellite-borne platforms. The availability of this data has enabled rapid progress in both monitoring the evolution of ice sheets and understanding their underlying physical processes. Because the material properties of ice are spatially variable and poorly constrained, however, it is difficult to infer englacial velocity fields from surface velocity alone. Radio echo sounders, also called ice-penetrating radars, can image beneath the surface and resolve englacial layering, commonly assumed to represent isochronal surfaces. In limited settings, interferometric measurements of these englacial layers have also been used to infer vertical velocity within ice sheets, however these applications to date have focused on areas where layers could be assumed to be flat. Here, we develop the mathematical

relationships between observed englacial layer deformation and englacial velocity fields, making no assumptions about the shape of the layers and very minimal assumptions about the internal velocity structure. Taking this general approach opens up the possibility of using interferometric radio echo sounding to reconstruct three-dimensional englacial velocity fields at large scale across ice sheets. Potential applications of this method include data-driven estimation of ice rheology, inference of englacial conditions, and estimation of basal sliding. The proposed technique provides more direct constraints on these processes than has previously been available by remote sensing methods and offers the potential to both understand and predict the flow of ice sheets and glaciers.

5.2 Introduction

Radar interferometry is a well-established technique for precisely measuring the motion of reflecting interfaces over multiple observations. Airborne and satellite-borne radar systems use interferometric synthetic aperture radar (InSAR) techniques to track surface deformation and map surface topography [147]. Radio echo sounders (RES), also known as ice-penetrating radars, can also be used for interferometry, tracking the motion of reflecting interfaces within or beneath ice sheets, ice shelves, and glaciers relative to the radar's antennas. In the context of polar ice sheets, this technique was first employed to measure ice shelf melt rates by tracking the apparent motion of the ice-ocean interface with stationary radar systems [27, 69, 13, 99].

RES imaging of polar ice sheets also reveals semi-continuous englacial horizons, commonly known as layers, the origins and structure of which have been a subject of research since the earliest RES surveys [54]. Most work has focused on the use of layers for dating ice [82] or estimating historical flow patterns [120], but it is also possible to monitor the current motion of these layers using interferometric RES (InRES) [73, 23]. Because englacial layers tend to be relatively flat and are being advected with the ice's internal motion, phase changes must be interpreted as the result of both vertical velocity and horizontal advection of the layers, complicating the interpretation of observed vertical deformation measurements from InRES [156].

Although complicated by internal ice dynamics, InRES measurements of englacial layers are a compelling target for observing englacial motion. The composition, temperature, and crystal fabric all strongly influence the rheology of ice [75]. Because none of these variables are easily observable in-situ without drilling an ice core, the internal motion of ice in real-world glaciers remains poorly constrained and difficult to predict. Here we will show that InRES measurements of englacial layer motion provide a remote sensing observable that could be used to constrain englacial motion within glaciers and ice sheets.

The ability to create three-dimensional maps of englacial velocity structure holds the promise to rapidly advance our understanding of ice physics and directly improve ice sheet model initialization. Ice sheet surface velocity is used by large-scale models as a key constraint in inversion-based

initializations [77], in the estimation of bed topography [95], and in estimation of ice rheology [90, 117, 150]. In all of these applications, three-dimensional velocity data could be added in to existing frameworks to reduce uncertainties. Sub-surface velocity measurements also inform estimates of basal sliding velocities, a currently under-determined parameter which may be critical to predicting ice sheet evolution [34].

In this work, we develop a mathematical foundation for connecting InRES-observed englacial layer motion and englacial ice velocity. We show how, with an appropriate survey design, InRES measurements can be used to reconstruct three-dimensional englacial velocity fields, and we discuss the noise sources impacting these measurements and how this should inform RES instrument design. Finally, we present simulated velocity reconstruction experiments and explore potential applications of InRES surveys, including quantitative estimates of ice rheology and basal slip.

5.2.1 Englacial layering in radio echo sounding

Continuous englacial horizons identified in radio echo sounder data, representing contrasts in the dielectric properties of the ice, have been attributed to a number of physical phenomena including changes in density (only applicable in the near surface), chemical composition, crystal fabric orientation, and inclusions of other materials such as volcanic ash [134].

Under most interpretations, englacial layers represent isochronal surfaces [134] and thus their structure has been interpreted to convey information about the flow history of ice by comparison of their shape to forward model results [152, 47]. Notably, englacial layers are the product of the entire flow history they have experienced. Thus, there is no one-to-one mapping between a single temporal observation of layer geometry and the contemporaneous flow field [103].

5.2.2 Prior work in radio echo sounder layer interferometry

The isochronal nature of englacial layers implies that we can treat these layers as material surfaces, meaning that we assume no mass is transported through a layer boundary. If these layers are assumed to be flat or not in relative horizontal motion, then a time series measurement of the vertical motion of a layer provides a measurement of the local vertical velocity within the ice. Note that the no relative horizontal motion criterion requires both that the horizontal velocity is uniform with depth and that the instrument is advected at the same horizontal velocity (Lagrangian measurement), which may be achieved either by tracking the surface velocity (for airborne systems) or by anchoring the instrument to the surface. This is the principle behind using stationary ground-based radar systems, such as the Autonomous Phase-Sensitive Radio Echo Sounder (ApRES), to measure basal melt on ice shelves [27, 69, 13, 99].

This use of radar interferometry to measure deformation of englacial layer motion has been extended with ground-based measurements to observe the Raymond effect near ice rises [73], estimate motion and orientation of dipping layers [156], and for measurements of firn compaction [20].

The technique has also been shown to work with repeat-pass airborne radio echo sounding data [23, 89, 6, 5]. Airborne repeat-pass interferometry generally differs from ground-based measurements in that airborne repeats tend to follow an Eulerian measurement approach, tracking measurement over time at a fixed location, whereas ground-based systems are generally advected with the surface of the ice and thus make Lagrangian measurements. When airborne measurements are collected along surface flow lines, they may be processed from either an Eulerian or Lagrangian perspective, however in this paper we will focus on the Eulerian frame of reference.

In all of these cases, the study design focuses on areas where it is reasonable to expect that either the layers are relatively flat and/or that the variation in horizontal velocity with depth is negligible. These assumptions do not always hold, however, and complex sloping layer geometries can be found that do not match present-day surface velocity fields [39]. Non-zero layer slopes have been identified as a source of ambiguity in such interferometric measurements [156]. Similar to the use of snapshot layer geometry to infer flow history through data-model comparison, inversions can be used to extract velocity data even with sloped layers by imposing sufficient regularizing constraints on the rheology [137].

5.3 Interferometric measurement of englacial layer deformation

We begin by reviewing the measurement of englacial layer deformation with InRES and deriving the relationship between measured layer deformation and the englacial velocity field.

5.3.1 Notation

We use a Cartesian (x, y, z) coordinate system, with z pointing upwards vertically. The velocity field of the ice is represented as $\mathbf{v} = (u, v, w)$. We identify surface quantities with a subscripted s , such that surface velocities are represented as $\mathbf{v}_s = (u_s, v_s, w_s)$ and z_s is the z coordinate value at the ice upper surface.

We treat layers as material surfaces, consisting of the same particles of ice at all times. Each layer is defined by a function $l_i(x, y, t)$ such that the phase center of the dielectric contrast occurs along $l_i(x, y, t) - z = 0$ at time t , where i is the index of the layer. We generally omit the subscript i for notational simplicity.

InRES measures the vertical deformation of each layer function $\frac{\partial l_i}{\partial t}(x, y)$. Critically, this observed layer vertical motion at a specific location is not, in general, equivalent to the vertical velocity of a particle of ice at that location. As illustrated in Fig. 5.1, horizontal advection of a layer with a non-zero slope produces a non-zero $\frac{\partial l}{\partial t}$ even when there is zero vertical velocity.

When it is convenient, we also introduce a simplified two-dimensional flowline geometry. Here we

introduce an approximation that the horizontal velocity vector at any location is equal in direction (but not necessarily in magnitude) to the surface velocity. We represent the scalar relationship between the velocity at depth and the surface velocity as a function $s(x, y, z)$:

$$\begin{aligned}(u, v, w) &= (s(x, y, z)u_s, s(x, y, z)v_s, w) \\ s(x, y, z = z_s) &= 1\end{aligned}\quad (5.1)$$

At any given location, we can equivalently represent this by rotating the coordinate system by an angle β about the z axis such that the local x axis, x_f , points along the map plane direction of surface flow and the layer slope in this direction is α :

$$u_f = \sqrt{u^2 + v^2}$$

$$\tan \alpha = \nabla l \cdot \frac{\mathbf{v}}{|\mathbf{v}|} = \frac{u \frac{\partial l}{\partial x} + v \frac{\partial l}{\partial y}}{u_f} \quad (5.2)$$

In this geometry, we use coordinates (x_f, z) with velocity field (u_f, w) . We begin with the three-dimensional case and make clear where we use the two-dimensional flowline approximation.

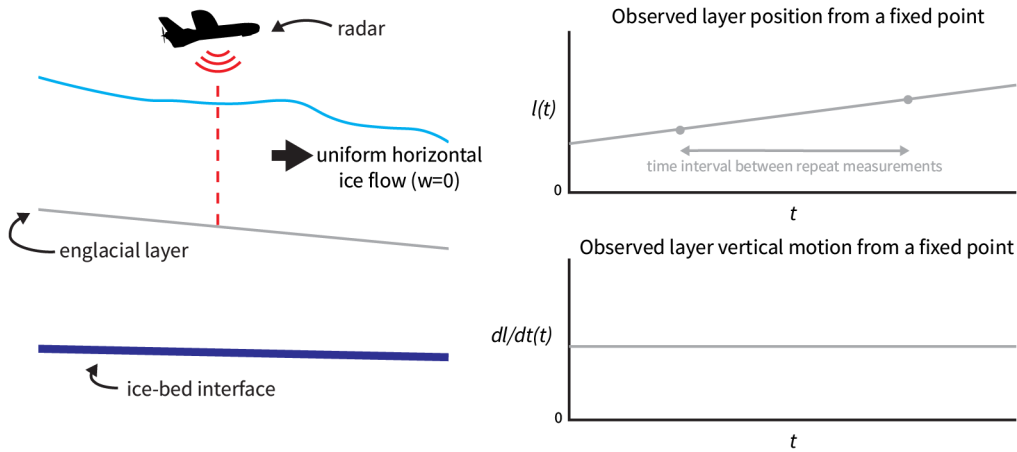


Figure 5.1: Even with zero vertical velocity, horizontal advection of sloped layers produce an apparent vertical motion of the layers from the perspective of a radar system observing from a fixed position.

5.3.2 Estimating the three-dimensional englacial velocity field

For an ice particle located on a layer boundary described by $l_i(x, y, t)$, the functional $F_i(x, y, z, t) = l_i(x, y, t) - z$ will always evaluate to zero when evaluated along the path of a particle contained in the i -th layer since $l_i(x, y, t) = z$ for all particles in this layer. Therefore, the material derivative of this functional will always be zero for particles contained in the layer. From this relationship, we find an expression relating apparent layer motion and horizontal advection:

$$\frac{DF_i}{Dt} = \frac{\partial F_i}{\partial t} + \mathbf{v} \cdot \nabla F_i = \frac{\partial l}{\partial t} + u \frac{\partial l}{\partial x} + v \frac{\partial l}{\partial y} - w = 0 \quad (5.3)$$

We assume that ice below the firn is incompressible, such that $\nabla \cdot \mathbf{v} = 0$. This implies that $-\frac{\partial w}{\partial z} = \frac{\partial u}{\partial x} + \frac{\partial v}{\partial y}$. Differentiating with respect to z and substituting the result into the incompressibility constraint provides a first-order PDE in 3 dimensions (x , y , and z) with two dependent variables (u and v):

$$\frac{\partial^2 l}{\partial t \partial z} + u \frac{\partial^2 l}{\partial x \partial z} + \frac{\partial u}{\partial z} \frac{\partial l}{\partial x} + v \frac{\partial^2 l}{\partial y \partial z} + \frac{\partial v}{\partial z} \frac{\partial l}{\partial y} + \frac{\partial v}{\partial y} + \frac{\partial u}{\partial x} = 0 \quad (5.4)$$

Here we have taken the partial derivative $\frac{\partial^2 l}{\partial t \partial z}$ to be a finite differences approximation of the derivative with respect to z of the $\frac{\partial l_i}{\partial t}$ functions.

All of the partial derivatives of l can be determined from (In)RES radar data, either from single-pass estimation of the layer geometry or, for the time derivatives, estimated by the change between repeat measurements. Unfortunately, Equation 5.4 is underdetermined, requiring an additional constraint to separate u and v .

In this work, we introduce an assumption that the horizontal components of the velocity field are always aligned with the horizontal components of the surface velocity, as described in Section 5.3.1.

Using Equation 5.1, the original PDE in Equation 5.4 can be re-written in terms of a single variable $s(x, y, z)$, representing the scalar relationship between u and v components of the velocity field and the surface velocity.

$$\begin{aligned} \frac{\partial^2 l}{\partial t \partial z} + s u_s \frac{\partial^2 l}{\partial x \partial z} + u_s \frac{\partial s}{\partial z} \frac{\partial l}{\partial x} + s v_s \frac{\partial^2 l}{\partial y \partial z} + v_s \frac{\partial s}{\partial z} \frac{\partial l}{\partial y} + s \frac{\partial v_s}{\partial y} + v_s \frac{\partial s}{\partial y} + s \frac{\partial u_s}{\partial x} + u_s \frac{\partial s}{\partial x} = 0 \\ u_s \frac{\partial s}{\partial x} + v_s \frac{\partial s}{\partial y} + \left(u_s \frac{\partial l}{\partial x} + v_s \frac{\partial l}{\partial y} \right) \frac{\partial s}{\partial z} = - \left(u_s \frac{\partial^2 l}{\partial x \partial z} + v_s \frac{\partial^2 l}{\partial y \partial z} + \frac{\partial v_s}{\partial y} + \frac{\partial u_s}{\partial x} \right) s - \frac{\partial^2 l}{\partial t \partial z} \end{aligned} \quad (5.5)$$

This reduction of the PDE to one dependent variable allows it to be solved by the method of characteristics. The characteristic curves, parameterized by τ , for Equation 5.5 are defined by:

$$\begin{aligned}\frac{dx}{d\tau} &= u_s \\ \frac{dy}{d\tau} &= v_s \\ \frac{dz}{d\tau} &= u_s \frac{\partial l}{\partial x} + v_s \frac{\partial l}{\partial y}\end{aligned}\quad (5.6)$$

Because $\frac{dx}{d\tau} = u_s$ and $\frac{dy}{d\tau} = v_s$, the characteristic curves projected onto the x-y plane follow surface flow lines. If the starting point for each characteristic curve is selected to be on a layer, then the characteristic curves are the projection of any surface velocity flow line onto any continuous layer. This is a useful property that can simplify data collection and analysis.

Using the chain rule and our choice of characteristic curves, we find that $\frac{\partial s(\tau)}{\partial \tau}$ is equal to the left hand side of Equation 5.5:

$$\frac{ds(\tau)}{d\tau} = \frac{\partial s}{\partial x} \frac{\partial x}{\partial \tau} + \frac{\partial s}{\partial y} \frac{\partial y}{\partial \tau} + \frac{\partial s}{\partial z} \frac{\partial z}{\partial \tau} = u_s \frac{\partial s}{\partial x} + v_s \frac{\partial s}{\partial y} + \left(u_s \frac{\partial l}{\partial x} + v_s \frac{\partial l}{\partial y} \right) \frac{\partial s}{\partial z} \quad (5.7)$$

This allows us to find that the solution to Equation 5.5 reduces to an ODE along any characteristic curve, as defined by Equation 5.6:

$$\frac{ds(\tau)}{d\tau} = - \left(u_s \frac{\partial^2 l}{\partial x \partial z} + v_s \frac{\partial^2 l}{\partial y \partial z} + \frac{\partial v_s}{\partial y} + \frac{\partial u_s}{\partial x} \right) s - \frac{\partial^2 l}{\partial t \partial z} \quad (5.8)$$

Because the characteristic curve follows a surface flow line, any cross-flow layer slope will be zeroed out by the dot product of the surface velocity with the layer slopes. Thus, this may be further simplified by substituting in the along-flow horizontal velocity u_f :

$$\frac{ds}{d\tau} = - \left(u_f \frac{\partial^2 l}{\partial x_f \partial z} + \frac{\partial v_s}{\partial y} + \frac{\partial u_s}{\partial x} \right) s - \frac{\partial^2 l}{\partial t \partial z} \quad (5.9)$$

This solution form implies that it is possible to solve for horizontal velocity by integrating along any surface flow line projection onto any continuous layer. Thus, the input data needed may be acquired from a single flight line, flown twice or more at different times, provided that the flight line follows a surface velocity flow line and that enough layers may be continuously traced to estimate the partial derivatives of observed layer motion in Equation 5.9.

The ODE tends to be stable if the surface flow field is divergent, which is the case across much of the Antarctic and Greenland Ice Sheets. Stability properties are addressed in more detail in Section 5.9.

5.3.3 Boundary conditions

Solving Equation 5.9 requires a boundary condition. Since the ODE is solved along each layer, this requires knowing the horizontal velocity somewhere along a continuous section of each layer. Without any approximations, these boundary conditions can only come from ice divides (where the horizontal velocity at all depths is zero) or from in-situ borehole measurements. In practice, there may be other sources of boundary conditions. If the layers trace a continuous path to a fast-flowing area or onto an ice shelf, it may be sufficient to assume the horizontal velocity throughout the ice is equal to the surface horizontal velocity, though this final value boundary formulation has implications for ODE stability. In principle, it may also be possible to estimate the transformation matrix for a sufficiently unique feature within the ice, in a manner similar to how feature tracking is used to infer surface velocities by correlation [159]. Finally, the zero-slope approximation, discussed in Section 5.4, may provide alternative boundary conditions.

5.4 Zero layer slope approximation

Up to this point we have drawn a clear distinction between vertical layer motion at a point and vertical velocity of the ice at that location. If, however, layers can be assumed to be flat, this allows for simplifications of the relationship between vertical layer motion at a fixed point and vertical velocity. Substituting the along-flow notation from Equation 5.2 into Equation 5.3, we see how the horizontal velocity u_f and layer slope α contribute to the observed layer motion:

$$\frac{\partial l}{\partial t} + u_f \tan \alpha - w = 0 \quad (5.10)$$

Taking the z -derivative to solve for vertical strain rate, we find:

$$\frac{\partial w}{\partial z} = \frac{\partial^2 l}{\partial t \partial z} + \frac{\partial u_f}{\partial z} \tan \alpha + u_f \sec^2(\alpha) \frac{\partial \alpha}{\partial z} \quad (5.11)$$

The challenge in applying this equation is that the magnitude of the horizontal velocity, u_f , is generally unknown, except at the surface. If we neglect the terms involving the horizontal velocity (for example, by assuming that $\alpha = 0$ for all layers), then we can view any non-zero values of the latter two terms of Eq. 5.11 as error terms. Illustrations of the effects of these two error terms are shown in Fig. 5.2.

In this paper, all measurements are taken to be in an Eulerian frame of reference, however we briefly depart from this convention to note that the error behavior is notably different from a Lagrangian measurement, such as one taken from an instrument anchored to the ice surface. From a Lagrangian reference, the along-flow velocity u_f in the $u_f \sec^2(\alpha) \frac{\partial \alpha}{\partial z}$ would be replaced by the relative motion between the radar platform and the englacial interface. In a Lagrangian measurement, this error term is thus reduced by the horizontal velocity of the radar across the surface. For a more

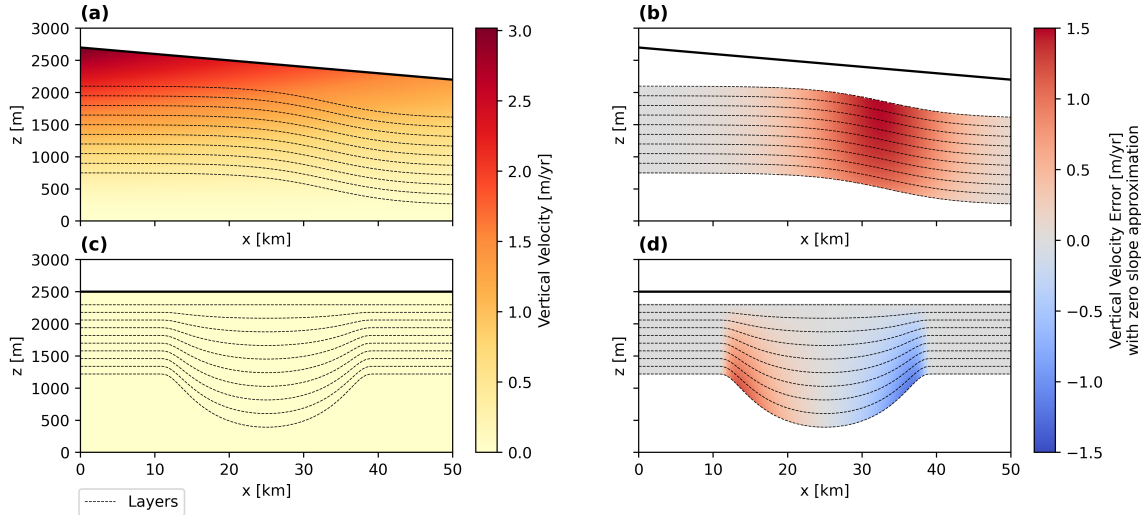


Figure 5.2: Synthetic cases showing the error introduced in vertical velocity estimation by the use of the zero-slope approximation. Dashed lines represent the locations of synthetic layers, constructed to illustrate each error term. The solid black line represents the surface. In the case shown in the top row (a-b), the layers are parallel, but the vertical strain rate is non-zero. Where the layers dip down (non-zero slope), there is an error in the estimated vertical velocity. In the case shown in the bottom row (c-d), the horizontal velocity is uniform throughout (plug flow) but there is variation in the layer slope with depth. Where this variation occurs, a positive or negative vertical velocity is incorrectly estimated.

detailed treatment of observed layer motion from a Lagrangian perspective, we refer to Young et al. [156].

In general, these errors can only be geometrically corrected if a full three-dimensional model of both the layer geometry and the horizontal velocity are known. For the purposes of estimating vertical strain rate, the latter requirement is, presumably, never satisfied. If, however, the goal is to measure melt rates on an ice shelf or another location where the horizontal velocity may be assumed uniform with depth, then geometric corrections, as discussed in Young et al. [156], are sufficient even if layer slopes cannot be assumed to be zero. The magnitude of potential errors from the zero-slope approximation can be estimated from a simple ice-sheet model. An example of model-derived error estimation is shown in Section 5.10.

5.4.1 Interpolation between zero layer slope areas

Assuming some noise in the measurements, errors will accumulate as Equation 5.9 is integrated from a boundary condition, so it is desirable to find areas of known horizontal velocity along the path to avoid long stretches of integrating error. The zero-slope approximation may offer one approach to finding the horizontal velocity in some locations.

If the layer slopes are zero (or, as discussed in Section 5.10, very close to zero), then Equation 5.11 may be used to find the vertical strain rate without integration. If a top or bottom surface boundary condition for horizontal velocity is known, the vertical strain rates may be integrated using conservation of mass to find horizontal velocity through the ice column. If some areas along a flow line can be identified where Equation 5.11 can be used independently to find horizontal and vertical velocity, these values may serve as boundary conditions for integrating Equation 5.9.

5.5 Radar measurement model

Coherent radio echo sounder systems measure reflections of a transmitted wave off of dielectric contrasts, including englacial layers [13]. Assuming that one reflection dominates the return in a given range cell, the phase of the returned signal ϕ_0 contains sub-range-cell information about the distance to the phase center of the reflecting interface [13]. Two spatially coincident measurements separated by an offset time can be interfered to measure the relative phase $\Delta\phi = \phi_1 - \phi_0$, where ϕ_1 is the phase measured on the second measurement from the same location at a later time. This relative phase contains a signal related to the motion of the target between the two acquisition times:

$$\Delta\phi = \frac{-f_c \sqrt{\epsilon_r} 4\pi}{c} \Delta R + \phi_{\text{noise}} \quad (5.12)$$

In this relationship, f_c is the radar center frequency, ϵ_r is the relative permittivity of the medium of propagation, c is the speed of light in vacuum, ΔR is the observed change in range to the layer interface, and ϕ_{noise} is the combined contribution of thermal noise at the time of each measurement. Because we are considering only relative motion beneath the firn, we can assume ϵ_r to be a constant (see Section 5.5.4 for more detail).

Due to geometric uncertainties in the sensor location (repeat pass misalignment) and the layer phase center (off-nadir reflections due to sloped layers), the observed change in range is assumed to contain some noise, which will be discussed, along with the previously mentioned thermal noise, in Section 5.5.1.

$$\Delta R(x, y, \Delta t) = l(x, y, t + \Delta t) - l(x, y, t) - \Delta R_{\text{error}} \quad (5.13)$$

Neglecting the error terms for now, the radar system observes layer deformation as:

$$\frac{\partial l}{\partial t}(x, y) \approx \frac{\Delta R(x, y, \Delta t)}{\Delta t} \quad (5.14)$$

5.5.1 Measurement error sources

We consider two general classes of measurement error, each of which may impact retrievals of englacial velocities and strain rates. First, thermal noise in the radar system impacts the accuracy with which we may measure the interferometric phase. The variance of the interferometric phase noise due to thermal noise is approximately the inverse of the system signal to noise ratio [SNR, 147].

$$\Delta\phi = \frac{-f_c\sqrt{\epsilon_r}4\pi}{c}\Delta R + \phi_{\text{noise}} \quad (5.15)$$

$$\text{Var}(\phi_{\text{noise}}) \approx \frac{1}{\text{SNR}}$$

A second kind of “noise” results from unknown or unintended variations in the measurement geometry, resulting in measuring a change in range between two points not exactly equal to the intended points. This may arise from three issues: (1) off-nadir reflections due to sloped layer surfaces, (2) variations in the position of the radar between the two measurement times, and (3) constant phase offsets introduced by uncertainty in measuring the surface or bed interface locations. We consider each of these below.

5.5.2 Off-nadir reflections from non-zero layer slopes

Typical airborne radio echo sounding systems have a relatively large antenna footprint. In the along-track direction, synthetic-aperture focusing can be used to create a narrow effective along-track antenna footprint; however, the cross-track antenna footprint remains large [30]. If the layers being imaged have a non-zero cross-track slope and are largely flat, specular reflectors, as we expect them to be, the phase center of the reflection may not be at nadir. Given a wide cross-track antenna footprint and a gently sloping layer, the measured distance will generally be along the path from the antenna that makes a right angle with the layer, as shown in Fig. 5.3 and represented by the term $R_{\text{error, off-nadir}}$:

$$R_{\text{error, off-nadir}} = R(1 - \cos \alpha) \quad (5.16)$$

Neglecting any cross-track advection of this layer (a safe assumption along a flow line), the contributed error to the interferometric range estimate is:

$$\Delta R_{\text{error, off-nadir}} = \Delta R(1 - \cos \alpha) \quad (5.17)$$

A consequence of assuming that the phase center of the reflection is along the ray path perpendicular to the layer is that pointing errors (as a result of antenna calibration issues or bank angle of the aircraft) will have little impact on the distance to the phase center. As the steering angle of the antenna or array increases, the antenna’s main lobe may shift far enough that the power return

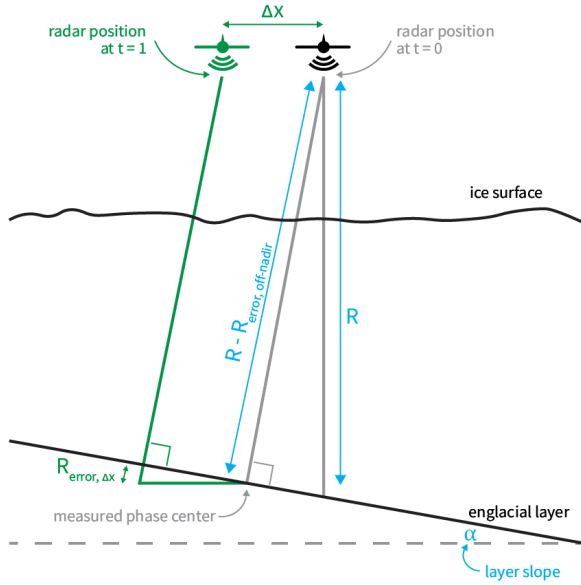


Figure 5.3: Conceptual geometry (not to scale) of a cross-track off-nadir reflection changing the measured phase to a layer with a non-zero cross-track slope (in blue) and the effects of cross-track offset of the two measurements (in green). Note that ray path changes due to the change in relative permittivity between air and ice are not shown here because we assume phases are referenced to a reflection beneath the firn.

from layers decreases significantly. Assuming largely flat layers, these issues will largely manifest as a decrease in SNR rather than an incorrectly measured phase center.

We have assumed here that the radar instrument has no way of estimating the cross-track layer slope. If the radar system is equipped with a cross-track antenna array, phased-array beamforming may be used to estimate this layer slope [63]. Alternatively, if additional lines are flown perpendicular to the main track, these measurements may be used to estimate the cross-track layer slopes, usually with effective aperture sizes much larger than are feasible with a cross-track array [22]. With known cross-track layer slopes, this error term can be fully corrected.

5.5.3 Radar instrument offset between measurements

Although efforts should be made to repeat the measured flight line as precisely as possible, some offset between the measurement locations is inevitable. There are numerous factors, including autopilot capabilities, weather, and real-time positioning accuracy, which may impact the precision of repeat flights. Generally speaking, however, reconstructing the true flight lines is an easier problem. By post-processing GNSS data with Precise Point Positioning (PPP), sub-meter accuracy can generally be obtained [55]. We will assume that, after post-processing, flight line positions are known to within a fraction of a wavelength (typical wavelengths for RES systems are around 1-5 meters) and

uncertainty in the actual recorded positions can be ignored.

Any vertical offset is compensated for by phase referencing to an englacial reflector, as previously discussed. Assuming the exact flight paths are known after the fact, measurements can be aligned and interpolated to eliminate any along-track offsets. This leaves only cross-track offsets in the radar position, a situation illustrated by the green annotations in Fig. 5.3.

For a cross-track offset Δx , the contributed error term is:

$$\Delta R_{\text{error, offset}} = \Delta x \sin \alpha \quad (5.18)$$

As with the off-nadir reflections, we note that this error term becomes zero if the layers are flat ($\alpha = 0$) and can be corrected if the cross-track layer slopes are known, for example by a cross-track radar array or by performing cross-over flights perpendicular to the main flight line.

5.5.4 Difficulty of absolutely referencing layer motion

The propagation velocity of radio waves is inversely proportional to the square root of the relative permittivity in a non-magnetic material [3]. For most purposes, it is safe to assume that the speed of light in glacier ice is a known quantity [118]. In the firn, however, unknown compaction properties complicate this [88]. As a result, it is difficult to absolutely calibrate the reflection distance of a radar system within the first 10s of meters of an ice sheet in the accumulation zone. While this uncertainty is generally small for estimating the depth of a reflector buried in 100s or 1000s of meters of ice, for a relative position measurement, it cannot be easily ignored. Given the difficulty to quantifying changes in the firn over time, this effectively introduces an unknown range offset between the measurements at the same location but spaced apart in time. As a result, we assume that the interferometric phase of two measurements beneath a firn layer spaced apart in time has some unknown constant offset.

In some cases, the ice-bed interface may provide a reliable reference point, however uncertainties exist here as well. In some cases, the apparent ice-bed interface may also change between acquisitions due to any combination of changes in subglacial water, erosion of the bed, or motion of the solid earth [149, 153]. Additionally, the ice-bed interface is generally rougher than the englacial layer interfaces. This roughness increases the impact of sensor location offset between the two measurements on interferometric phase [122]. This scenario is similar to aircraft-borne InSAR error analysis [147, see Chapter 15].

The amount of uncertainty introduced by either changes in the apparent ice-bed reflection or the firn (depending on your choice of reference) will be highly dependent on the local context. Deep interior regions with flat, frozen beds would likely have minimal uncertainty added by the bed. Areas in the ablation zone where no firn would exist are likely to be similarly low uncertainty using the radar location as the reference point.

In any case, we note that any offset introduced by unknown changes in the firm creates a constant offset in the range measurement for each reflection between two separate measurements. This is important because it means that the vertical spatial derivative of the layer motion can be observed without impact from this error source. That is to say that $\frac{\partial^2 l}{\partial t \partial z}$ can be observed even if $\frac{\partial l}{\partial t}$ is considered unreliable due to unknown firm or bed changes.

As a result, solutions to Equation 5.9 provide estimates of horizontal velocity which are unaffected by this source of uncertainty, provided that the boundary conditions are also unaffected. Retrievals of vertical velocity from horizontal velocity using Equation 5.3 depend on $\frac{\partial l}{\partial t}$ and thus are impacted by this error source. The error is canceled out if one is solving only for the vertical strain rate.

5.5.5 Phase wrapping and layer alignment

A final class of error to consider are discrete phase estimation errors, resulting either from phase wrapping of a single target (motion exceeding half a wavelength without correction) or from misalignment of radargrams (incorrectly computing the phase difference between different layers across the two snapshots in time). While avoiding these errors will be an important consideration in building software pipelines for this analysis, they are unlikely to be major obstacles. Because this work looks at tracing the phase differences across long continuous reflectors, mismatched layer pairs and phase wrapping issues should both be relatively easy to spot in processed data. Interferometric RES systems are generally relatively less impacted by phase wrapping as compared to satellite-borne InSAR as a result of their higher fractional bandwidths [57]. There is also an extensive literature on phase unwrapping in InSAR that can be readily applied to interferometric RES [157].

5.6 Applications and Examples

To demonstrate potential applications of this technique, we show several numerical examples using synthetically generated flowline models. The first set of examples highlights the potential of this technique to make in-situ estimates of ice rheology, even in grounded ice. We compare three synthetic glaciers with identical surface expressions but different values of the flow exponent in Glen's flow law [49, 48] and show that the flow law exponent can be retrieved from each. We also consider a spatially-variable rheology, where the lower parts of the ice column are made up of Eemian ice, represented as a "softer" material [104, 75].

The second example explores a rapid transition from frozen to sliding, such as what might be seen at the onset location of an ice stream [86]. Although the method does not directly estimate basal velocity, this example shows how seeing horizontal velocity in the lower layers can make a frozen to sliding transition easily apparent. We also consider the impact of temporal changes and show how estimated englacial velocity can be used to determine if the layer geometry reflects steady-state flow [103, 64]. This approach opens the possibility of quantitatively identifying parts of the ice sheet that

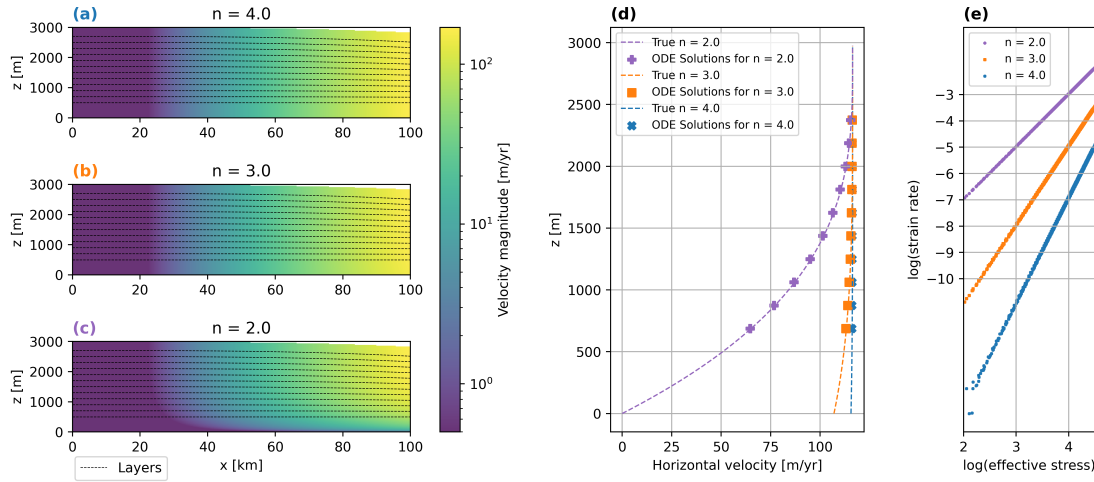


Figure 5.4: Three synthetic flowline models are created with identical surface topography and surface velocity but different rheology in the form of power law relationships with varying exponents. (a), (b), and (c) show horizontal velocity profiles for the three synthetic cases, with black dashed lines indicating the locations of simulated layers. (d) shows profiles of the horizontal velocities at $x=90$ km, with dashed lines indicating the “true” synthetic values and markers indicating ODE solutions along the layer lines. (e) shows stress and strain estimated along the ODE solution paths.

may have undergone dynamic changes in the recent past.

All of the examples are built around a two-dimensional flowline model using the shallow ice approximation. The results are based on the method of characteristics approach described in Section 5.3.2. Measurement noise is ignored for now and addressed in the following section.

5.6.1 Rheology estimation

We consider three synthetic glacier transects with identical topography and surface velocity. In each case, the exponent in Glen’s flow law is varied. The $n = 2$ case is used as a reference with prescribed zero horizontal velocity at the bed. In the other two cases, the basal velocity is set such that the surface velocity is identical to the reference case. The velocity field is assumed to be uniform in time and layers are simulated by advecting offset copies of the surface topography in the velocity field. Interferometric measurements are simulated by advecting the simulated layers by one year in the velocity field. In this experiment, no noise is added to the measurements.

In each case, the horizontal velocity is solved by numerically integrating Equation 5.9 along each layer line. Fig. 5.4 shows the results of these integrations at 90 km along the flow line. Although the surface velocities match exactly, the profile of the horizontal velocity with depth varies dramatically as a result of the different rheologies of the three cases.

Effective stress, τ_d , is calculated under the simplifying assumption that the driving stress is due only to gravitational forces and decreases linearly from the bed [$<$ see Section 8.2, $>$ cuffey_pphysics₂₀₁₀ :

$$\tau_d = \rho g(H - z) \frac{dS}{dx} \quad (5.19)$$

Where ρ is the density of ice (assumed to be constant), g is the gravitational acceleration, $H(x)$ is the ice thickness, and $S(x)$ is the surface elevation. In all examples shown here, the bed is flat at $z = 0$. Fig. 5.4(e) uses the horizontal velocities reconstructed by solving the ODE to estimate strain rate and plots effective stress versus strain rate curves, showing how the exponent used in the flow law for each experiment can be readily estimated from the reconstructions.

Recent data-driven rheology estimation techniques have produced interesting results on ice shelves [90, 117, 150], however these techniques cannot be easily extended to grounded ice because they rely on assuming that basal drag is negligible in order to infer strain rate from surface velocity alone. By providing a method to infer englacial velocity without making assumptions on basal drag or rheology, the approach we present here would allow these techniques to be extended to grounded ice and a wider class of processes, problems, and questions. This could provide evidence to resolve current discrepancies between the widely-used form of Glen's flow law with $n = 3$ and the more variable flow law forms suggested by the new data-driven rheology literature.

5.6.2 Spatially variable rheology

A further advantage of retrieving englacial velocities is being able to distinguish the dynamics of different components of the ice column. Temperature, chemical composition, grain size, crystal fabric orientation, and other factors can cause spatially-variable ice rheology [51]. Depth-dependent ice rheology, which can currently only be resolved with borehole data, may play an important role in ice sheet dynamics [129].

As one example, ice from the Last Glacial Period has been identified to be “softer” than Holocene ice [75]. This “softness” can be approximated by an enhancement factor in Glen's flow law [104].

We modify the $n = 3$ case from the prior experiment to “soften” the ice below 50% fractional ice thickness by an enhancement factor of 3. The basal velocity field is also updated to keep the surface topography and velocity identical to the prior cases. Fig. 5.5(b) shows the estimated stress versus strain rate scatter plot with points colored by depth. The depth-dependence of the ice rheology is clearly visible.

This concept could be extended to determine the dependence of the stress/strain rate relationship on temperature, ice fabric, or any other variable of interest, allowing ice sheet models to more accurately account for the dependence of rheology on other englacial conditions.

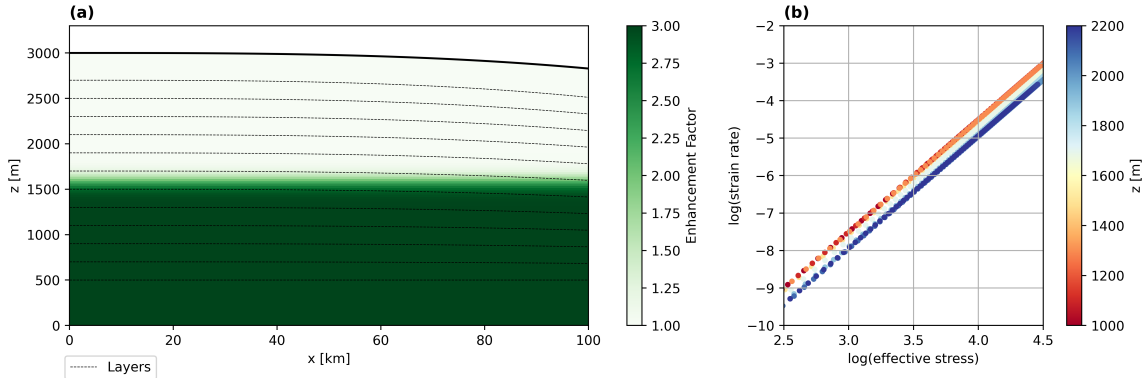


Figure 5.5: (a) A synthetic flowline model with “softer” ice (represented as an enhancement factor of 3) below 1600 meters. (b) The resulting estimated stress versus strain relationship for this depth-dependent rheology. Points in the rheology plot are shaded by depth. The depth-dependence of the enhancement factor is apparent in the higher red line representing ice from the “softer” bottom part of the glacier. Dashed black lines represent layers; the solid black line represents the surface.

5.6.3 Observing basal sliding

While the echo-free zone [38] generally prevents InRES techniques from directly measuring basal sliding, velocity measurements deep within the ice can still provide strong constraints on basal velocity. It is generally assumed that fast surface velocities, >50 m/year in Morlighem et al. [95] for example, are primarily the result of basal sliding and that slow surface velocities are primarily the result of internal deformation. Intermediate speeds, however, may be a combination of factors. Understanding what happens in transitions between slow and fast flow is critical to predicting future sea level rise [86, 34]. Basal reflectivity may be used as a proxy for basal conditions [127, 33], but the exact relationship between basal reflectivity and basal conditions contain ambiguities with traditional RES systems [14, 87].

In this example, we explore how a rapid basal transition from frozen to sliding may be observed in the lower layers of the ice column. A rapid onset of basal sliding is prescribed in the basal horizontal velocity around 80 km along the flow line. The onset of sliding produces characteristic dips in the simulated layers (more details on the layer simulation follow). Vertical velocity along the flow transect is calculated both by interpolating the results of the ODEs defined by Equation 5.9 and by applying the zero-slope approximation, as shown in Equation 5.10. The result from each approach, along with their errors from the true solution, are shown in Fig. 5.6. The sloping layers resulting from the frozen to sliding transition cause errors in the zero-slope approximation solution that can only be corrected with knowledge of the horizontal velocity profile.

Although the simulated layers do not extend to the bed, Fig. 5.7 shows how the lowest layer more clearly shows the true basal velocity profile. How closely the lowest layer matches the basal velocity is primarily determined by how close to the bed the last observable layer is and the local

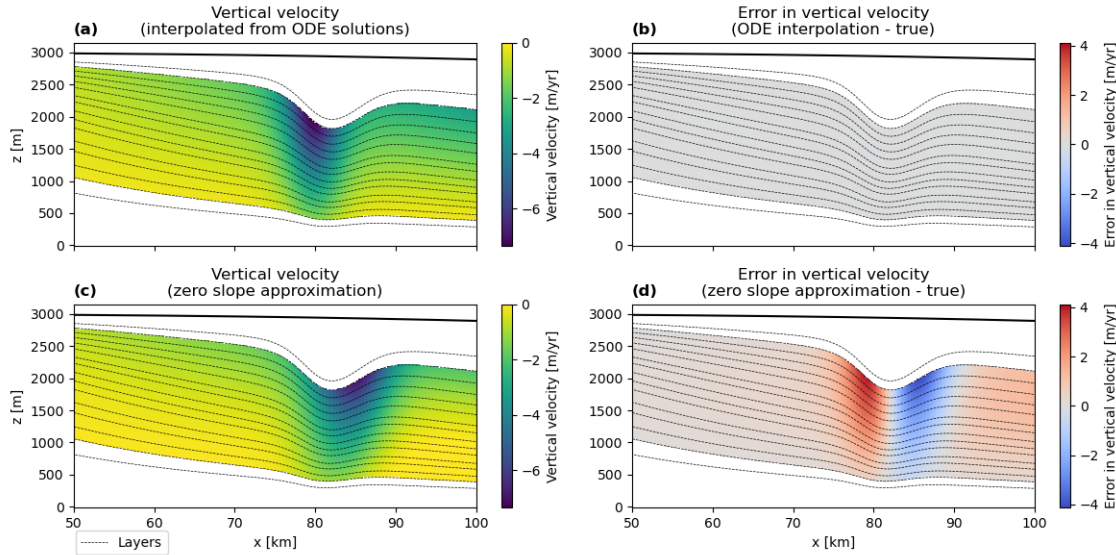


Figure 5.6: Results of solving for vertical velocity in a synthetic frozen-to-sliding transition case. The top plots (a-b) show the results of interpolating the ODEs along the characteristic curves, which correctly reconstructs the nearly vertical column of increased vertical velocity. The bottom plots (c-d), showing the results of the zero-slope approximation, capture the general trend but distort and shift the vertical velocity profile. The maximum layer dip in this example is less than 7 degrees. Dashed black lines represent layers; the solid black line represents the surface.

rheology. The relationship between surface velocity and basal velocity is complex and not well understood [116]. Englacial velocity measurements would provide a new constraint to improve our understanding of basal sliding, which is critical to understanding ice streams [86] and predicting future ice mass loss [34].

5.6.4 Identifying englacial velocity in transition

The layers in the above example were simulated by advecting the surface profile by an increasing number of years within the velocity field *with no basal sliding* to form each layer. This layer geometry was then advected within the velocity field *with* basal sliding for an additional 100 years. As a result, the simulated layers represent a geometry in transition from one steady-state flow regime to another. After reconstructing the englacial velocity profile, the geometry of layers advected only through the current flow profile can be determined. By comparing the slopes of the observed layers to the expected slopes of layers in a steady state flow with the current englacial velocity profile, we can estimate if the current flow field is in steady state, relative to the ages of the observed layers. Fig. 5.8 shows how this layer misalignment analysis reveals the parts of the velocity profile that are not in steady state. This approach may be able to shed light on the flow history of glaciers, especially

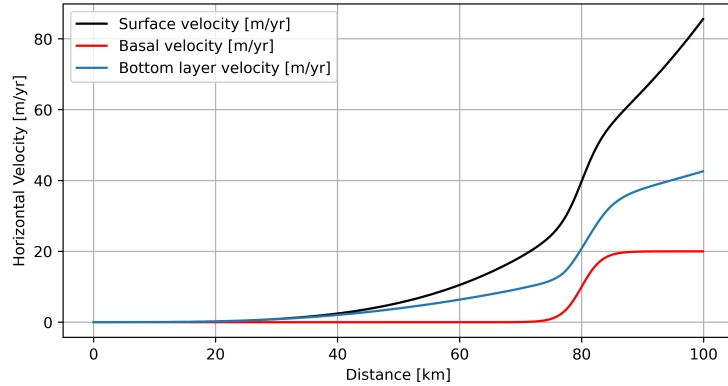


Figure 5.7: Horizontal velocity profiles at the surface, the bed, and the lowest available layer are shown for the same simulated setup as Fig. 5.6. Although basal velocity cannot be directly observed with InRES, the horizontal velocity profiles of layers deep within the ice provide better indicators of basal velocity than surface velocity alone.

around areas of rapid transition in velocity, and provides a constraint on ice flow that may pre-date the satellite record in some cases.

5.6.5 Measurement noise and cross-track error simulations

Section 5.5.1 outlines a model for how measurement noise and uncompensated geometry errors can impact reconstructions of englacial velocity. Starting from the same setup as in Section 5.6.3, we introduce Gaussian noise in the layer measurements, following Equation 5.15, and simulate the effects of uncompensated cross-track layer slopes.

We note that care must be taken in specifying the SNR of a radar instrument because the SNR generally increases through a series of post-processing steps, which may include coherent summation, incoherent summation, and focusing. These tasks are commonly split between onboard processing and post-processing, so care must be taken in translating these results between radar systems. For these simulations, we specify an SNR at 10 Hz pulse repetition interval (representative of the effective pulse repetition interval after stacking). We assume a center frequency of 60 MHz.

Due to the multiple terms in Equation 5.9, which must be approximated by finite differences, directly solving the ODE with noisy inputs is often unstable (see Section 5.9) due to the physically-unrealistic large derivatives of the layer geometry function. To mitigate this, high-frequency noise is reduced by taking a moving average of the layer depth over a 100-meter window.

This filtering process is applied independently on each layer at each time. In reality, each layer is not independent of the others surrounding it. These statistical relationships could conceivably be used in the filtering process, but we neglect this potential optimization for now. For real-world

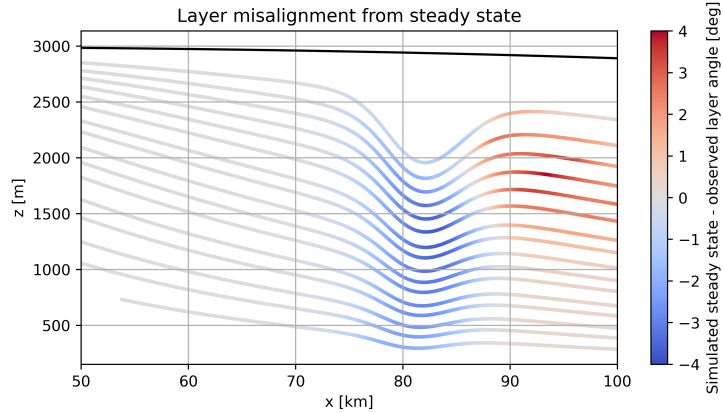


Figure 5.8: Observed layer slopes are compared against layers simulated by advecting within the current velocity profile. The mismatch between these slopes shows areas where the observed layers do not align with the current flow field, suggesting recent changes in the englacial velocity field. Dashed black lines represent layers; the solid black line represents the surface.

applications, layer-optimized focusing [22] may be a practical approach to successfully extracting high-SNR radargrams while directly estimating layer slopes.

The results of solving for horizontal and vertical velocity using the method of characteristics approach with a range of measurement SNRs and uncompensated cross-track slopes are shown in Fig. 5.9. Even under the low SNR and high cross-track slope scenario, the basic patterns of englacial velocity remain clearly visible. Note, however, that this example does not consider any impacts of spatial offsets between repeat measurements.

For horizontal velocity solutions, the error terms accumulate along the ODE solution lines, leading to a striped pattern. For vertical velocity, however, error terms are introduced directly through Equation 5.3. Note that we do not simulate the effects of unknown changes in the firn (Section 5.5.4), which would further add to vertical velocity reconstruction error (but not horizontal velocity), unless a suitable correction can be applied.

5.7 Discussion

We have shown that three-dimensional horizontal and vertical englacial velocity profiles may be obtained using interferometric processing of airborne RES data. Successfully achieving this with real-world data collection requires careful planning and imposes some requirements on both the radar system and its platform.

Most importantly, englacial velocity reconstruction by the proposed method is only practical if radar data is collected following surface flow lines, where continuously traceable layers are visible and can be traced to a boundary condition where horizontal velocity can be relatively accurately

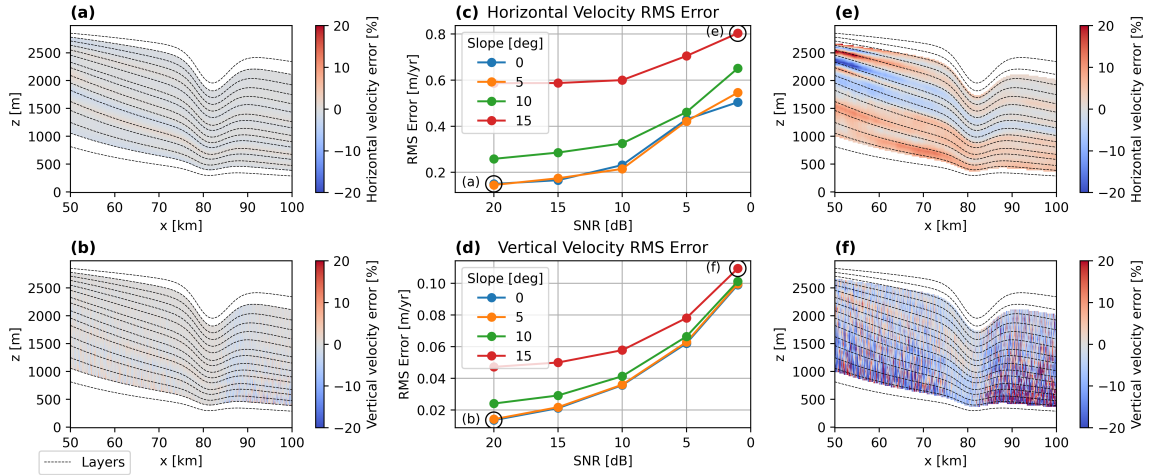


Figure 5.9: (a, b) Example horizontal (a) and vertical (b) englacial velocity reconstruction error at high SNR (25 dB) with zero cross-track slope. (c, d) Comparison of root-mean-square (RMS) error in horizontal (c) and vertical (d) velocity over a range of SNR and cross-track slopes. RMS error is evaluated over the same domain shown in the example figures (a, b, e, f). (e, f) Example horizontal (e) and vertical (f) englacial velocity reconstruction error at very low SNR (1 dB) with 15 degree cross-track slope. Despite the extreme geometry and high noise levels, the error terms remain relatively small.

estimated throughout the depth of the ice. Practically, this means an ice divide or, at least, an area of very slow flow close to a divide. Up-to-date surface flow lines must also be known to reasonable precision.

The requirement for continuously traceable layers is likely the strongest constraint on both SNR and bandwidth for radar systems. While bandwidth does not directly enter into SNR as modelled here, the assumption behind Equation 5.15 is that a single reflection is dominating the return from the relevant range bin, thus the radar bandwidth must be sufficient to fully separate all strong englacial reflectors and the SNR must be sufficient to resolve layers as deep in the ice column as possible.

Knowing the cross-track layer slopes is desirable, though perhaps not a strong requirement depending on the survey objectives. This can be achieved either by flying perpendicular crossing flights or by using a cross-track array [63]. In some cases, this might also be achievable by examining previously-collected layer data in the area.

The cross-track layer slopes largely determine the importance of precise re-flights. If the cross-track layer slopes are near zero, there is more tolerance to repeat measurements with some offset. If the cross-track slopes are high, however, either very precise repeat flights are needed or the cross-track slopes need to be mapped very well. In any case, platforms should be equipped to produce sub-wavelength positioning estimates following post-processing, a requirement that should

be relatively easy to satisfy with modern GNSS receivers.

Many of these requirements can only be accurately quantified in local context of the layer arrangement, which requires compiling existing radar data or using a pre-made dataset, such as the existing radiostratigraphy of Greenland [82] or the results of the currently-ongoing AntArchitecture effort [11].

A final survey planning consideration should be the expected stability of the ODE solution, as discussed in Section 5.9. The stability criterion for the ODE may be of limited use in many real-world situations where the surface velocity switches between converging and diverging multiple times, in which case the formal criterion cannot offer guarantees either way. Intuitively, however, the stability analysis process can guide away from attempting to apply this technique in areas of strongly converging flow, where the ODEs are unlikely to be stable.

The techniques described in this work offer a pathway to mapping three-dimensional englacial velocity at ice sheet scale. While a theoretical pathway has been laid out, real-world validations are needed to clarify and refine the limits of where and how these approaches may be applied. It is clear that creating an ice sheet-scale velocity map would represent a massive surveying effort. An ice-sheet scale survey pattern would be needed, with repeat measurements needed across all lines at varying intervals, depending on the flow speed of the ice. Effectively, this would transform continent-scale RES surveying from a one-time map making effort to an annual time series product.

The scientific opportunities from building such a time series are extensive. In much the same way that time series surface velocity maps have improved estimates of basal topography [95], revealed subsurface hydrology dynamics [135], improved our understanding of basal sliding [71], provided a means of quantitatively estimating rheology on ice shelves [90], and more, unlocking three-dimensional englacial velocity would have wide-ranging implications for glaciology. This work connects InRES measurements directly to englacial velocity, a field that is already represented but under-constrained in ice sheet models. This provides a direct pathway to incorporating new radar-derived constraints beyond basal topography into numerical models. In addition to direct assimilation into models, englacial velocity maps would allow for quantifying ice rheology across entire ice sheets, not just on ice shelves, and would give a much more direct picture of where basal sliding occurs and how it begins. Englacial velocity maps would also allow for better estimates of mass flux, which would improve mass conservation interpolation-based bed mapping, and a better understanding of how dynamics such as seasonal hydrology cycles impact glacier flow.

Englacial layer structure (without interferometry) has long been used as a record of flow history, but the fact that layers encode the combined effects of hundreds or thousands of years of flow history limits their use for understanding present-day velocity fields. When combined with interferometry to derive current englacial velocity, however, there is an opportunity to compare layer structure with englacial velocity maps to determine if sections of an ice sheet or glacier are in steady state or in a period of transition.

Ice sheet scale englacial velocity maps represent an interesting new potential data source in that they rely on proven and well-understood sensing technology. The basics of radio echo sounding and interferometric radar processing are both extremely well studied. While some instrument advancements may be needed, the primary obstacle to developing three-dimensional velocity maps is logistical, due to the high cost and logistical complications with flying the crewed aircraft used for RES surveys in Antarctica and Greenland. Uncrewed aerial vehicles (UAVs) may provide part of the solution. In addition to reducing the costs associated with airborne surveying, UAVs may simplify the process of collecting repeat lines. If the logistical obstacles can be overcome, englacial velocity maps could rapidly improve the fidelity of ice sheet models and unlock better predictions for the future of Antarctica and Greenland.

5.8 Conclusions

In this paper, we have developed a mathematic framework connecting interferometric radio echo sounding (InRES) observations to subsurface velocity, with minimal assumptions on the internal dynamics of the ice. This approach allows for InRES measurements to be used for englacial velocity estimation across a wide range of possible study sites. We have also illustrated how this general framework compares to the zero slope approximation, and provided some intuition on where the zero slope approximation is or is not applicable.

We have also provided a solution approach that limits the InRES data that must be collected to repeat observations of a single flow line, provided that the flow line is extended to a suitable boundary where the horizontal velocity is known throughout the ice column, most likely an ice divide. Basic error analysis has been provided, although there is much work to be done in extending this to real-world datasets and more complicated processing techniques.

Finally, we have offered some guiding thoughts on the platforms and radar instruments that will be best suited to collecting the repeat measurements needed for InRES processing and englacial velocity estimation.

5.9 Stability of horizontal velocity ODE

The ODE in Equation 5.8 can be written in the standard form:

$$\frac{\partial s}{\partial \tau} = -a(\tau) - sb(\tau) \quad (5.20)$$

When $b(\tau) > 0$ for all τ , the ODE is stable, meaning that the solutions for two different initial conditions will vary by no more than the difference in the initial values [67]. Equation 5.9 is stable if the following criterion holds true for all values of τ in the solution domain:

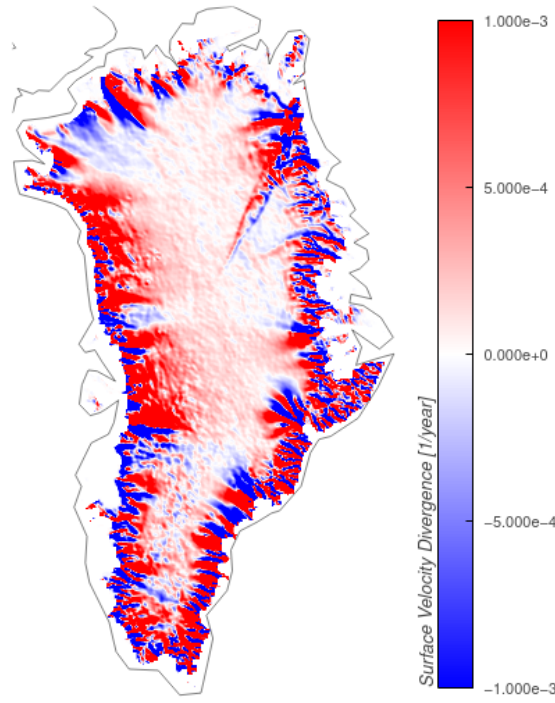


Figure 5.10: Map of the surface velocity divergence in Greenland based on Greenland surface velocity data [45]. Areas in red (positive) are likely to have locally stable behavior of Equation 5.9.

$$b(\tau) = \underbrace{u_s \frac{\partial^2 l}{\partial x \partial z} + v_s \frac{\partial^2 l}{\partial y \partial z}}_{\text{layer geometry}} + \underbrace{\frac{\partial v_s}{\partial y} + \frac{\partial u_s}{\partial x}}_{\text{surface velocity}} > 0 \quad (5.21)$$

If $b(\tau) < 0$ over the entire domain, then Equation 5.9 is unstable. In cases where $b(\tau)$ changes sign, practically useful bounds are not known to the authors.

This stability condition is a function of surface velocity and layer geometry. Existing radar data, either directly from radargrams or as compiled in radiostratigraphy analyses [82], can be used to estimate the layer geometry component. Surface velocity estimates are widely available from satellite observations.

Investigation of the stability of Equation 5.9 in specific regions based on all available data is advisable if interferometric radar surveys are being planned.

To develop some intuition about the stability criterion, we separately consider the terms depending on the layer geometry from the terms depending only on the surface velocity, as labeled in Equation 5.21.

We use a radiostratigraphic compilation across Greenland [82] combined with Greenland surface velocity data from autoRIFT [45] and bed topography from BedMachine [95]. We apply 5 kilometer

standard deviation Gaussian smoothing to the isochrone geometry and surface velocities to minimize measurement artifacts in the data. Within the area where layer geometry is available, we find that the magnitude of the surface velocity divergence term of Equation 5.21 is greater than the magnitude of the terms depending on the layer geometry about 85% of the time and more than twice the layer geometry terms about 71% of the time. This suggests that, in practice, the layer geometry terms are generally small in comparison to the surface velocity divergence. Thus, for the purpose of gaining intuition about where this technique is most likely to be numerically stable, we may approximate the stability criterion as $\frac{\partial v_s}{\partial y} + \frac{\partial u_s}{\partial x} > 0$, or simply that the surface velocity field is diverging. The divergence of the surface velocity field for Greenland is shown in Fig. 5.10. It is positive throughout most of the interior but varies significantly in faster flowing areas.

5.10 SIA model to evaluate zero layer slope approximation

In order to investigate where the zero layer slope approximation is suitable, we propose considering a shallow ice approximation [SIA, 68] model with a flow exponent of $n = 3$ and the basal horizontal velocity fixed at zero. Greenland surface topography from Morlighem [96] and surface velocity data generated from Gardner et al. [45] are used for this model. The SIA model provides a simulated englacial velocity field, from which we extract the vertical gradients of horizontal velocity. While not strictly a limit, we treat this as an upper bound on plausible vertical gradients of horizontal velocity.

Because estimating the $u_f \sec^2(\alpha) \frac{\partial \alpha}{\partial z}$ term is challenging on an ice sheet scale, we focus on the $\frac{\partial u_f}{\partial z} \tan \alpha$ error term. Using the described SIA model, we find the maximum layer slope α that achieves a given percentage error in vertical strain rate estimation under the zero-slope approximation.

Fig. 5.11 shows the results of evaluating this model at 50% fractional ice thickness for the maximum layer slope that could exist while bounding the error in vertical strain rate to 10%.

We note that the 10% error figure and the 50% ice thickness are both chosen arbitrarily. We also note that this rough model is designed to approximate a case where nothing is known about the rheology or basal conditions. When more is known, a different part of the ice column is being studied, or different error limits apply, this analysis will look different. Our purpose here is to provide an example of our proposed methodology to evaluate if this approximation is suited to a particular task. The evaluation of the suitability of this approximation can only be performed in the full context of a specific study site and a scientific objective.

While the exact parameters may vary, the map in Fig. 5.11 produces the expected pattern. Slow-flowing areas near ice divides permit much steeper layer slopes for a given percent error in vertical strain rate.

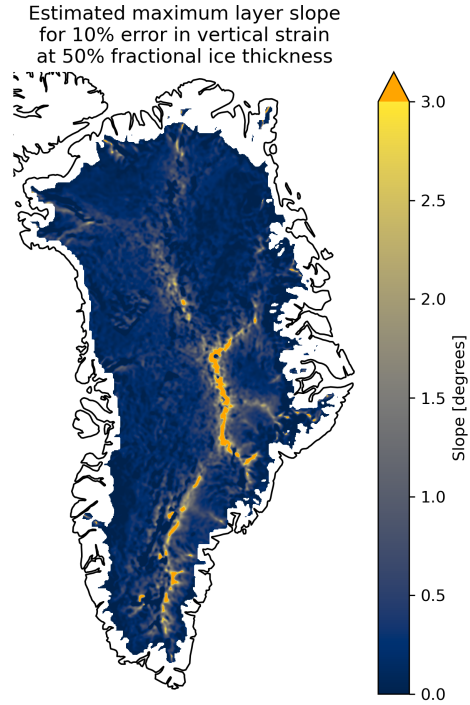


Figure 5.11: Maximum layer slope for 10% error in vertical strain rate when using the zero layer slope approximation, based on an SIA model with $n=3$ evaluated at 50% fractional ice thickness. Areas in yellow or orange would permit a steeper layer slope, thus making them more feasible as locations to neglect layer slope and apply the zero-slope approximation. Areas in blue likely require additional assumptions on the englacial velocity structure.

Open Research Section

Greenland surface topography, traced radiostratigraphy, and surface velocity data products are used for the stability analysis in Section 5.9. Surface topography data is available from the NSIDC at <https://doi.org/10.5067/GMEVBWFLWA7X> [96]. The traced radiostratigraphy data is also available from the NSIDC at <https://doi.org/10.5067/UGI2BGTC4QJA> [83]. Greenland surface velocity data was generated using auto-RIFT [45] and is provided by the NASA MEaSUREs ITS_LIVE project (<https://its-live.jpl.nasa.gov/>) at https://its-live-data.s3.amazonaws.com/velocity_mosaic/v1/static/GRE_G0120_0000.nc. This dataset is alternatively available from the NSIDC at <https://doi.org/10.5067/6ii6vw8llwj7> [46].

All code to reproduce the figures and simulations in this paper are available on GitHub at https://github.com/thomasteisberg/englacial_velocity and archived on Zenodo at <https://zenodo.org/record/4520277>.

//doi.org/zenodo.15191737 [138].

Acknowledgements

The authors would like to thank NASA and the TomKat Center for Sustainable Energy for support in developing this work. We would also like to thank Roland Warner for helpful email conversations in response to early versions of this work. The authors would like to thank the editor, Dr. Japp Nienhuis, Dr. John Paden, and one anonymous reviewer for their helpful feedback and suggestions.

T. O. Teisberg was supported by a NASA FINESST Grant (80NSSC23K0271), the TomKat Center for Sustainable Energy, and Stanford Data Science. Additional support was provided by the Heising-Simons Foundation and the Stanford Institute for Human-Centered Artificial Intelligence.

Chapter 6

Conclusions

6.1 Summary of Research

The contributions in this dissertation are aimed at unlocking new ways of collecting and interpreting sub-surface geophysical data about Earth’s ice sheets, reducing the costs of large-scale sub-surface data collection efforts and helping to accelerate an era of sub-surface data richness for Earth’s ice sheets. I have presented developments in IPR instrumentation, automated platforms to carry these instruments, and the interpretation of IPR radar data. The key contributions of myself and my co-authors are as follows:

- Development of an open-source framework for building highly configurable ice-penetrating radar instruments
- An approach for data collection and post-processing that enables divergent purpose-built radar instruments to be processed with a common set of code
- An open-source, inexpensive IPR payload design tightly integrated with a fixed-wing UAV that has been successfully demonstrated in real-world polar field conditions
- A rigorous analysis of how interferometric radar sounder data may be used to infer englacial velocity structure, including potential sources of error and the associated implications for radar and platform design

6.2 Future Directions

The sections below briefly review relevant next steps for each of the three chapters.

6.2.1 Software-defined radar

With both Anna and myself at least temporarily moving on from building radar systems, it is important that ORCA finds a new set of users. Others in the lab and externally are beginning to leverage ORCA for future projects, but there is a lot of work to do in building a sustainable community of users.

Critical to the building of a more diverse community of users will be improving on automated tests to ensure that new development directions do not conflict or cause regressions for other users.

There is also significant work to be done in post-processing features. Currently only very basic post-processing is offered, however it should be straight-forward to build features such as focusing, interferometry, and noise suppression into the existing architecture. This will also raise questions about integration with radar data from non-ORCA instruments. The ORCA data architecture solves many problems with large IPR datasets that could benefit other radar systems, however it is not unique in proposing a solution. Some thought will need to be put into how the ORCA post-processing code should or should not integrate with other radar systems.

6.2.2 UAV-borne ice-penetrating radar

Peregrine exists as a ready-to-use platform. There are certainly improvements that could be made both to the aircraft design and to the radar instrument, however these are likely to be somewhat specific to the desired mission.

As it stands, Peregrine's radar is extremely limited by the mass budget not supporting a meaningfully large power amplifier. There are, however, slightly larger aircraft that can support significantly larger payloads. A 2.5 kg version of the payload has already been ground-tested near Summit Station and dramatically improves on the current radar capabilities. This version of the payload is under active development for a 4-meter wingspan UAS in collaboration with Jamin Greenbaum at the Scripps Institute of Oceanography.

Two significant technical challenges remain with that radar system: antenna integration with the aircraft and power management. On the power management side, the available power from the aircraft is limited and must be shared with the avionics in a way that prioritizes the avionics over the scientific instrumentation. Careful management of the power amplifier and design of the power supplies can maximize the transmitted energy per watt drawn from the aircraft generator. On the antenna integration side, consideration should be given to aerodynamic fairings to protect the antennas and reduce both drag and any potential flutter.

6.2.3 Interferometric estimation of englacial velocity

Although work has been done on radar sounder interferometry for more than a decade, the existing literature has focused on narrow cases where simplifying assumptions could be made due to the

measurement geometry and/or known properties of the ice. For most of that time, collecting airborne measurements has been practically challenging due to the lack of high-quality autopilots on the aircraft collecting airborne IPR data. As UAV-borne radar becomes an operational reality, significant work is needed to fully understand the potential of airborne radar sounder interferometry. The potential to create a three-dimensional map of englacial velocity is extremely exciting and could transform how we currently model ice sheets, eliminating the need for untestable assumptions about ice rheology and sliding. At the same time, however, the potential noise sources are numerous and the signal being measured is very small. The work presented here should hopefully serve as a useful foundation, but questions about how well we can overcome errors in these measurements and arrive at useful englacial velocity measurements may only be answered once real data is collected. Some repeat-pass radar data does exist, but very little of it is flow-aligned. Perhaps the most promising data yet was collected this past season.

If englacial velocity can be retrieved from IPR interferometry, this should change the way we think about IPR data collection. For decades, IPR data has been primarily viewed as a tool to make maps of the basal interface, which, over grounded areas, mostly changes at rates that are not detectable to conventional IPR systems on human timescales. As we have learned from satellite-derived surface velocity, however, englacial velocity likely varies on much shorter timescales. The successful development of an englacial velocity measurement capability would be a core part of a strong case that IPR data needs to be viewed as a time-series measurement, not a one-off mapping effort.

References

- [1] *About USRP Bandwidths and Sampling Rates*. 2016. URL: https://kb.ettus.com/About%5C_USRP%5C_Bandwidths%5C_and%5C_Sampling%5C_Rates.
- [2] Christopher T. Allen, Shadab N. Mozaffar, and Torry L. Akins. “Suppressing Coherent Noise in Radar Applications With Long Dwell Times”. In: *IEEE Geoscience and Remote Sensing Letters* 2.3 (2005), pp. 284–286. ISSN: 1545-598X. DOI: 10.1109/lgrs.2005.847931.
- [3] P. Allison et al. “Measurement of the real dielectric permittivity ϵ of glacial ice”. en. In: *Astroparticle Physics* 108 (Mar. 2019), pp. 63–73. ISSN: 09276505. DOI: 10.1016/j.astropartphys.2019.01.004. URL: <https://linkinghub.elsevier.com/retrieve/pii/S0927650518301154>.
- [4] M.J. Andrews et al. “Properties of the 500-2000-MHz RFI environment observed in high-latitude airborne radiometer measurements”. In: *IEEE Trans. Geosci. Remote Sens.* 60 (2021), pp. 1–11. ISSN: 0196-2892. DOI: 10.1109/tgrs.2021.3090945.
- [5] Gordon Ariho. “Multipass SAR Processing for Ice Sheet Vertical Velocity and Tomography Measurements”. en. PhD thesis. University of Kansas, 2023. URL: <https://hdl.handle.net/1808/35033>.
- [6] Gordon Ariho et al. “Joint Estimation of Ice Sheet Vertical Velocity and Englacial Layer Geometry from Multipass Synthetic Aperture Radar Data”. en. In: *2022 IEEE International Symposium on Phased Array Systems & Technology (PAST)*. Waltham, MA, USA: IEEE, Oct. 2022, pp. 01–05. ISBN: 978-1-66544-166-7. DOI: 10.1109/PAST49659.2022.9974985. URL: <https://ieeexplore.ieee.org/document/9974985/>.
- [7] Emily Arnold et al. “HF/VHF Radar Sounding of Ice from Manned and Unmanned Airborne Platforms”. en. In: *Geosciences* 8.5 (May 2018), p. 182. ISSN: 2076-3263. DOI: 10.3390/geosciences8050182. URL: <http://www.mdpi.com/2076-3263/8/5/182>.
- [8] Curtis Barrett. “Fractional/Integer-N PLL Basics”. en. In: (1999). TI Publication SWRA029.
- [9] Robin E. Bell and Helene Seroussi. “History, mass loss, structure, and dynamic behavior of the Antarctic Ice Sheet”. en. In: *Science* 367.6484 (Mar. 2020), pp. 1321–1325. ISSN: 0036-8075, 1095-9203. DOI: 10.1126/science.aaz5489. URL: <https://www.science.org/doi/10.1126/science.aaz5489>.

- [10] N.L. Bienert et al. “Post-Processing Synchronized Bistatic Radar for Long Offset Glacier Sounding”. In: *IEEE Trans. Geosci. Remote Sens.* 60 (2022), pp. 1–17. ISSN: 0196-2892. DOI: 10.1109/tgrs.2022.3147172.
- [11] Robert G. Bingham et al. *Review Article: Antarctica’s internal architecture: Towards a radiostratigraphically-informed age-depth model of the Antarctic ice sheets*. Oct. 2024. DOI: 10.5194/egusphere-2024-2593. URL: <https://egusphere.copernicus.org/preprints/2024/egusphere-2024-2593/>.
- [12] P.V. Brennan et al. “Phase-sensitive FMCW radar system for high-precision Antarctic ice shelf profile monitoring”. In: *IET Radar, Sonar & Navigation* 8.7 (2014), pp. 776–786. ISSN: 1751-8784. DOI: 10.1049/iet-rsn.2013.0053.
- [13] Paul V. Brennan et al. “Phase-sensitive FMCW radar system for high-precision Antarctic ice shelf profile monitoring”. en. In: *IET Radar, Sonar & Navigation* 8.7 (Aug. 2014), pp. 776–786. ISSN: 1751-8792, 1751-8792. DOI: 10.1049/iet-rsn.2013.0053. URL: <https://onlinelibrary.wiley.com/doi/10.1049/iet-rsn.2013.0053>.
- [14] Anna L. Broome and Dustin M. Schroeder. “A Radiometrically Precise Multi-Frequency Ice-Penetrating Radar Architecture”. en. In: *IEEE Transactions on Geoscience and Remote Sensing* 60 (2022), pp. 1–15. ISSN: 0196-2892, 1558-0644. DOI: 10.1109/TGRS.2021.3099801. URL: <https://ieeexplore.ieee.org/document/9506987/>.
- [15] Anna L. Broome, Dustin M. Schroeder, and Joel T. Johnson. “First Results from Mapperr: The Multi-Frequency Active Passive Polar Exploration Radar-Radiometer”. In: *IGARSS 2023 - 2023 IEEE International Geoscience and Remote Sensing Symposium* 00 (2023), pp. 36–39. DOI: 10.1109/igarss52108.2023.10282237.
- [16] Anna L. Broome, Dustin M. Schroeder, and Thomas O. Teisberg. “A Framework for Considering Receiver Saturation Trade-Offs in Ice-Penetrating Radars”. en. In: *IGARSS 2024 - 2024 IEEE International Geoscience and Remote Sensing Symposium*. Athens, Greece: IEEE, July 2024, pp. 11450–11453. ISBN: 9798350360325. DOI: 10.1109/IGARSS53475.2024.10641680. URL: <https://ieeexplore.ieee.org/document/10641680/>.
- [17] Lorenzo Bruzzone et al. “STRATUS: A new mission concept for monitoring the subsurface of polar and arid regions”. en. In: *2021 IEEE International Geoscience and Remote Sensing Symposium IGARSS*. Brussels, Belgium: IEEE, July 2021, pp. 661–664. ISBN: 978-1-66540-369-6. DOI: 10.1109/IGARSS47720.2021.9553877. URL: <https://ieeexplore.ieee.org/document/9553877/>.
- [18] S. Campbell et al. “Brine, englacial structure and basal properties near the terminus of McMurdo Ice Shelf, Antarctica”. In: *Annals of Glaciology* 58.74 (2017), pp. 1–11. ISSN: 0260-3055. DOI: 10.1017/aog.2017.26.

- [19] Leonardo Carrer et al. “Distributed Radar Sounder: A Novel Concept for Subsurface Investigations Using Sensors in Formation Flight”. en. In: *IEEE Transactions on Geoscience and Remote Sensing* 57.12 (Dec. 2019), pp. 9791–9809. ISSN: 0196-2892, 1558-0644. DOI: 10.1109/TGRS.2019.2929422. URL: <https://ieeexplore.ieee.org/document/8804366/>.
- [20] Elizabeth Case and Jonathan Kingslake. “Phase-sensitive radar as a tool for measuring firn compaction”. en. In: *Journal of Glaciology* 68.267 (Feb. 2022), pp. 139–152. ISSN: 0022-1430, 1727-5652. DOI: 10.1017/jog.2021.83. URL: https://www.cambridge.org/core/product/identifier/S0022143021000836/type/journal_article.
- [21] Davide Castelletti et al. “Layer optimized SAR processing and slope estimation in radar sounder data”. In: *Journal of Glaciology* 65.254 (2019), pp. 983–988. ISSN: 0022-1430. DOI: 10.1017/jog.2019.72.
- [22] Davide Castelletti et al. “Layer optimized SAR processing and slope estimation in radar sounder data”. en. In: *Journal of Glaciology* 65.254 (Dec. 2019), pp. 983–988. ISSN: 0022-1430, 1727-5652. DOI: 10.1017/jog.2019.72. URL: https://www.cambridge.org/core/product/identifier/S0022143019000728/type/journal_article.
- [23] Davide Castelletti et al. “Permanent Scatterers in Repeat-Pass Airborne VHF Radar Sounder for Layer-Velocity Estimation”. en. In: *IEEE Geoscience and Remote Sensing Letters* (2020), pp. 1–5. ISSN: 1545-598X, 1558-0571. DOI: 10.1109/LGRS.2020.3007514. URL: <https://ieeexplore.ieee.org/document/9143148/>.
- [24] Blake A. Castleman et al. “Derivation of bedrock topography measurement requirements for the reduction of uncertainty in ice-sheet model projections of Thwaites Glacier”. In: *The Cryosphere* 16.3 (Mar. 2022). Saved from BrowZine: <http://thirdiron.com/download>, pp. 761–778. ISSN: 1994-0416. DOI: 10.5194/tc-16-761-2022. URL: <https://browzine.com/articles/519715930>.
- [25] Marie G P Cavitte et al. “From ice core to ground-penetrating radar: representativeness of SMB at three ice rises along the Princess Ragnhild Coast, East Antarctica”. In: *Journal of Glaciology* (2022), pp. 1–13. ISSN: 0022-1430. DOI: 10.1017/jog.2022.39.
- [26] K. Christianson et al. “Basal conditions at the grounding zone of Whillans Ice Stream, West Antarctica, from ice-penetrating radar”. In: *J. Geophys. Research: Earth Surface* 121.11 (2016), pp. 1954–1983. ISSN: 2169-9011. DOI: 10.1002/2015jf003806.
- [27] H. F. J. Corr et al. “Precise measurement of changes in ice-shelf thickness by phase-sensitive radar to determine basal melt rates”. en. In: *Geophysical Research Letters* 29.8 (Apr. 2002). ISSN: 0949-8276, 1944-8007. DOI: 10.1029/2001GL014618. URL: <https://agupubs.onlinelibrary.wiley.com/doi/10.1029/2001GL014618>.
- [28] CReSIS Radar Depth Sounder Readme. Tech. rep. University of Kansas. URL: https://data.cresis.ku.edu/data/rds/rds_readme.pdf.

- [29] R. Culberg and D.M. Schroeder. “Firn Clutter Constraints on the Design and Performance of Orbital Radar Ice Sounders”. In: *IEEE Trans. Geosci. Remote Sens.* 58.9 (2020), pp. 1–18. ISSN: 0196-2892. DOI: [10.1109/tgrs.2020.2976666](https://doi.org/10.1109/tgrs.2020.2976666).
- [30] Riley Culberg and Dustin M. Schroeder. “Firn Clutter Constraints on the Design and Performance of Orbital Radar Ice Sounders”. en. In: *IEEE Transactions on Geoscience and Remote Sensing* 58.9 (Sept. 2020), pp. 6344–6361. ISSN: 0196-2892, 1558-0644. DOI: [10.1109/TGRS.2020.2976666](https://doi.org/10.1109/TGRS.2020.2976666). URL: <https://ieeexplore.ieee.org/document/9031695/>.
- [31] Riley Culberg, Dustin M. Schroeder, and Winnie Chu. “Extreme melt season ice layers reduce firn permeability across Greenland”. en. In: *Nature Communications* 12.1 (Dec. 2021), p. 2336. ISSN: 2041-1723. DOI: [10.1038/s41467-021-22656-5](https://doi.org/10.1038/s41467-021-22656-5). URL: <http://www.nature.com/articles/s41467-021-22656-5>.
- [32] John C Curlander and Robert N McDonough. *Synthetic aperture radar systems and signal processing*. Vol. 11. Wiley, New York, 1991.
- [33] Eliza J. Dawson et al. “Heterogeneous Basal Thermal Conditions Underpinning the Adélie-George V Coast, East Antarctica”. en. In: *Geophysical Research Letters* 51.2 (Jan. 2024), e2023GL105450. ISSN: 0094-8276, 1944-8007. DOI: [10.1029/2023GL105450](https://doi.org/10.1029/2023GL105450). URL: <https://agupubs.onlinelibrary.wiley.com/doi/10.1029/2023GL105450>.
- [34] Eliza J. Dawson et al. “Ice mass loss sensitivity to the Antarctic ice sheet basal thermal state”. en. In: *Nature Communications* 13.1 (Sept. 2022), p. 4957. ISSN: 2041-1723. DOI: [10.1038/s41467-022-32632-2](https://doi.org/10.1038/s41467-022-32632-2). URL: <https://www.nature.com/articles/s41467-022-32632-2>.
- [35] Annick Dewald and R J. Hansman. “A Multidisciplinary Analysis of a Stratospheric Airborne Climate Observatory System for Key Climate Risk Areas”. en. In: *AIAA SCITECH 2023 Forum*. National Harbor, MD & Online: American Institute of Aeronautics and Astronautics, Jan. 2023. ISBN: 978-1-62410-699-6. DOI: [10.2514/6.2023-2603](https://doi.org/10.2514/6.2023-2603). URL: <https://arc.aiaa.org/doi/10.2514/6.2023-2603>.
- [36] Alexey Dobrovolskiy and Kristaps Brass. “GPR on a drone — practical experience gained in the past 2 years”. In: *18th International Conference on Ground Penetrating Radar, Golden, Colorado, 14–19 June 2020*. 18th International Conference on Ground Penetrating Radar, Golden, Colorado, 14–19 June 2020. Golden, Colorado, USA: Society of Exploration Geophysicists, Nov. 11, 2020, pp. 113–116. DOI: [10.1190/gpr2020-030.1](https://doi.org/10.1190/gpr2020-030.1). URL: <https://library.seg.org/doi/10.1190/gpr2020-030.1>.
- [37] J. A. Dowdeswell et al. “Airbome Radio Echo Sounding of Sub-Polar Glaciers in Spitsbergen”. en. In: (1984).
- [38] R Drews et al. “Layer disturbances and the radio-echo free zone in ice sheets”. en. In: *The Cryosphere* (2009).

- [39] Cooper W. Elsworth, Dustin M. Schroeder, and Matthew R. Siegfried. “Interpreting englacial layer deformation in the presence of complex ice flow history with synthetic radargrams”. en. In: *Annals of Glaciology* 61.81 (Apr. 2020), pp. 206–213. ISSN: 0260-3055, 1727-5644. DOI: 10.1017/aog.2019.41. URL: https://www.cambridge.org/core/product/identifier/S0260305519000417/type/journal_article.
- [40] R. V. Engeset. “Comparison of annual changes in winter ERS-1 SAR images and glacier mass balance of Slakbreen, Svalbard”. en. In: *International Journal of Remote Sensing* 20.2 (Jan. 1999), pp. 259–271. ISSN: 0143-1161, 1366-5901. DOI: 10.1080/014311699213433. URL: <https://www.tandfonline.com/doi/full/10.1080/014311699213433>.
- [41] *Ettus Products*. URL: <https://www.ettus.com/products/>.
- [42] B. Fox-Kemper et al. “Ocean, Cryosphere and Sea Level Change”. In: *Climate Change 2021: The Physical Science Basis. Contribution of Working Group I to the Sixth Assessment Report of the Intergovernmental Panel on Climate Change*. Ed. by V. Masson-Delmotte et al. Cambridge, United Kingdom and New York, NY, USA: Cambridge University Press, 2021, pp. 1211–1362. DOI: 10.1017/9781009157896.011.
- [43] B. Fox-Kemper et al. “Ocean, Cryosphere and Sea Level Change”. en. In: *Climate Change 2021: The Physical Science Basis. Contribution of Working Group I to the Sixth Assessment Report of the Intergovernmental Panel on Climate Change*. Cambridge University Press, Aug. 2021. DOI: 0.1017/9781009157896.011. URL: https://www.ipcc.ch/report/ar6/wg1/downloads/report/IPCC_AR6_WGI_Chapter09.pdf.
- [44] Alice C. Frémand et al. “Antarctic Bedmap data: Findable, Accessible, Interoperable, and Reusable (FAIR) sharing of 60 years of ice bed, surface, and thickness data”. en. In: *Earth System Science Data* 15.7 (July 2023), pp. 2695–2710. ISSN: 1866-3516. DOI: 10.5194/essd-15-2695-2023. URL: <https://essd.copernicus.org/articles/15/2695/2023/>.
- [45] A. S. Gardner et al. “Increased West Antarctic and unchanged East Antarctic ice discharge over the last 7 years”. In: *The Cryosphere* 12.2 (2018), pp. 521–547. DOI: 10.5194/tc-12-521-2018. URL: <https://tc.copernicus.org/articles/12/521/2018/>.
- [46] Alex Gardner, Mark Fahnestock, and Ted Scambos. *MEaSUREs ITS_LIVE Regional Glacier and Ice Sheet Surface Velocities, Version 1 [Dataset]*. 2022. DOI: 10.5067/6II6VW8LLWJ7. URL: <http://nsidc.org/data/NSIDC-0776/versions/1>.
- [47] Tamara Annina Gerber et al. “Upstream flow effects revealed in the EastGRIP ice core using Monte Carlo inversion of a two-dimensional ice-flow model”. en. In: *The Cryosphere* 15.8 (Aug. 2021), pp. 3655–3679. ISSN: 1994-0424. DOI: 10.5194/tc-15-3655-2021. URL: <https://tc.copernicus.org/articles/15/3655/2021/>.
- [48] John Glen. *The flow law of ice: A discussion of the assumptions made in glacier theory, their experimental foundations and consequences*. 1958.

- [49] W Glen. "Experiments on the Deformation of Ice". en. In: *Journal of Glaciology* (1952), p. 4.
- [50] Prasad Gogineni et al. "A CubeSat Train for Radar Sounding and Imaging of Antarctic Ice Sheet". en. In: (2018).
- [51] D. L. Goldsby and D. L. Kohlstedt. "Superplastic deformodemation of ice: Experimental observations". en. In: *Journal of Geophysical Research: Solid Earth* 106.B6 (June 2001), pp. 11017–11030. ISSN: 01480227. DOI: 10.1029/2000JB900336. URL: <http://doi.wiley.com/10.1029/2000JB900336>.
- [52] C. Grima et al. "Surface and basal boundary conditions at the Southern McMurdo and Ross Ice Shelves, Antarctica". In: *J. Glaciology* 65.252 (2019), pp. 675–688. ISSN: 0022-1430. DOI: 10.1017/jog.2019.44.
- [53] P Gudmandsen. "Airborne Radio Echo Sounding of the Greenland Ice Sheet". In: *The Geographical Journal* 135.4 (1969), p. 548. ISSN: 0016-7398. DOI: 10.2307/1795099.
- [54] Preben Gudmandsen. "Layer echoes in polar ice sheets". en. In: *Journal of Glaciology* 15.73 (1975), pp. 95–101. ISSN: 0022-1430, 1727-5652. DOI: 10.3189/S0022143000034304. URL: https://www.cambridge.org/core/product/identifier/S0022143000034304/type/journal_article.
- [55] Mert Gurturk and Metin Soycan. "Accuracy assessment of kinematic PPP versus PPK for GNSS flights data processing". en. In: *Survey Review* 54.382 (Jan. 2022), pp. 48–56. ISSN: 0039-6265, 1752-2706. DOI: 10.1080/00396265.2020.1865016. URL: <https://www.tandfonline.com/doi/full/10.1080/00396265.2020.1865016>.
- [56] Svein-Erik Hamran and Eldar Aarholt. "Glacier study using wavenumber domain synthetic aperture radar". en. In: *Radio Science* 28.4 (July 1993), pp. 559–570. ISSN: 0048-6604, 1944-799X. DOI: 10.1029/92RS03022. URL: <https://agupubs.onlinelibrary.wiley.com/doi/10.1029/92RS03022>.
- [57] Michael Hayes and Peter T. Gough. "Interferometric synthetic aperture processing: a comparison of sonar and radar". en. In: *The Journal of the Acoustical Society of America* 123.5 (May 2008), pp. 3907–3907. ISSN: 0001-4966, 1520-8524. DOI: 10.1121/1.2935898. URL: https://pubs.aip.org/jasa/article/123/5_Supplement/3907/650152/Interferometric-synthetic-aperture-processing-a.
- [58] Mark S. Haynes et al. "Debris: Distributed Element Beamformer Radar for Ice and Subsurface Sounding". en. In: *2021 IEEE International Geoscience and Remote Sensing Symposium IGARSS*. Brussels, Belgium: IEEE, July 2021, pp. 651–654. ISBN: 978-1-66540-369-6. DOI: 10.1109/IGARSS47720.2021.9554746. URL: <https://ieeexplore.ieee.org/document/9554746/>.

- [59] Essam Heggy et al. “Orbiting Arid Subsurface and Ice Sheet Sounder (OASIS): Exploring desert aquifers and polar ice sheets and their role in current and paleo-climate evolution”. en. In: (2013).
- [60] G Heinzel, A Rudiger, and R Schilling. “Spectrum and spectral density estimation by the Discrete Fourier transform (DFT), including a comprehensive list of window functions and some new flat-top windows.” en. In: (2002). URL: https://holometer.fnal.gov/GH_FFT.pdf.
- [61] Florence Hélière et al. “Radio Echo Sounding of Pine Island Glacier, West Antarctica: Aperture Synthesis Processing and Analysis of Feasibility From Space”. en. In: (2007).
- [62] Florence Hélière et al. “Radio Echo Sounding of Pine Island Glacier, West Antarctica: Aperture Synthesis Processing and Analysis of Feasibility from Space”. In: *IEEE Transactions on Geoscience and Remote Sensing* 45.8 (2007), pp. 2573–2582. ISSN: 0196-2892. DOI: 10.1109/tgrs.2007.897433.
- [63] N. Holschuh et al. “Linking postglacial landscapes to glacier dynamics using swath radar at Thwaites Glacier, Antarctica”. en. In: *Geology* (Jan. 2020). ISSN: 0091-7613, 1943-2682. DOI: 10.1130/G46772.1. URL: <https://pubs.geoscienceworld.org/gsa/geology/article/579962/Linking-postglacial-landscapes-to-glacier-dynamics>.
- [64] Nicholas Holschuh et al. “Decoding ice sheet behavior using englacial layer slopes”. en. In: *Geophysical Research Letters* 44.11 (June 2017), pp. 5561–5570. ISSN: 0094-8276, 1944-8007. DOI: 10.1002/2017GL073417. URL: <https://agupubs.onlinelibrary.wiley.com/doi/10.1002/2017GL073417>.
- [65] Martin Horwath et al. “Global sea-level budget and ocean-mass budget, with a focus on advanced data products and uncertainty characterisation”. en. In: *Earth System Science Data* 14.2 (Feb. 2022), pp. 411–447. ISSN: 1866-3516. DOI: 10.5194/essd-14-411-2022. URL: <https://essd.copernicus.org/articles/14/411/2022/>.
- [66] Hanxiong Hu. “Development of A Radio-Frequency Front-End for An Ice-Penetrating Radar”. PhD thesis. Pennsylvania State University, 2015. URL: <https://etda.libraries.psu.edu/catalog/25364>.
- [67] Brian R. Hunt et al. “Solutions of Differential Equations”. In: *Differential Equations with Mathematica*. 3rd. Theorem 5.2, Page 52. Wiley, 2009. ISBN: 0-471-77316-6.
- [68] K. Hutter. *Theoretical Glaciology: Material Science of Ice and the Mechanics of Glaciers and Ice Sheets*. Mathematical Approaches to Geophysics. Springer, 1983. ISBN: 978-90-277-1473-2.
- [69] Adrian Jenkins et al. “Interactions between ice and ocean observed with phase-sensitive radar near an Antarctic ice-shelf grounding line”. en. In: *Journal of Glaciology* 52.178 (2006), pp. 325–346. ISSN: 0022-1430, 1727-5652. DOI: 10.3189/172756506781828502.

- [70] Thomas M. Jordan et al. “A polarimetric coherence method to determine ice crystal orientation fabric from radar sounding: Application to the NEEM Ice Core region”. In: *IEEE Transactions on Geoscience and Remote Sensing* 57.11 (2019), pp. 8641–8657. ISSN: 0196-2892. DOI: 10.1109/tgrs.2019.2921980.
- [71] Ian Joughin et al. “Basal conditions for Pine Island and Thwaites Glaciers, West Antarctica, determined using satellite and airborne data”. en. In: *Journal of Glaciology* 55.190 (2009), pp. 245–257. ISSN: 0022-1430, 1727-5652. DOI: 10.3189/002214309788608705. URL: https://www.cambridge.org/core/product/identifier/S002214300020052X/type/journal_article.
- [72] Sarina Kapai et al. “SAR Focusing of Mobile Apres Surveys”. en. In: *IGARSS 2022 - 2022 IEEE International Geoscience and Remote Sensing Symposium*. Kuala Lumpur, Malaysia: IEEE, July 2022, pp. 1688–1691. ISBN: 978-1-66542-792-0. DOI: 10.1109/IGARSS46834.2022.9883784. URL: <https://ieeexplore.ieee.org/document/9883784/>.
- [73] Jonathan Kingslake et al. “Full-depth englacial vertical ice sheet velocities measured using phase-sensitive radar: Measuring englacial ice velocities”. en. In: *Journal of Geophysical Research: Earth Surface* 119.12 (Dec. 2014), pp. 2604–2618. ISSN: 21699003. DOI: 10.1002/2014JF003275. URL: <http://doi.wiley.com/10.1002/2014JF003275>.
- [74] J. Kohler et al. “Acceleration in thinning rate on western Svalbard glaciers”. en. In: *Geophysical Research Letters* 34.18 (Sept. 2007), 2007GL030681. ISSN: 0094-8276, 1944-8007. DOI: 10.1029/2007GL030681. URL: <https://agupubs.onlinelibrary.wiley.com/doi/10.1029/2007GL030681>.
- [75] Ernst-Jan N. Kuiper et al. “Using a composite flow law to model deformation in the NEEM deep ice core, Greenland – Part 1: The role of grain size and grain size distribution on deformation of the upper 2207 m”. en. In: *The Cryosphere* 14.7 (July 2020), pp. 2429–2448. ISSN: 1994-0424. DOI: 10.5194/tc-14-2429-2020. URL: <https://tc.copernicus.org/articles/14/2429/2020/>.
- [76] E. Larour et al. “Continental scale, high order, high spatial resolution, ice sheet modeling using the Ice Sheet System Model (ISSM)”. In: *J. Geophys. Research: Earth Surface* 117.F1 (2012), pp. 1–20. ISSN: 2156-2202. DOI: 10.1029/2011jf002140.
- [77] E. Larour et al. “Sensitivity Analysis of Pine Island Glacier ice flow using ISSM and DAKOTA”. en. In: *Journal of Geophysical Research: Earth Surface* 117.F2 (June 2012). ISSN: 01480227. DOI: 10.1029/2011JF002146. URL: <http://doi.wiley.com/10.1029/2011JF002146>.
- [78] Justin J. Legarsky, Sivaprasad P. Gogineni, and Torry L. Akins. “Focused Synthetic Aperture Radar Processing of Ice-Sounder Data Collected Over the Greenland Ice Sheet”. In: *IEEE Transactions on Geoscience and Remote Sensing* 39.10 (2001), p. 2109. ISSN: 0196-2892. DOI: 10.1109/36.957274.

- [79] David A Lilien et al. “ImpDAR: an open-source impulse radar processor”. In: *Annals of Glaciology* (2020), pp. 1–10. ISSN: 0260-3055. DOI: 10.1017/aog.2020.44.
- [80] Peng Liu et al. “Software-Defined Radar Systems for Polar Ice-Sheet Research”. In: *IEEE Journal of Selected Topics in Applied Earth Observations and Remote Sensing* 12.3 (2019), pp. 803–820. ISSN: 1939-1404. DOI: 10.1109/jstars.2019.2895616.
- [81] Peng Liu et al. “Software-Defined Radar Systems for Polar Ice-Sheet Research”. en. In: *IEEE Journal of Selected Topics in Applied Earth Observations and Remote Sensing* 12.3 (Mar. 2019), pp. 803–820. ISSN: 1939-1404, 2151-1535. DOI: 10.1109/JSTARS.2019.2895616. URL: <https://ieeexplore.ieee.org/document/8654719/>.
- [82] Joseph A. MacGregor et al. “Radiostratigraphy and age structure of the Greenland Ice Sheet”. In: *Journal of Geophysical Research: Earth Surface* 120.2 (2015), pp. 212–241. ISSN: 2169-9003, 2169-9011. DOI: 10.1002/2014JF003215. URL: <https://onlinelibrary.wiley.com/doi/10.1002/2014JF003215>.
- [83] Joseph A. MacGregor et al. *Radiostratigraphy and Age Structure of the Greenland Ice Sheet, Version 1 [Dataset]*. 2015. DOI: 10.5067/UGI2BGTC4QJA. URL: <http://nsidc.org/data/rrrag4/versions/1>.
- [84] Joseph A. MacGregor et al. “The scientific legacy of NASA’s Operation IceBridge”. In: *Reviews of Geophysics* 59.2 (2021). ISSN: 8755-1209. DOI: 10.1029/2020rg000712.
- [85] Ali Mahmood. “Design, Integration, and Deployment of UAS borne HF/VHF Depth Sounding Radar and Antenna System”. In: (2017).
- [86] E. Mantelli, M. Haseloff, and C. Schoof. “Ice sheet flow with thermally activated sliding. Part 1: the role of advection”. en. In: *Proceedings of the Royal Society A: Mathematical, Physical and Engineering Sciences* 475.2230 (Oct. 2019), p. 20190410. ISSN: 1364-5021, 1471-2946. DOI: 10.1098/rspa.2019.0410. URL: <https://royalsocietypublishing.org/doi/10.1098/rspa.2019.0410>.
- [87] Kenichi Matsuoka. “Pitfalls in radar diagnosis of ice-sheet bed conditions: Lessons from englacial attenuation models: Radar Diagnosis Of Ice-Sheet Beds”. en. In: *Geophysical Research Letters* 38.5 (Mar. 2011). ISSN: 00948276. DOI: 10.1029/2010GL046205. URL: <http://doi.wiley.com/10.1029/2010GL046205>.
- [88] B. Medley et al. “Antarctic firn compaction rates from repeat-track airborne radar data: I. Methods”. en. In: *Annals of Glaciology* 56.70 (2015), pp. 155–166. ISSN: 0260-3055, 1727-5644. DOI: 10.3189/2015AoG70A203. URL: https://www.cambridge.org/core/product/identifier/S026030550025043X/type/journal_article.

- [89] Bailey Miller et al. “Multipass SAR Processing for Radar Depth Sounder Clutter Suppression, Tomographic Processing, and Displacement Measurements”. en. In: *IGARSS 2020 - 2020 IEEE International Geoscience and Remote Sensing Symposium*. Waikoloa, HI, USA: IEEE, Sept. 2020, pp. 822–825. ISBN: 978-1-72816-374-1. DOI: 10.1109/IGARSS39084.2020.9324498. URL: <https://ieeexplore.ieee.org/document/9324498/>.
- [90] Joanna D. Millstein, Brent M. Minchew, and Samuel S. Pegler. “Ice viscosity is more sensitive to stress than commonly assumed”. en. In: *Communications Earth & Environment* 3.1 (Mar. 2022), p. 57. ISSN: 2662-4435. DOI: 10.1038/s43247-022-00385-x. URL: <https://www.nature.com/articles/s43247-022-00385-x>.
- [91] L. Mingo and G.E. Flowers. “An integrated lightweight ice-penetrating radar system”. In: *J. Glaciology* 56.198 (2010), pp. 709–714. ISSN: 0022-1430. DOI: 10.3189/002214310793146179.
- [92] Laurent Mingo and Gwenn E. Flowers. “An integrated lightweight ice-penetrating radar system”. en. In: *Journal of Glaciology* 56.198 (2010), pp. 709–714. ISSN: 0022-1430, 1727-5652. DOI: 10.3189/002214310793146179. URL: https://www.cambridge.org/core/product/identifier/S0022143000206588/type/journal_article.
- [93] Laurent Mingo et al. “A stationary impulse-radar system for autonomous deployment in cold and temperate environments”. In: *Annals of Glaciology* 61.81 (2020), pp. 99–107. ISSN: 0260-3055. DOI: 10.1017/aog.2020.2.
- [94] M. Morlighem et al. “BedMachine v3: Complete Bed Topography and Ocean Bathymetry Mapping of Greenland From Multibeam Echo Sounding Combined With Mass Conservation”. en. In: *Geophysical Research Letters* 44.21 (Nov. 2017), pp. 11, 051–11, 061. ISSN: 0094-8276, 1944-8007. DOI: 10.1002/2017GL074954. URL: <https://onlinelibrary.wiley.com/doi/abs/10.1002/2017GL074954>.
- [95] M. Morlighem et al. “High-resolution ice-thickness mapping in South Greenland”. en. In: *Annals of Glaciology* 55.67 (2014), pp. 64–70. ISSN: 0260-3055, 1727-5644. DOI: 10.3189/2014AoG67A088. URL: <https://doi.org/10.3189/2014AoG67A088>.
- [96] Mathieu Morlighem. *IceBridge BedMachine Greenland, Version 5 [Dataset]*. 2022. DOI: 10.5067/GMEVBWFLWA7X. URL: <https://nsidc.org/data>IDBMG4/versions/5>.
- [97] Mathieu Morlighem et al. “Deep glacial troughs and stabilizing ridges unveiled beneath the margins of the Antarctic ice sheet”. en. In: *Nature Geoscience* (Dec. 2019). ISSN: 1752-0894, 1752-0908. DOI: 10.1038/s41561-019-0510-8. URL: <http://www.nature.com/articles/s41561-019-0510-8>.
- [98] Keith W. Nicholls et al. “A ground-based radar for measuring vertical strain rates and time-varying basal melt rates in ice sheets and shelves”. In: *Journal of Glaciology* 61.230 (2015), pp. 1079–1087. ISSN: 0022-1430. DOI: 10.3189/2015jog15j073.

- [99] Keith W. Nicholls et al. “A ground-based radar for measuring vertical strain rates and time-varying basal melt rates in ice sheets and shelves”. en. In: *Journal of Glaciology* 61.230 (2015), pp. 1079–1087. ISSN: 0022-1430, 1727-5652. DOI: 10.3189/2015JoG15J073. URL: https://www.cambridge.org/core/product/identifier/S0022143000200269/type/journal_article.
- [100] G.K.A. Oswald and S.P. Gogineni. “Mapping basal melt under the northern Greenland Ice Sheet”. In: *IEEE Trans. Geosci. Remote Sens.* 50.2 (2012), pp. 585–592. ISSN: 0196-2892. DOI: 10.1109/tgrs.2011.2162072.
- [101] John Paden et al. “Ice-sheet bed 3-D tomography”. In: *Journal of Glaciology* 56.195 (2010), pp. 3–11. ISSN: 0022-1430. DOI: 10.3189/002214310791190811.
- [102] Ben G. Panzer. “Development of an electrically small Vivaldi antenna: The CReSIS Aerial Vivaldi (CAV-A)”. PhD thesis. University of Kansas, 2007.
- [103] Frédéric Parrenin and Richard Hindmarsh. “Influence of a non-uniform velocity field on isochrone geometry along a steady flowline of an ice sheet”. en. In: *Journal of Glaciology* 53.183 (2007), pp. 612–622. ISSN: 0022-1430, 1727-5652. DOI: 10.3189/0022143000214494. URL: https://www.cambridge.org/core/product/identifier/S0022143000214494/type/journal_article.
- [104] W.S.B. Paterson. “Why ice-age ice is sometimes “soft””. en. In: *Cold Regions Science and Technology* 20.1 (Nov. 1991), pp. 75–98. ISSN: 0165232X. DOI: 10.1016/0165-232X(91)90058-0. URL: <https://linkinghub.elsevier.com/retrieve/pii/0165232X91900580>.
- [105] Frank Pattyn and Mathieu Morlighem. “The uncertain future of the Antarctic Ice Sheet”. en. In: *Science* 367.6484 (Mar. 2020), pp. 1331–1335. ISSN: 0036-8075, 1095-9203. DOI: 10.1126/science.aaz5487. URL: <https://www.science.org/doi/10.1126/science.aaz5487>.
- [106] M.E. Peters et al. “Along-track focusing of airborne radar sounding data from West Antarctica for improving basal reflection analysis and layer detection”. In: *IEEE Trans. Geosci. Remote Sens.* 45.9 (2007), pp. 2725–2736. ISSN: 0196-2892. DOI: 10.1109/tgrs.2007.897416.
- [107] M.E. Peters, D.D. Blankenship, and D.L. Morse. “Analysis techniques for coherent airborne radar sounding: Application to West Antarctic ice streams”. In: *J. Geophys. Research: Solid Earth* 110.B6 (2005). ISSN: 2156-2202. DOI: 10.1029/2004jb003222.
- [108] Matthew E. Peters, Donald D. Blankenship, and David L. Morse. “Analysis techniques for coherent airborne radar sounding: Application to West Antarctic ice streams”. en. In: *Journal of Geophysical Research: Solid Earth* 110.B6 (June 2005), 2004JB003222. ISSN: 0148-0227. DOI: 10.1029/2004JB003222. URL: <https://agupubs.onlinelibrary.wiley.com/doi/10.1029/2004JB003222>.

- [109] S.T. Peters et al. “In Situ Demonstration of a Passive Radio Sounding Approach Using the Sun for Echo Detection”. In: *IEEE Trans. Geosci. Remote Sens.* 56.12 (2018), pp. 7338–7349. ISSN: 0196-2892. DOI: 10.1109/tgrs.2018.2850662.
- [110] Sean T Peters et al. “Passive Synthetic Aperture Radar Imaging Using Radio-Astronomical Sources”. In: *IEEE Transactions on Geoscience and Remote Sensing* (2021), pp. 1–16. ISSN: 0196-2892. DOI: 10.1109/tgrs.2021.3050429.
- [111] Kevin Player et al. “Characterization and Mitigation of RFI Signals in Radar Depth Sounder Data of Greenland Ice Sheet”. In: *IEEE Transactions on Electromagnetic Compatibility* 55.6 (2013), pp. 1060–1067. ISSN: 0018-9375. DOI: 10.1109/temc.2013.2265046.
- [112] David Pollard and Robert M. DeConto. “Modelling West Antarctic ice sheet growth and collapse through the past five million years”. en. In: *Nature* 458.7236 (Mar. 2009), pp. 329–332. ISSN: 0028-0836, 1476-4687. DOI: 10.1038/nature07809. URL: <https://www.nature.com/articles/nature07809>.
- [113] David M Pozar. *Microwave engineering*. John wiley & sons, 2011.
- [114] Samuel Prager et al. “Snow Depth Retrieval With an Autonomous UAV-Mounted Software-Defined Radar”. In: *IEEE Transactions on Geoscience and Remote Sensing* 60 (2022), pp. 1–16. ISSN: 0196-2892. DOI: 10.1109/tgrs.2021.3117509.
- [115] Hamish D Pritchard. “Bedgap: where next for Antarctic subglacial mapping?” en. In: *Antarctic Science* 26 (2014), p. 16. DOI: 10.1017/S095410201400025X.
- [116] M. J. Raymond and G. H. Gudmundsson. “On the relationship between surface and basal properties on glaciers, ice sheets, and ice streams”. en. In: *Journal of Geophysical Research: Solid Earth* 110.B8 (Aug. 2005), 2005JB003681. ISSN: 0148-0227. DOI: 10.1029/2005JB003681. URL: <https://agupubs.onlinelibrary.wiley.com/doi/10.1029/2005JB003681>.
- [117] Bryan Riel and Brent Minchew. “Variational inference of ice shelf rheology with physics-informed machine learning”. en. In: *Journal of Glaciology* 69.277 (Oct. 2023), pp. 1167–1186. ISSN: 0022-1430, 1727-5652. DOI: 10.1017/jog.2023.8. URL: https://www.cambridge.org/core/product/identifier/S0022143023000084/type/journal_article.
- [118] G. De Q. Robin. “Velocity of radio waves in ice by means of a bore-hole interferometric technique”. en. In: *Journal of Glaciology* 15.73 (1975), pp. 151–159. ISSN: 0022-1430, 1727-5652. DOI: 10.3189/S0022143000034341. URL: https://www.cambridge.org/core/product/identifier/S0022143000034341/type/journal_article.
- [119] F. Rodriguez-Morales et al. “Advanced Multifrequency Radar Instrumentation for Polar Research”. In: *IEEE Transactions on Geoscience and Remote Sensing* 52.5 (2014), pp. 2824–2842. ISSN: 0196-2892. DOI: 10.1109/tgrs.2013.2266415.

- [120] Neil Ross, Hugh Corr, and Martin Siegert. “Large-scale englacial folding and deep-ice stratigraphy within the West Antarctic Ice Sheet”. en. In: *The Cryosphere* 14.6 (June 2020), pp. 2103–2114. ISSN: 1994-0424. DOI: 10.5194/tc-14-2103-2020. URL: <https://tc.copernicus.org/articles/14/2103/2020/>.
- [121] Bastien Ruols et al. *4D imaging of a near terminus glacier collapse feature through high-density GPR acquisitions*. en. Oct. 2024. DOI: 10.5194/egusphere-2024-3074. URL: <https://egusphere.copernicus.org/preprints/2024/egusphere-2024-3074/>.
- [122] Kirk M. Scanlan et al. “Interferometric discrimination of cross-track bed clutter in ice-penetrating radar sounding data”. en. In: *Annals of Glaciology* 61.81 (Apr. 2020), pp. 68–73. ISSN: 0260-3055, 1727-5644. DOI: 10.1017/aog.2020.20. URL: https://www.cambridge.org/core/product/identifier/S0260305520000208/type/journal_article.
- [123] Joerg M. Schaefer et al. “Greenland was nearly ice-free for extended periods during the Pleistocene”. en. In: *Nature* 540.7632 (Dec. 2016), pp. 252–255. ISSN: 0028-0836, 1476-4687. DOI: 10.1038/nature20146. URL: <https://www.nature.com/articles/nature20146>.
- [124] D. M. Schroeder, D. D. Blankenship, and D. A. Young. “Evidence for a water system transition beneath Thwaites Glacier, West Antarctica”. en. In: *Proceedings of the National Academy of Sciences* 110.30 (July 2013), pp. 12225–12228. ISSN: 0027-8424, 1091-6490. DOI: 10.1073/pnas.1302828110. URL: <http://www.pnas.org/cgi/doi/10.1073/pnas.1302828110>.
- [125] D.M. Schroeder et al. “Estimating subglacial water geometry using radar bed echo specularity: Application to Thwaites Glacier, West Antarctica”. In: 12.3 (2015), pp. 443–447. ISSN: 1545-598X. DOI: 10.1109/lgrs.2014.2337878.
- [126] D.M. Schroeder et al. “Five decades of radioglaciology”. In: *Annals of Glaciology* 61.81 (2020), pp. 1–13. ISSN: 0260-3055. DOI: 10.1017/aog.2020.11.
- [127] Dustin M. Schroeder et al. “Adaptively constraining radar attenuation and temperature across the Thwaites Glacier catchment using bed echoes”. en. In: *Journal of Glaciology* 62.236 (Dec. 2016), pp. 1075–1082. ISSN: 0022-1430, 1727-5652. DOI: 10.1017/jog.2016.100. URL: https://www.cambridge.org/core/product/identifier/S0022143016001003/type/journal_article.
- [128] Dustin M. Schroeder et al. “Glaciological Constraints on Link Budgets for Orbital Radar Sounding of Earth’s Ice Sheets”. en. In: *2021 IEEE International Geoscience and Remote Sensing Symposium IGARSS*. Brussels, Belgium: IEEE, July 2021, pp. 647–650. ISBN: 978-1-66540-369-6. DOI: 10.1109/IGARSS47720.2021.9553237. URL: <https://ieeexplore.ieee.org/document/9553237/>.

- [129] H. Seroussi et al. “Dependence of century-scale projections of the Greenland ice sheet on its thermal regime”. en. In: *Journal of Glaciology* 59.218 (2013), pp. 1024–1034. ISSN: 0022-1430, 1727-5652. DOI: 10.3189/2013JoG13J054. URL: https://www.cambridge.org/core/product/identifier/S0022143000203742/type/journal_article.
- [130] Hélène Seroussi et al. “ISMIP6 Antarctica: a multi-model ensemble of the Antarctic ice sheet evolution over the 21st century”. In: *The Cryosphere* 14.9 (2020), pp. 3033–3070. DOI: 10.5194/tc-14-3033-2020.
- [131] Helene Seroussi et al. *ISMIP6 Antarctica: a multi-model ensemble of the Antarctic ice sheet evolution over the 21st century*. en. preprint. Ice sheets/Antarctic, Jan. 2020. DOI: 10.5194/tc-2019-324. URL: <https://tc.copernicus.org/preprints/tc-2019-324/>.
- [132] Lei Shi et al. “Multichannel Coherent Radar Depth Sounder for NASA Operation Ice Bridge”. en. In: *2010 IEEE International Geoscience and Remote Sensing Symposium*. Honolulu, HI, USA: IEEE, July 2010, pp. 1729–1732. ISBN: 978-1-4244-9565-8. DOI: 10.1109/IGARSS.2010.5649518. URL: <http://ieeexplore.ieee.org/document/5649518/>.
- [133] Martin Siegert et al. “Twenty-first century sea-level rise could exceed IPCC projections for strong-warming futures”. en. In: *One Earth* 3.6 (Dec. 2020), pp. 691–703. ISSN: 25903322. DOI: 10.1016/j.oneear.2020.11.002. URL: <https://linkinghub.elsevier.com/retrieve/pii/S2590332220305923>.
- [134] Martin J Siegert. “On the origin, nature and uses of Antarctic ice-sheet radio-echo layering”. en. In: *Progress in Physical Geography: Earth and Environment* 23.2 (1999), pp. 159–308. ISSN: 0309-1333.
- [135] A. M. Solgaard et al. “Seasonal Patterns of Greenland Ice Velocity From Sentinel-1 SAR Data Linked to Runoff”. en. In: *Geophysical Research Letters* 49.24 (Dec. 2022), e2022GL100343. ISSN: 0094-8276, 1944-8007. DOI: 10.1029/2022GL100343. URL: <https://agupubs.onlinelibrary.wiley.com/doi/10.1029/2022GL100343>.
- [136] W Stern. “Principles, methods and results of electrodynamic thickness measurement of glacier ice”. In: *Zeitschrift fur Gletscherkunde* 18 (1930), p. 24.
- [137] Paul T. Summers, Dustin M. Schroeder, and Matthew R. Siegfried. “Constraining Ice Sheet Basal Sliding and Horizontal Velocity Profiles Using A Stationary Phase Sensitive Radar Sounder”. In: *2021 IEEE International Geoscience and Remote Sensing Symposium IGARSS*. IGARSS 2021 - 2021 IEEE International Geoscience and Remote Sensing Symposium. Brussels, Belgium: IEEE, July 11, 2021, pp. 5524–5527. ISBN: 978-1-66540-369-6. DOI: 10.1109/IGARSS47720.2021.9554535. URL: <https://ieeexplore.ieee.org/document/9554535/>.
- [138] Thomas Teisberg et al. *thomasteisberg/englacial_velocity: Manuscript Revision 1 [Software]*. Apr. 2025. DOI: 10.5281/zenodo.15191737.

- [139] Thomas O. Teisberg, Anna L. Broome, and Dustin M. Schroeder. “Open Radar Code Architecture (ORCA): A Platform for Software-Defined Coherent Chirped Radar Systems”. In: *IEEE Transactions on Geoscience and Remote Sensing* 62 (2024), pp. 1–11. ISSN: 0196-2892, 1558-0644. DOI: 10.1109/TGRS.2024.3446368. URL: <https://ieeexplore.ieee.org/document/10639440/>.
- [140] Thomas O. Teisberg et al. “Coherence and phase noise in software-defined radio-based ice-penetrating radar instruments”. In: *IGARSS 2024 - 2024 IEEE International Geoscience and Remote Sensing Symposium* (2024). in review.
- [141] Thomas O. Teisberg et al. “Development of a UAV-Borne Pulsed Ice-Penetrating Radar System”. en. In: *IGARSS 2022 - 2022 IEEE International Geoscience and Remote Sensing Symposium*. Kuala Lumpur, Malaysia: IEEE, July 2022, pp. 7405–7408. ISBN: 978-1-66542-792-0. DOI: 10.1109/IGARSS46834.2022.9883583. URL: <https://ieeexplore.ieee.org/document/9883583/>.
- [142] Thomas O. Teisberg et al. “Development of a UAV-Borne Pulsed Ice-Penetrating Radar System”. In: *IGARSS 2022 - 2022 IEEE International Geoscience and Remote Sensing Symposium* 00 (2022), pp. 7405–7408. DOI: 10.1109/igarss46834.2022.9883583.
- [143] Thomas O. Teisberg et al. “Measurement of Englacial Velocity Fields With Interferometric Radio Echo Sounders”. In: *Journal of Geophysical Research: Earth Surface* 130.6 (June 2025), e2025JF008286. ISSN: 2169-9003, 2169-9011. DOI: 10.1029/2025JF008286. URL: <https://agupubs.onlinelibrary.wiley.com/doi/10.1029/2025JF008286>.
- [144] Simone Turchetti et al. “Accidents and opportunities: a history of the radio echo-sounding of Antarctica, 1958–79”. In: *The British Journal for the History of Science* 41.3 (2008), pp. 417–444. ISSN: 0007-0874. DOI: 10.1017/s0007087408000903.
- [145] *UBX - RF Performance Data*. 2021. URL: https://kb.ettus.com/UBX%5C#RF%5C_Performance%5C_Data.
- [146] F. Ulaby and D. Long. *Microwave Radar and Radiometric Remote Sensing*. Artech House, 2015.
- [147] Fawwaz T. Ulaby and David G. Long. *Microwave radar and radiometric remote sensing*. Ann Arbor: The University of Michigan Press, 2014. ISBN: 978-0-472-11935-6.
- [148] *Using the RFNoC Replay Block in UHD 4*. 2022. URL: https://kb.ettus.com/Using%5C_the%5C_RFNoC%5C_Replay%5C_Block%5C_in%5C_UHD%5C_4.
- [149] Irena Vaňková et al. “Vertical Structure of Diurnal Englacial Hydrology Cycle at Helheim Glacier, East Greenland”. en. In: *Geophysical Research Letters* 45.16 (Aug. 2018), pp. 8352–8362. ISSN: 0094-8276, 1944-8007. DOI: 10.1029/2018GL077869. URL: <https://agupubs.onlinelibrary.wiley.com/doi/10.1029/2018GL077869>.

- [150] Yongji Wang, Ching-Yao Lai, and Charlie Cowen-Breen. *Discovering the rheology of Antarctic Ice Shelves via physics-informed deep learning*. en. preprint. In Review, Nov. 2022. doi: 10.21203/rs.3.rs-2135795/v1. URL: <https://www.researchsquare.com/article/rs-2135795/v1>.
- [151] Brian C. Welch and Robert W. Jacobel. “Analysis of deep-penetrating radar surveys of West Antarctica, US-ITASE 2001”. In: *Geophysical Research Letters* 30.8 (2003). issn: 0094-8276. doi: 10.1029/2003gl017210.
- [152] I. M. Whillans. “Radio-echo layers and the recent stability of the West Antarctic ice sheet”. en. In: *Nature* 264.5582 (Nov. 1976), pp. 152–155. issn: 0028-0836, 1476-4687. doi: 10.1038/264152a0. URL: <https://www.nature.com/articles/264152a0>.
- [153] Christian T. Wild, Oliver J. Marsh, and Wolfgang Rack. “Differential interferometric synthetic aperture radar for tide modelling in Antarctic ice-shelf grounding zones”. en. In: *The Cryosphere* 13.12 (Nov. 2019), pp. 3171–3191. issn: 1994-0424. doi: 10.5194/tc-13-3171-2019. URL: <https://tc.copernicus.org/articles/13/3171/2019/>.
- [154] C. Yardim et al. “Greenland Ice Sheet Subsurface Temperature Estimation Using Ultrawide-band Microwave Radiometry”. In: *IEEE Trans. Geosci. Remote Sens.* 60 (2021), pp. 1–12. issn: 0196-2892. doi: 10.1109/tgrs.2020.3043954.
- [155] D. A. Young et al. “The distribution of basal water between Antarctic subglacial lakes from radar sounding”. In: *Philosophical Transactions of the Royal Society A: Mathematical, Physical and Engineering Sciences* 374.2059 (2016), p. 20140297. issn: 1364-503X. doi: 10.1098/rsta.2014.0297.
- [156] Tun Jan Young et al. “Resolving the internal and basal geometry of ice masses using imaging phase-sensitive radar”. en. In: *Journal of Glaciology* 64.246 (Aug. 2018), pp. 649–660. issn: 0022-1430, 1727-5652. doi: 10.1017/jog.2018.54. URL: https://www.cambridge.org/core/product/identifier/S0022143018000540/type/journal_article.
- [157] Hanwen Yu et al. “Phase Unwrapping in InSAR : A Review”. en. In: *IEEE Geoscience and Remote Sensing Magazine* 7.1 (Mar. 2019), pp. 40–58. issn: 2168-6831, 2473-2397, 2373-7468. doi: 10.1109/MGRS.2018.2873644. URL: <https://ieeexplore.ieee.org/document/8672140/>.
- [158] *Zarr-Python Documentation*. URL: <https://zarr.readthedocs.io/en/stable/index.html>.
- [159] Whyjay Zheng et al. “GLAcier Feature Tracking testkit (GLAFT): a statistically and physically based framework for evaluating glacier velocity products derived from optical satellite image feature tracking”. en. In: *The Cryosphere* 17.9 (Sept. 2023), pp. 4063–4078. issn: 1994-0424. doi: 10.5194/tc-17-4063-2023. URL: <https://tc.copernicus.org/articles/17/4063/2023/>.